NSK Technical Journal

Motion & Control

No. 32 June 2021

ISSN1342-3630

NSK

MOTION & CONTROL No. 32
NSK Technical Journal
Printed and Published: June 2021
ISSN1342-3630
Publisher: NSK Ltd., Ohsaki, Shinagawa, Tokyo, JAPAN
Public Relations Department
TEL +81-3-3779-7050
FAX +81-3-3779-7431
Editor: Nobuaki MITAMURA
Managing Editor: Aya OKAMOTO
Design, Typesetting & Printing: Kuge Printing Co., Ltd.

NSK Technical Journal
Motion & Control
No. 32
June 2021

NSK

Contents

Technical Papers

Development of Tapered Roller Bearings for Electric/Hybrid Vehicles ..... *H. Yamanaka, M. Zenbutsu* 1

Demonstration of Two-Speed Seamless Shifting for EV Using Magnetostrictive Torque Sensor ..... *S. Kaneko, S. Yamada, A. Yamamoto* 7

Developments in Steering Performance for Automotive Steering Systems ..... *M. Nishio* 16

Development of Bearings for Industrial Machinery Motors ..... *K. Denpou* 26

High Load Endurance Test Unit for Electric Injection Molding Machine Ball Screws ..... *A. Ishikawa, K. Namimatsu, N. Sekiya* 36

Mobile Extendable Robot Arm (MERA) ..... *S. Teshigawara, H. Harry Asada* 43

Development of an Automated Single-Cell Seeding Device for Biopharmaceuticals ..... *R. House* 56

Quantitative Evaluation of Effects on Dent-Initiated Flaking of Rolling Bearings (Part 1: Evaluation of Dent-Density ρ_d) ..... *F. Aikawa, S. Hashimoto, H. Komata, K. Ueda* 61

Quantitative Evaluation of Effects on Dent-Initiated Flaking on Rolling Bearings (Part 2: Evaluation of Factors Influencing Dent-Density ρ_d) ..... *J. Hamasaki, F. Aikawa, S. Hashimoto, K. Ueda* 66

New Products

Hub Unit Bearing Sealed by a Plastic Sensor Cap 70

Ball Screw Units for Electric Hydraulic Brake Systems 72

High Safety Redundant Column EPS 74

Thin-Section Ball Bearings for Strain Wave Gearings 76

Sealed-Clean Four-Row Tapered Roller Bearing with Long-Life, Water-Resistant Grease 78

High Durability Precision Ball Screw 80

Development of Tapered Roller Bearings for Electric/Hybrid Vehicles

Hiroaki Yamanaka, Makoto Zenbutsu
Automotive Technology Development Center, Automotive Powertrain Bearing Technology Center, Powertrain Bearing Technology Department

Abstract

With stricter regulations and increasing concerns for the environment, consumers, and businesses around the world are requiring better fuel economy in motor vehicles. This has led to the rapid development of electric/hybrid vehicles. Gearboxes for these vehicles require low-viscosity lubricant oil that reduces unit loss to save fuel/electricity. As a result, the lubrication environment for tapered roller bearings (TRBs) used in gearboxes has become increasingly severe, and there is increased focus on maintaining an oil film to prevent surface damage and seizure.

In this article, we will introduce TRBs with improved lubrication in the contact areas between the roller end surface and the inner ring rib resulting in greatly improved seizure resistance. A specially shaped plastic cage supplies oil to the roller end surface, improving seizure resistance by about seven times under low lubrication conditions. Furthermore, we achieved zero churning loss by significantly reducing the amount of lubricating oil and made the TRBs 10% smaller and 5% lighter.

1. Introduction

In recent years, with the strengthening of environmental regulations globally, the fuel economy improvement of automobiles is required, and the development of electric vehicles equipped with drive motors is rapidly advancing.

For electric vehicle gearboxes, efforts are being made to reduce both the amount and the viscosity of lubricating oil to reduce losses in order to achieve fuel and power economy improvements in electric vehicles. As a result, the lubrication environment of tapered roller bearings used in gearboxes has become more severe, and the prevention of surface damage and seizure of bearings due to lubricant film failure has become an important issue in gearbox reliability.

As automobile manufacturers accelerate the development of electric vehicles, a highly robust bearing is required to improve the efficiency of the gearbox. NSK has developed NSK LCube II™ technology to prevent surface damage caused by lubricant film breakage[1].

This article presents a tapered roller bearing in which lubrication at the sliding contact between the roller end surface and the inner ring rib is improved through the use of a specially shaped plastic cage, resulting in improved seizure resistance and reliability in a lean lubrication environment.

2. Factors of Friction of Tapered Roller Bearings and Changes in the Environment in which Bearings Are Used

NSK has developed various types of low friction tapered roller bearings to improve gearbox efficiency[2].

Aihara has reported the theory of frictional resistance of tapered roller bearings[3]. It is known that friction factors of tapered roller bearings are classified into (1)–(4) shown in Figures 1 and 2.

(1) Rolling friction between the raceway surfaces of inner and outer rings and rolling surfaces
(2) Sliding friction between the inner ring rib and roller end surface
(3) Sliding friction between the rollers and cage
(4) Churning resistance of the lubricating oil

Here, (1), (2), and (4) account for the majority of friction in tapered roller bearings.

NSK has developed various types of low friction tapered roller bearings to reduce these friction factors and expand the market.

In recent years, to reduce (4) the churning resistance of lubricating oil in particular, the prevention of seizure of bearings due to running out of oil film (Figure 3) has become an important issue in ensuring high reliability.

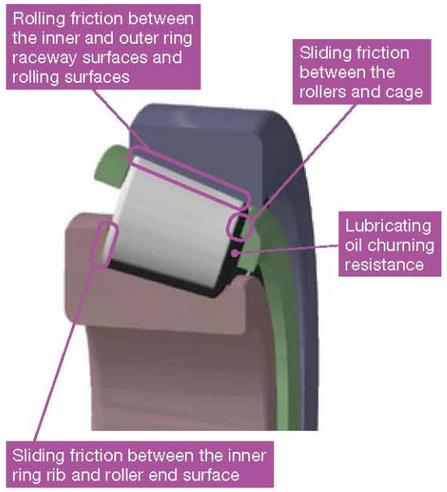

Fig. 1 Friction factors of tapered roller bearing

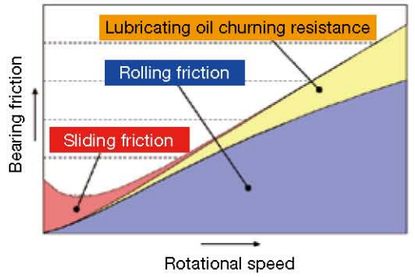

Fig. 2 Relationship between rolling friction and sliding friction

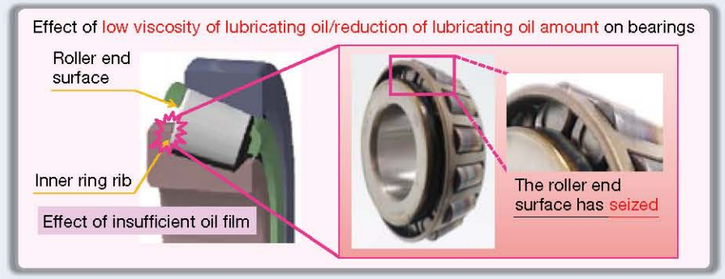

Fig. 3 TRB surface enlarged photograph

3. Features and Effects of the Developed Products

The developed tapered roller bearing (hereinafter referred to as "the developed product") introduced in this article drastically improves seizure resistance under lean lubrication environments by stably maintaining an oil film at the roller end surface and the inner ring rib in a single bearing. The features and effects are described below.

3.1 Features

As shown in Figure 4, this product retains lubricating oil via capillary action through fine grooves located in the cage pocket at the roller end surface contact zone. The width, depth, and shape (among other parameters) of these fine grooves are optimized in order to maximize the oil retention and oil supply effects. When the lubrication is sufficient, oil is retained within the bearing interior, and when lubrication is insufficient, the oil is supplied from the micro grooves to the roller end surface. Therefore, as shown below, seizure resistance is greatly improved.

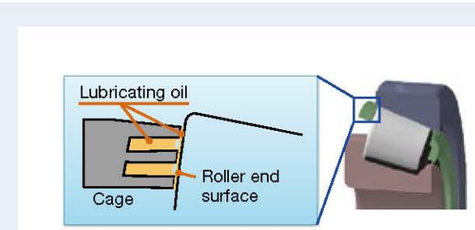

Fig. 4 Schematic of the developed product

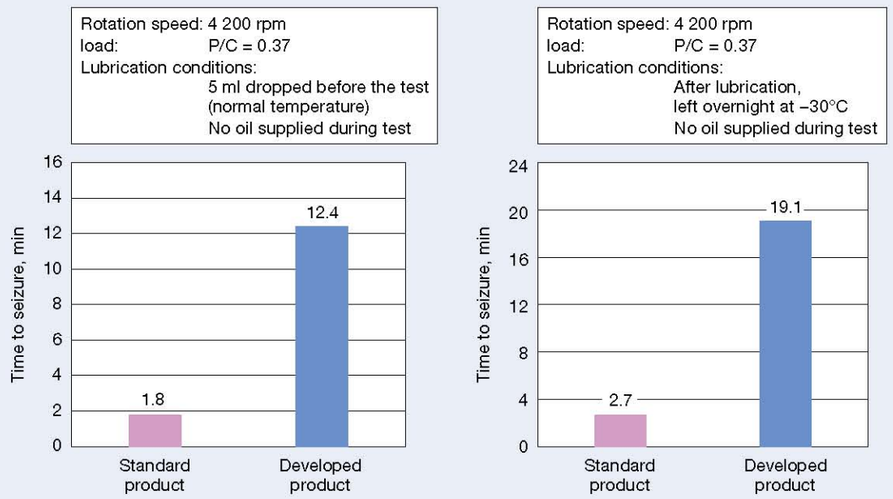

Fig. 5 Bearing seizure test results without lubrication

3.2 Resistance to seizure

Due to the effect of the micro grooves formed in the cage, the developed bearing has dramatically improved seizure resistance compared to the conventional tapered roller bearing.

Figure 5 shows the results of a seizure test. When the oil supply is cut off, seizure occurs within minutes for a standard product due to the lack of lubricating oil between the roller end surface and the inner ring rib. However, the developed product shows seizure resistance of about seven times that of the standard.

Figure 6 shows an example of a test in which the radial dimension of a micro groove (micro groove width) is modified (groove depth is unchanged). The total volume of multiple grooves is roughly identical. With a fewer number of grooves, the seizure resistance is 2.3 times that of the standard product. However, as the number of grooves increases (with decreasing oil groove width), the seizure resistance further improves. This is based on the basic principle that the smaller the groove is, the greater the capillary force. This tendency is more pronounced for lower lubricating oil viscosity and higher bearing rotational speed.

The effect of the micro groove shape, width, and depth were confirmed through testing. Based on the test results, the optimum design guidelines were established resulting in a developed product with excellent seizure resistance.

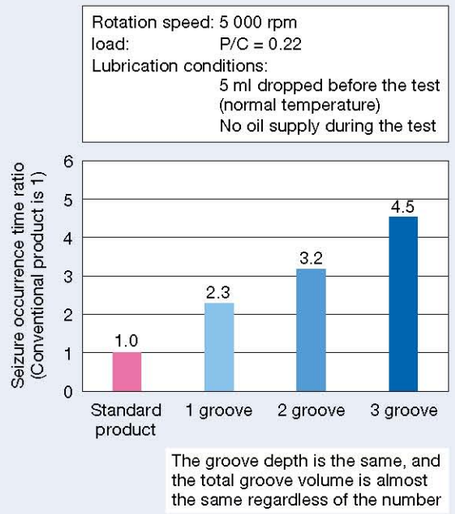

Fig. 6 Bearing seizure test results without lubrication

3.3 Required amount of lubricating oil

Figure 7 shows the results of the comparison test for the amount of lubricating oil required for the gearboxes. The required minimum lubricant amount is obtained by gradually reducing the supplied amount of lubrication until a seizure occurs under the specified operating conditions.

Under operating conditions where the required lubrication amount was determined to be 60 ml/min for the standard product, the developed product showed no seizure even when the lubrication amount was reduced to 2 ml/min.

Conventional tapered roller bearings have required large amounts of lubricating oil supply when used under high loads. However, the developed product can prevent seizure even under lean environments such as oil splash (Figure 8).

As a result, it is possible to eliminate forced lubrication by the oil pump, which has been required in the past. This makes it possible to reduce loss due to the oil pump drive and simplify the lubrication system, including the oil line.

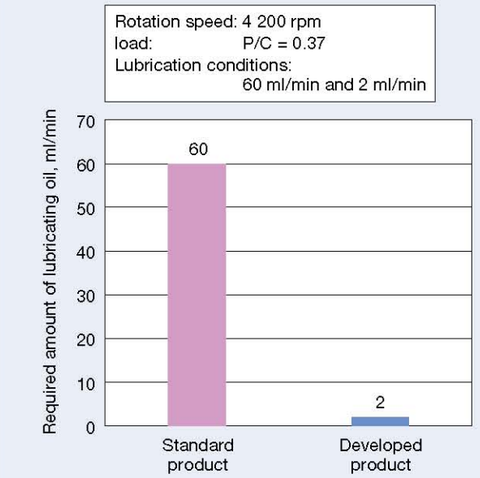

Fig. 7 Comparison of required lubricating oil amount

3.4 Reduction of friction by reducing the amount of lubricating oil

As shown in Figure 8, the newly developed product can greatly reduce the amount of lubricating oil required, making it possible to reduce the churning resistance of the oil to almost zero.

Figure 9 shows a comparison of bearing torque loss between oil bath lubrication and splash lubrication. The oil bath lubrication condition is an oil level at which only the bearing's lower part is immersed in the lubricating oil, and the splash lubrication condition is an oil application only (no immersion during the test).

In the case of oil bath lubrication, the torque loss from churning can be reduced to almost zero by reducing the oil supply amount to the amount present under splash lubrication. This effect is greater under conditions such as high oil level, high lubricating oil viscosity, and high bearing rotational speed.

In this way, eliminating the oil bath lubrication of the bearing and lowering the oil level also reduces the churning resistance of the surrounding components.

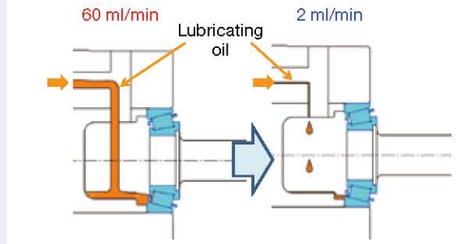

Fig. 8 Schematic diagram of required amount of lubricating oil

3.5 Space-saving

Plastic cages manufactured by injection molding have greater freedom in shape than metal cages manufactured by press molding and can be reduced in size and weight by 10 volume (%) and 5 mass (%) compared to tapered roller bearings using conventional metal cages (Figure 10).

Furthermore, adopting the developed bearing can greatly reduce the size by a factor of three compared to the case in which ball bearings are applied.

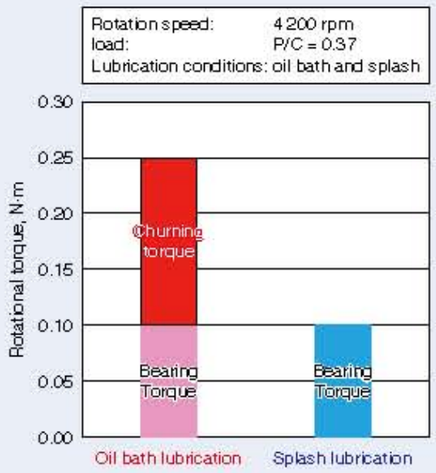

Fig. 9 Torque loss comparison

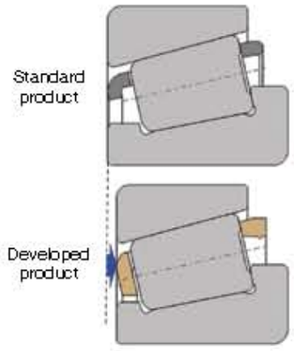

Fig. 10 Size comparison of conventional and developed TRB

4. Summary

NSK has developed low friction tapered roller bearings for the first to the sixth generation and is contributing to improved gearbox efficiency and automobile fuel and power economy with high durability and reliability[1].

In recent years, from the viewpoint of further improvement in fuel economy, there has been an increasing need for lowering the viscosity and reducing the amount of lubricating oil. The newly developed product applies to severe lubrication environments and contributes greatly to fuel economy and reliability improvement, downsizing, and weight reduction of gearboxes for electric vehicles.

At present, in the midst of the revolution in automobile technology, which is said to be once in 100 years, we will continue to promote the development of high-reliability, low-friction bearings that meet the needs of the market and continue to contribute to the improvement of fuel and power economy as well as the reliability of electric vehicles.

References

1) "Low-Friction Technology for Tapered Roller Bearings," *NSK Technical Journal*, 690 (2018) pp. 51–59.
2) S. Aihara, "Friction of Roller Bearings and EHL Viscous Rolling Resistance," *NSK Technical Journal*, 649 (1988) pp. 1–5.
3) M. Chishima, "Development of NSK LCube II TM Tapered Roller Bearings for Electric/Hybrid Vehicles," *NSK Technical Journal*, 692 (2020) pp. 1–7.

Hiroaki Yamanaka

Makoto Zenbutsu

Demonstration of Two-Speed Seamless Shifting for EV Using Magnetostrictive Torque Sensor

Shohei Kaneko, Shota Yamada, and Akihiro Yamamoto
Automotive Technology Development Center, Automotive New Product Development Department

Abstract

Introduction of two-speed transmissions with large step ratio into EVs improves cruising range and driving performance. However, shifting with large step ratio causes severe shock deteriorating driving comfort. NSK proposes that seamless shifting can be realized by making use of the magnetostrictive torque sensor and controlling clutches and e-motor with the torque feedback control signal. This report shows experimental results of seamless shifting with a torque sensor and its advantages.

This article has been approved for reprint by the Society of Automotive Engineers of Japan, Inc., following preprints of the 2020 JSAE Annual Congress (Spring), (No.72-2).

1. Introduction

The demand to reduce carbon dioxide emissions and improve fuel economy has made electric vehicles (EVs) more popular in recent years. The prediction is that strengthening fuel economy regulations in the future will popularize EVs further, but there are problems with cruising range, driving performance, and cost.

Two-speed transmission is among the measures for improving cruising range and driving performance in EVs. In particular, to realize both improvement of cruising range by two-speed shifting with a large step ratio and reduction of shift shock, we propose a shift control method, which feedback controls the clutch and motor using a magnetostrictive torque sensor[1].

This article shows the usefulness of a magnetostrictive torque sensor in a two-speed transmission system with a large step ratio by implementing feedback control with a magnetostrictive torque sensor and demonstrating seamless shifting in a bench test.

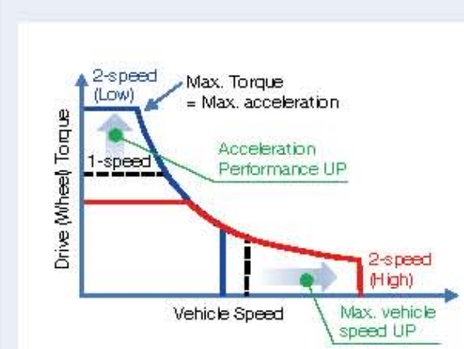

Fig. 1 Driving performance improvement by two-speed transmission

2. Concept of Seamless Shifting

2.1 Necessity of shifting in EVs

At present, many EVs produce their motor output via a speed reducer with a fixed reduction ratio, but they are often inferior to ICE vehicles of the same class in driving force and maximum vehicle speed. Therefore, adding a two-speed shifting function to the speed reducer enables both a large driving force and a maximum vehicle speed increase (Figure 1). Also, expanding the high-efficiency range by gear shifting can improve the cruising range (Figure 2).

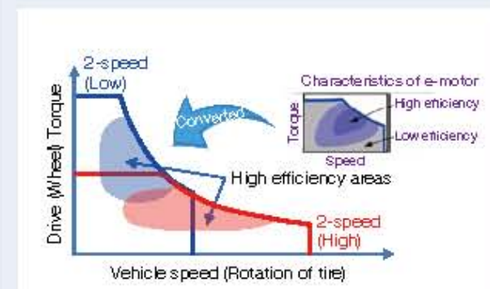

Fig. 2 Cruising range extension by two-speed transmission

2.2 Cruising range improvement and shift shock reduction

Improving cruising range requires an increase in the step ratio between Low and High modes. When the step ratio is small, the high-efficiency area cannot increase effectively due to the motor's overlapping high-efficiency points. Therefore, the cruising range improvement is small. Figure 3 shows the cruising range extension compared to the step ratio in the WLTC mode. It was calculated simply from the running resistance, neglecting the loss during shifting.

Maximizing the cruising range improvement is possible by setting the step ratio to around 2.5. On the other hand, increasing the step ratio causes a shift shock problem. We propose reducing shift shock by the output torque feedback control with a torque sensor[1].

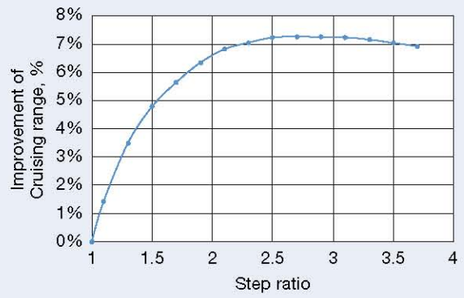

Fig. 3 Optimum step ratio of two-speed transmission for improvement of cruising range

2.3 Definition of seamless shifting

Seamless shifting is gear shifting in which there is no change in the output shaft torque during shifting. This section describes the ideal control for realizing seamless shifting.

Figure 4 shows the torque flow in the Low mode and the High mode in a system composed of a set of planetary gears, a wet multi-plate clutch, and a one-way clutch. In the Low mode, the one-way clutch functions as a brake, and in the High mode, the wet multi-plate clutch is engaged.

The ideal seamless up-shifting in this system is schematically shown in Figure 5[2]. The change in the input/output rotational speed, torque, and clutch torque capacity is expressed on the time axis. In the up-shifting, the modes are shifted in the order of the Low mode, torque phase, inertia phase, and High mode. It is assumed that the inertia of the vehicle is large and the output rotational speed is almost unchanged. In the inertia phase, the motor torque is reduced to expedite the mode shift.

Equation (1) shows the output torque in the torque phase.

$$T_{out} = T_{cl} + i\left(T_{mot} - T_{cl}\right) \quad \cdots\cdots (1)$$

T_{out}: Output torque
T_{cl}: Clutch torque capacity
i: Reduction ratio
T_{mot}: Motor torque

In the torque phase, the clutch torque capacity and the motor torque determine the output torque. With an increase in the clutch torque capacity, the torque flow shifts from the Low mode to the High mode. Although the reduction ratio decreases as the torque flow shifts to the High mode, the motor torque increases to prevent the output torque from decreasing.

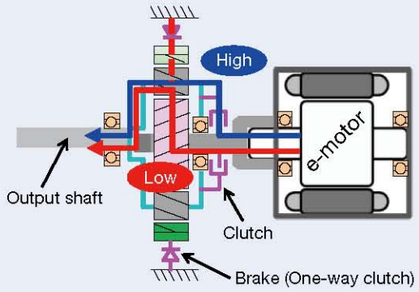

Fig. 4 Torque flow diagram of two-speed transmission in Low and High modes

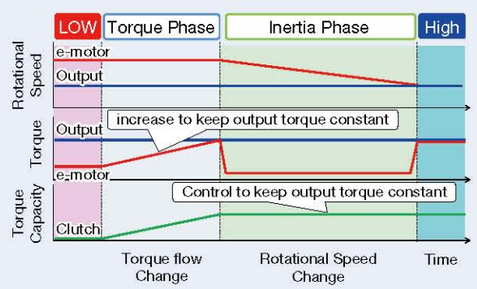

Fig. 5 Ideal control for seamless shifting

Equation (2) shows the output torque in the inertia phase.

$$T_{out} \cong T_{cl} \quad \cdots\cdots (2)$$

Since the output torque is almost equal to the clutch torque capacity in the inertia phase, with the clutch torque capacity kept constant, the output torque is kept constant.

Therefore, if it is possible to accurately estimate the clutch torque capacity both in the torque phase and the inertia phase, seamless shifting becomes possible.

2.4 Estimation error factors for clutch torque capacity

The clutch torque capacity is shown in Equation (3).

$$T_{cl} \propto \mu F \quad \cdots\cdots (3)$$

μ: Friction coefficient
F: Clutch force

The clutch torque capacity is proportional to the friction coefficient and clutch force. On the other hand, the friction coefficients change with such factors as peripheral speed, temperature, and aging, as shown in Figure 6[3, 4]. Also, there is a possibility that the clutch force may contain errors due to the variation of the return spring. It is therefore difficult to maintain constant output torque by controlling the motor and clutch by estimating the correct clutch torque capacity during gear shifting.

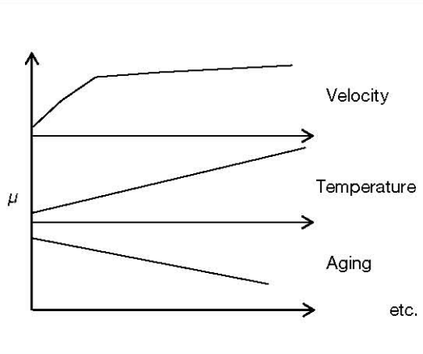

Fig. 6 Fluctuation factors of the friction coefficient

3. Seamless Shifting by Torque Feedback Control

3.1 System configuration

This article demonstrates that torque feedback control allows for seamless shifting without being affected by estimation error of clutch torque capacity.

Figure 7 shows the proposed system configuration. A magnetostrictive torque sensor equipped with the output shaft realizes the feedback control of the clutch force and motor torque while monitoring output torque.

Figure 8 shows the structure of the magnetostrictive torque sensor. The magnetostrictive torque sensor does not require any special materials or processing for the measuring shaft. Moreover, it is thin and contactless with the shaft, which enhances mountability on the transmission. It is mounted on the outer ring of the bearing in our setup.

When the shaft is twisted, the permeability changes due to the inverse magnetostrictive effect. This phenomenon is detected as inductance change of the coil, and the inductance change is converted as torque[5].

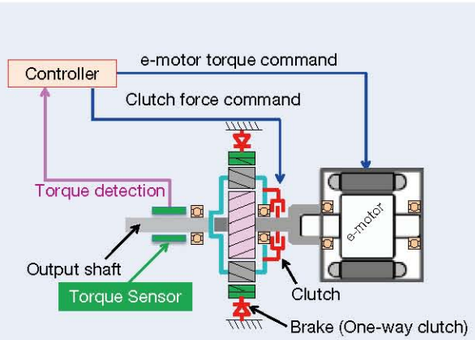

Fig. 7 System configuration of two-speed transmission with a torque sensor for seamless shifting

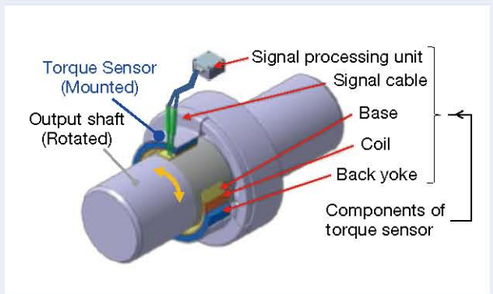

Fig. 8 Magnetostrictive torque sensor

3.2. Torque feedback control

3.2.1 Torque phase

Figure 9 (a) shows the shifting in the torque phase without torque feedback control. In this case, the motor torque is controlled according to the estimated clutch torque capacity to achieve seamless shifting. However, as described above, estimating the clutch torque capacity accurately is difficult. For example, as shown in Figure 9 (a), with the increase in clutch torque capacity due to the friction coefficient's estimation error, the output torque decreases.

On the other hand, Figure 9 (b) shows the shifting with torque feedback control. In this case, even if the output torque decreases due to the friction coefficient's estimation error, the motor torque increases by feedback control so that the output torque can be kept constant.

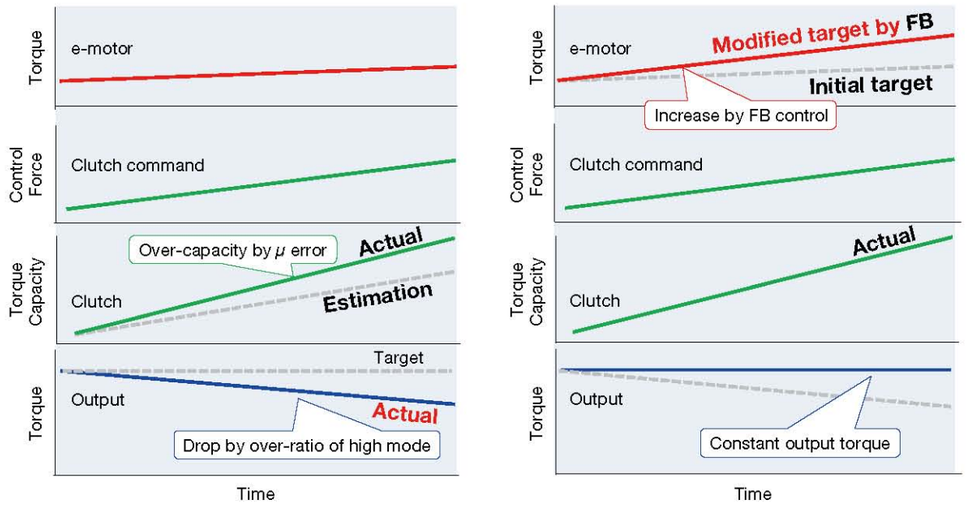

Fig. 9 Benefit of feedback control at the torque phase

3.2.2 Inertia phase

Figure 10 (a) shows the shifting without torque feedback control in the inertia phase. In the inertia phase, the clutch torque capacity is almost equal to the output torque. Therefore, the output torque can be kept constant by keeping the clutch torque capacity constant. However, it is difficult to accurately estimate the clutch torque capacity as in the torque phase. If there is an estimation error in the friction coefficient, the output torque cannot be kept constant as shown in the figure.

Figure 10 (b) shows the shifting with torque feedback control. Even if the output torque decreases due to the estimation error of the friction coefficient, the output torque can be kept constant by increasing the clutch force with the feedback control while monitoring the output torque.

Therefore, feedback control of the motor torque in the torque phase and the clutch force in the inertia phase enable seamless shifting with robustness against the estimation error of the clutch torque capacity. The feedback using the torque sensor is effective to compensate for the friction coefficient fluctuation during shifting. In other words, our torque sensor makes seamless shifting possible by the feedback control of the motor and the clutch.

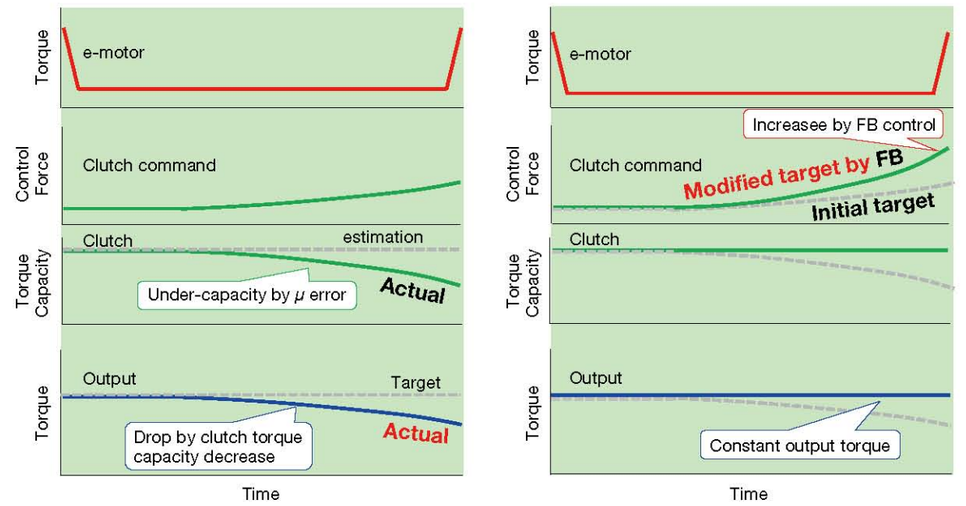

Fig. 10 Benefit of feedback control at the inertia phase

4. Demonstration of Seamless Shifting with Use of a Magnetostrictive Torque Sensor

4.1 Test equipment

This section demonstrates seamless shifting by feedback control using a magnetostrictive torque sensor on the test equipment.

The system shown in Figure 7 is mounted on the test bench, as shown in Figure 11. By speed control of the dynamo, it is simulated that the vehicle has almost no speed change during gear shifting due to large vehicle inertia.

Figure 12 shows the configuration of the two-speed transmission test equipment, having a Low mode and High mode, with the step ratio set to 2.815. The clutch uses a wet multi-plate clutch controlled by hydraulic pressure. The brake uses a one-way clutch. Table 1 shows the specifications of the planetary gear. The output shaft is equipped with the magnetostrictive torque sensor. The setup also has two torque meters for input torque measurement and the verification of the developed torque sensor.

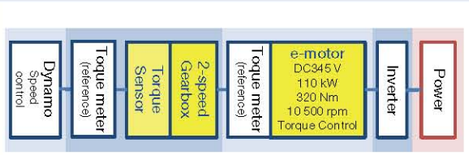

Fig. 11 System configuration for experimental verification of seamless shifting

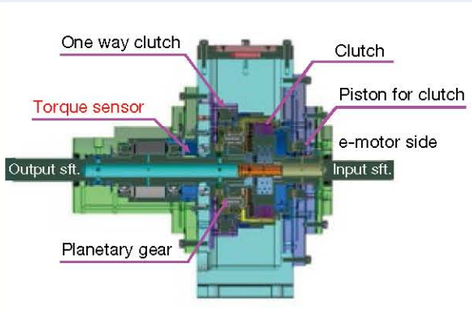

Fig. 12 Two-speed transmission

Table 1 Gear specification

	Sun Gear	Ring Gear	Pinion Gear
Number of teeth	54	98	22
module	1.25		

4.2 Implementation of seamless shifting control

A conducted up-shifting test varies the clutch control pressure in a specific pattern. The test demonstrates that the output torque can be kept constant by feedback controlling the drive motor torque in the torque phase and the clutch force (i.e., the clutch control pressure) in the inertia phase, according to the shifting pattern.

Figure 13 (a) shows the block diagram in the torque phase.

T^*_{out}, T^*_{mot}, F^*_{cl}, F_{cl}, and μ_n indicate the target output torque, the motor torque command value, the clutch control pressure command value, the measured clutch control pressure value, and a nominal value of the friction coefficient, respectively. The mode shifts by applying the pattern of time change in F^*_{cl}. The output torque is controlled by a feedforward controller and feedback controller. The feedforward controller commands the motor torque in accordance with the calculated value of the clutch torque capacity from μ_n and F_{cl}. The feedback controller commands the motor torque using the torque sensor information to perform robust seamless shifting.

Figure 13 (b) shows the block diagram in the inertia phase. The mode transition is expedited by lowering T^*_{mot} under the target torque in the high mode. V shows the measured values of the relative rotational speed of the input rotational speed (sun gear rotational speed) and the output rotational speed (carrier rotational speed). The output torque obtained by the torque sensor is feedback-controlled to compensate for the error of the feedforward controller of the clutch, considering the μ-V characteristic of the friction plates.

The change in the reduction ratio determines the transition from the torque phase to the inertia phase. When determining the phase transition, the control shown in Figure 13 (a) and the control shown in Figure 13 (b) are switched.

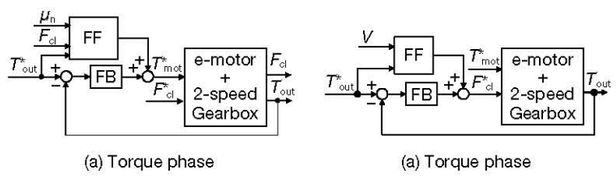

Fig. 13 Feedback control system for seamless shifting

4.3 Results of the shifting test

Figure 14 shows the results of the gear shifting test. The horizontal axis shows the time axis in Figures 14 (a)–(d). The vertical axis shows the rotational speed, torque, clutch control pressure, and the change rate of friction coefficient in percentage. The change rate of friction coefficient is calculated by obtaining T_{cl} from Equations (1) and (2) and the measured input/output torque. The friction coefficient at the end of the torque phase is defined as 100%. The friction coefficient is calculated from the time when the clutch engagement is stabilized in the torque phase using the moving average value at 10 points in the sampling period of 1 millisecond.

The mode shifts in the following order: Low mode (before A), torque phase (between A and B), inertia phase (between B and C), and High mode (after C).

In Low mode, the brake (one-way clutch) is functioning. Therefore, the reduction ratio is 2.815. The hydraulic chamber of the clutch is filled with hydraulic fluid to prepare for shifting.

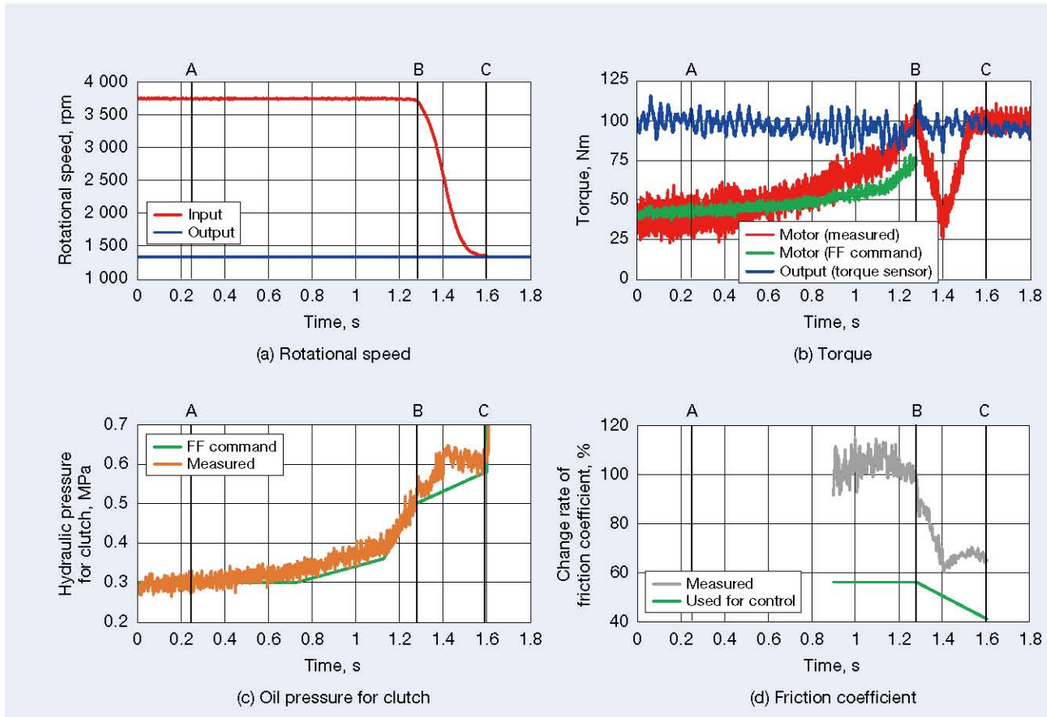

Fig.14 Experimental results of seamless upshifting

As the clutch control pressure increases in the torque phase, the clutch torque capacity also increases. As a result, the torque flow shifts to a High mode, and the output torque tends to decrease. The output torque feedback control increases the motor torque to keep the output torque constant.

In the inertia phase, the clutch control pressure is controlled to keep the output torque constant until the input rotational speed (sun gear rotational speed) decreases and matches the output rotational speed (carrier rotational speed).

After the gear shifting is completed, the clutch is fully engaged and the transition to the High mode is completed. In High mode, the input shaft and the output shaft are directly connected. The motor torque is controlled to keep the output torque constant across the gear shifting, considering the step ratio.

Figure 14 (b) shows a comparison between the motor torque command value by the feedforward control indicated by the green line and the measured value with the feedback control by the output torque information indicated by the red line.

In the torque phase (between A and B), there is a large difference between the measured input torque and the input torque command without FB control. The command indicated by the black line is based on μ_n and F_cl. Therefore, the lack of motor torque mainly caused by the difference between μ_n and the actual friction coefficient is compensated by the output torque FB control.

Figure 14 (c) compares the command value of the clutch control pressure by the feedforward control indicated by the green line and the measured value with the feedback control of the output torque information indicated by the orange line.

In the inertia phase (B-C), the clutch pressure is controlled with the FF controller and the output torque FB control. The FF controller generates the ramp command to roughly compensate the μ-v characteristic. The FB control compensates the modeling error of friction coefficient as shown in the discrepancy between the green and orange lines.

Therefore, the output torque indicated by the blue line in Figure 14 (b) is kept constant between A and C.

In this way, the feedback control using the magnetostrictive torque sensor equipped with the output shaft can control the motor torque in the torque phase and the clutch force in the inertia phase. This approach enabled seamless shifting with no output torque fluctuation during, before, or after gear shifting.

Figure 14 (d) compares the actual friction coefficient and the friction coefficient used for control. Since the friction coefficient changes with time during gear shifting, it is difficult to estimate the friction coefficient accurately. Even if there is a discrepancy between the actual friction coefficient and the friction coefficient used for control, this test result of seamless shifting shows the usefulness of the output torque feedback control.

This article describes the control method for seamless shifting. Feedback control using a torque sensor can arbitrarily control output torque without being affected by disturbances, such as the estimation error of clutch torque capacity.

5. Conclusion

In this article, we aimed to improve the shift quality to solve a problem in EV drive systems with a two-speed transmission having a large step ratio. This contributes to an improvement for cruising range and driving performance without negatively affecting driving comfort.

In order to realize a constant control of output torque with robustness, we proposed a shifting control method that uses a magnetostrictive torque sensor to feedback control the motor torque in the torque phase and clutch thrust in the inertia phase. We demonstrated the usefulness of the magnetostrictive torque sensor in an EV's two-speed transmission system with a large step ratio by achieving seamless shifting in the bench test.

Acknowledgments

The authors thank Professor Aihara at Hosei University for his support of theoretical construction and simulation development on seamless shifting. We are also grateful to Hitachi Metals, Ltd. for the support of the torque sensor developments.

REFERENCES

(1) K. Fukuda, J. Ono, T. Miyazaki, and S. Okada, "Proposal to apply Magnetostrictive Torque sensor in EV: Real time torque measurement of turbine shaft," JSAE Annu. Congress Spring, No. 20195291, pp. 1–6, Yokohama, Japan, May 2019.

(2) JSAE, "AUTOMOTIVE ENGINEERING HANDBOOK," Vol. 1, pp. 113–115, 2015.

(3) Pär Marklund, Rikard Mäki, Roland Larsson, Erik Höglund, M. M. Khonsari, and Joonyoung Jang, "Thermal influence on torque transfer of wet clutches in limited slip differential applications," *Tribology International*, Vol. 40, No. 5, pp. 876–884, 2007.

(4) K. Matsuo and S. Saeki, "Study on the Change of Friction Characteristics with Use in the Wet Clutch of Automatic Transmission," SAE Technical Paper, No. 972928, pp. 93–98, 1997.

(5) T. Nakamura, Y. Sugiyama, and H. Shimizu, "Magnetostrictive Torque Sensor for In-Vehicle Transmission," Hitachi metals technical review, Vol. 35, pp. 18–23, 2019.

Shohei Kaneko

Shota Yamada

Akihiro Yamamoto

Developments in Steering Performance for Automotive Steering Systems

Makoto Nishio
Steering & Actuator Technology Center, Steering R&D Center

Abstract

Steering performance, which allows the vehicle to move as the drivers expect, is an important metric for driver comfort. Steering performance has been tuned by control parameters in steering systems based on the feelings of experienced drivers. However, requirement specifications have not been defined, meaning steering performance has not been designed or evaluated based on quantitative targets. To solve this problem, strategies defining requirement specifications for vehicles and steering systems have been developed to design and evaluate steering performance. For example, 1D simulation has been employed in system design to allow steering performance to be analyzed based on the characteristics of individual units/components. Further developments aimed at better steering performance and autonomous driving will provide ease and pleasure for drivers using NSK steering systems.

1. Foreword

Steering performance refers to the ability of the vehicle to move as intended or expected by the driver. Good steering performance gives the driver a sense of ease and comfort while driving. On the other hand, bad steering performance gives the driver uncomfortable feelings such as a lack of unity with the car and fatigue. Therefore, steering performance is crucial and influences the impression of the whole vehicle.

The driver controls the vehicle by changing the tire's direction through the steering system. Therefore, the steering system's contribution to the steering performance is significant. In the coming era of automated driving, it goes without saying that the performance of the steering system is important for achieving vehicle motion that does not cause discomfort to the passengers.

Steering performance has been tuned by control parameters in steering systems based on the feelings of experienced drivers. However, the relationship between a sense-based evaluation and physical characteristics in most steering performance has not been made clear. As a result, design and evaluation based on quantitative targets have yet to be achieved.

In the development of better steering performance, the V-shaped process of development has been introduced[1]. Requirement specifications are defined by the input and output of the steering system, such as rack displacement and rack reaction force to steering torque and steering angle, based on the user's requirements. The steering system is designed and evaluated based on quantitative target characteristics (Figure 1).

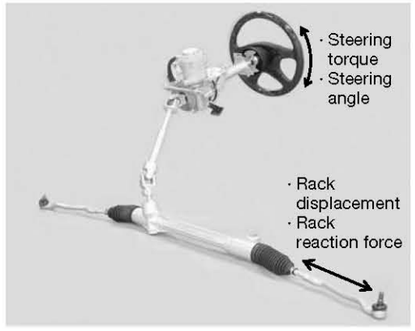

Fig. 1 Steering system input and output

2. Steering Performance Requirement Specifications Definition from the User's Point of View

2.1 Steering performance development process

The development process of steering performance takes the form of a V-shaped process starting from the extraction of driver requirements to reflect end-user needs in the design of steering system products (Figure 2).

In the requirement extraction, requirements for steering performance are extracted and summarized from the end-user's viewpoint.

In the vehicle requirement specifications definition, requirements for steering performance and target performance are quantified from the vehicle's viewpoint and summarized as vehicle requirement specifications.

In the steering system requirement specifications definition, in order to specify system requirement specifications that satisfy the vehicle requirement specifications, the vehicle requirement specifications are assigned to the steering system.

In the steering system design, the system requirement specifications are allocated to each unit in the system to realize a steering system that satisfies the specifications.

Figure 3 shows the development process and deliverables of each process. This article introduces the vehicle requirement specifications definition and steering system design.

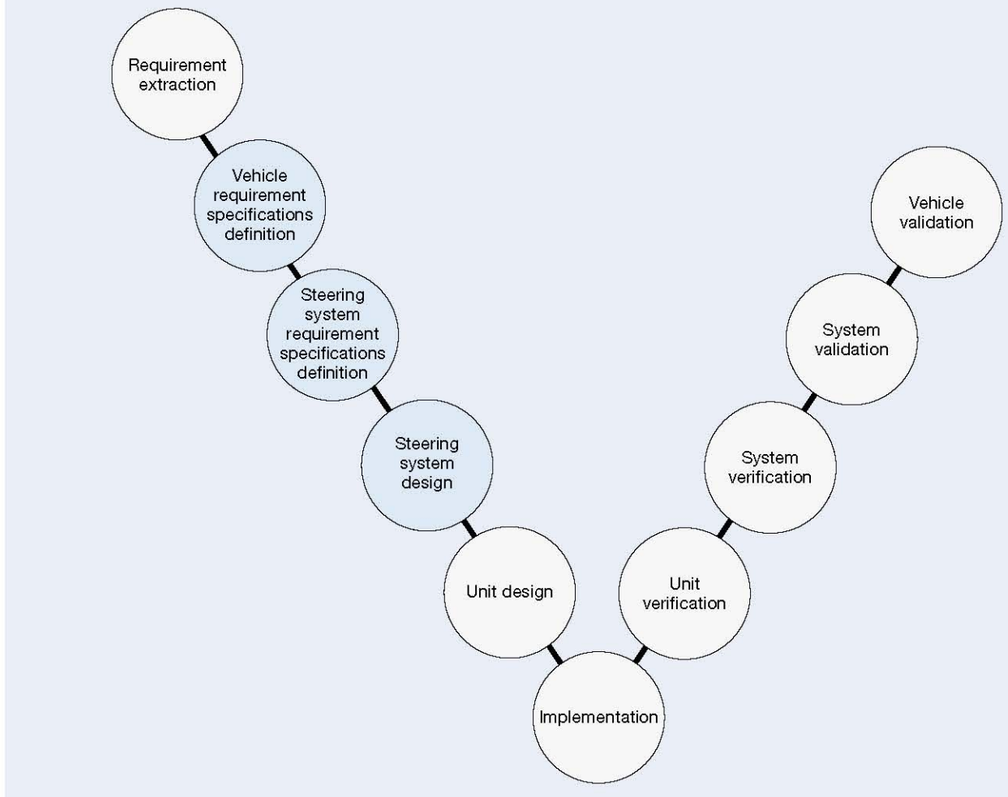

Fig. 2 V-shaped process for development

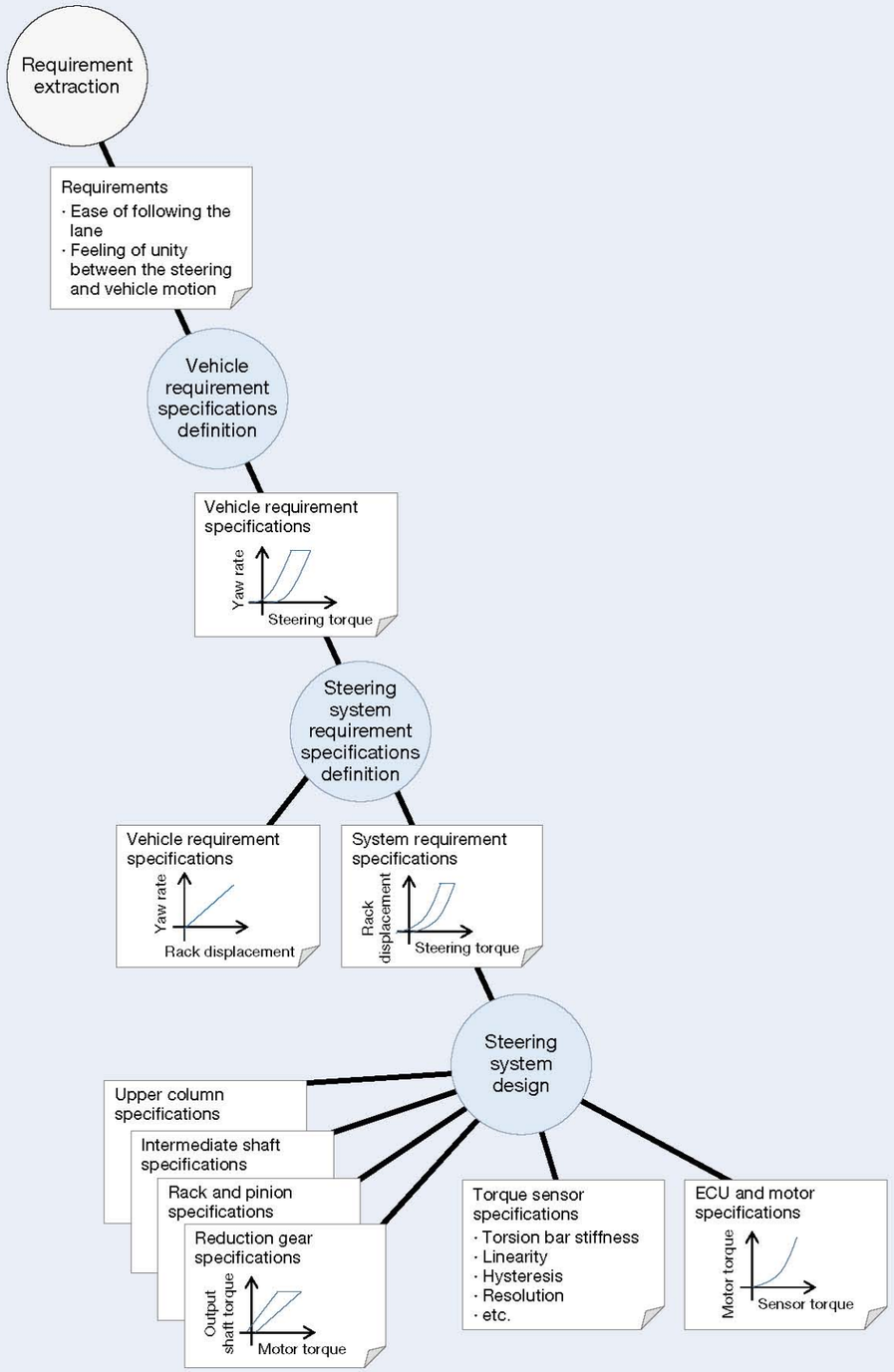

Fig. 3 Development process and outputs for steering performance

2.2 Procedure for defining vehicle requirement specifications

Although the vehicle's target performance cannot be realized only by the steering system, it is indispensable in defining its requirements.

In the vehicle requirement specifications definition, the driver's requirements such as "ease of following the lane" and "feeling of unity between the steering and the vehicle motion," which were obtained by the requirement extraction, are quantified as physical characteristics as the vehicle requirement specifications of steering performance.

The quantification of requirements comprises performing sensory evaluation and quantitative evaluation in each requirement item, comparing the results, and finding the correlation. The sensory evaluation ranks the performance of multiple benchmark vehicles for each requirement. In the quantitative evaluation, the test data measured for each requirement item is analyzed by function approximation[2] etc., and the parameters correlated with the sensory evaluation results are investigated (Figure 4).

2.3 Case 1: Quasi-static characteristics of the "on-center" zone

As the first specific example of the vehicle requirement specifications definition, this article introduces an example of quantifying "quasi-static characteristics of on-center." This is a critical characteristic that influences the steering performance during straight driving in the central zone called on-center, which comprises most driving actions. The following all required on center: ease of control when correcting the course to stay in the lane, straight driving stability to protect against careless steering, and good steering stability. These are crucial characteristics that cause fatigue during driving.

In the sensory evaluation, the vehicles were benchmarked and ranked from the viewpoint of ease of control, straight driving stability, and the characteristics to relieve fatigue during long-distance driving on main roads and expressways.

The quantification included formulating steering characteristics by referring to the technique using equations (1) and (2) proposed in the previous research[2].

$$SA = a_0 \cdot ST + a_s \cdot ST^{b_s} \quad \cdots\cdots\cdots (1)$$

$$YR = a_y \cdot ST^{b_y} \quad \cdots\cdots\cdots (2)$$

The measured steering angle (SA) was fitted with a function of steering torque ST (Eq. (1)) at the time of quasi-static turning from straight driving. The measured yaw rate (YR) was fitted with a function of the steering torque ST (Eq. (2)) (Figure 5). The equations (1) and (2) are modified for the actual fitting to cope with the change of characteristics due to increased friction of the steering system in recent years.

Figure 6 shows the steering angle characteristics to steering torque obtained by applying the fitting based on Equation (1) to the quantitative measurement data of all benchmark vehicles. Figure 6 shows the evaluation results that the more upper left of the figure, the lighter the feelings in the driver's hand and the worse the settling, and the lower right of the figure, the heavier the feelings, meaning a strong relationship with feelings. Figure 7 shows the characteristics of yaw rate to steering torque obtained by applying a fitting based on Equation (2) to all benchmark vehicles' quantitative measurement data. In Figure 7, the evaluation results show that the more upper left of the figure, the worse the straight driving stability and the more unsteady the response, and the lower the right of the figure, the slower the response, meaning a strong relationship with the vehicle response.

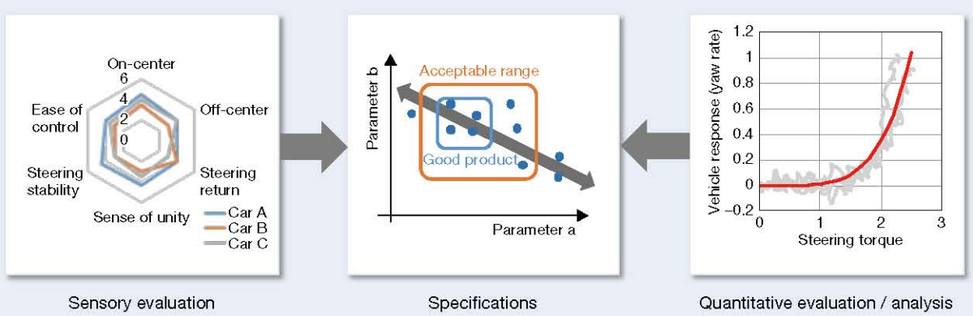

Fig. 4 Concept of requirement specifications for vehicles

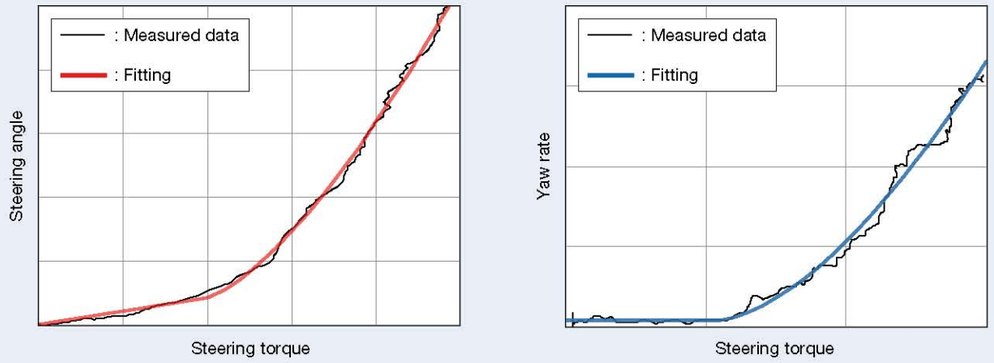

Fig. 5 Fitting for the response from steering torque to the steering angle and yaw rate

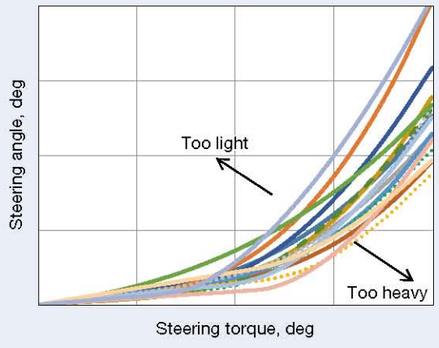

Fig. 6 Response from steering torque to the steering angle of the vehicles for benchmarking

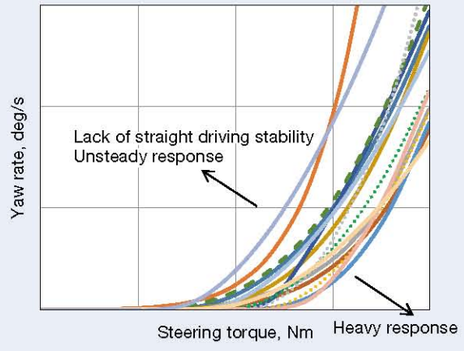

Fig. 7 Response from steering torque to the yaw rate of the vehicles for benchmarking

Figures 8 and 9 show the results of extracting and arranging the approximate equation coefficients from each vehicle's fitting result. Figure 8 shows the coefficients' distribution a_s and b_s of Eq. (1) extracted from the relationship between steering torque and steering angle of all benchmark vehicles and is used as an index of feelings in driver's hand. The area surrounded by the red circle was evaluated as a suitable area for the vehicle in the sensory evaluation. From the relationship with the sensory evaluation comments, the trend was confirmed where the right lower part was firm and the left upper part was light even in moderate response.

Figure 9 shows the distribution of the coefficients a_y and b_y of Equation (2) extracted from the relationship between steering torque and the yaw rate of all benchmark vehicles and is used as an index of vehicle response. The area surrounded by a red circle was evaluated as a high-ranking vehicle in the sensory evaluation and was considered as adequate vehicle response with good agility and less fatiguing. From the relationship with the sensory evaluation comment, the trend was confirmed where the right lower part provides ease and the left upper part was light even in the adequate vehicle response.

This result indicates that the vehicle's on-center steering performance will be improved by adapting the characteristics to both indexes' high evaluation area, successfully creating a car that can be driven without fatigue. In addition, adjusting characteristics in the highly evaluated area makes steering performance suitable for vehicle concepts such as agility and straight driving stability.

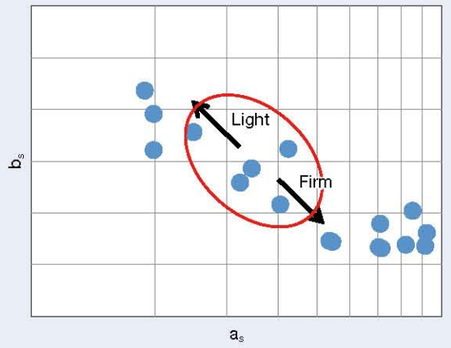

Fig. 8 Index of steering feeling

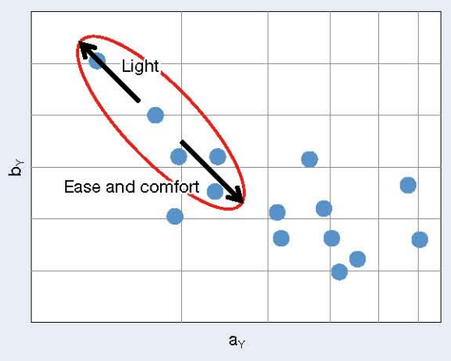

Fig. 9 Index of vehicle response

2.4 Case 2: Clean and smooth feeling of steering

As the second specific example of a vehicle requirement specifications definition, an example of quantifying the "clean and smooth feeling of steering" is introduced.

"The first turn of the steering feels clean." "The first steering from the parking lot feels smooth and nice." These expressions refer to the feeling of quality and luxury of steering and have often been used in development.

However, the relationship between physical properties and sensory evaluation, i.e., clean and smooth, is yet to be realized, and products continue to be made by adaptation relying on the senses of the evaluation drivers.

In this article, the requirement specifications for cleanness and smoothness are defined by evaluating the damping ratio of the system, including all of the spring, inertia, and viscosity shown in equation (3), based on the assumption that the gradient of the steering reaction force to the steering angle, the inertia of the steering system, and viscosity influence the clean and smooth feeling.

$$\zeta = \frac{C}{2\sqrt{IK}} \quad \cdots\cdots\cdots (3)$$

ζ: damping ratio
K: gradient of steering reaction force with respect to steering angle [Nm/rad]
I: inertia of the whole steering system [kg·mm^2]
C: viscosity of the whole steering system [Nm·s/rad]

For this item, benchmark results for vehicles in the market are not used, but a sample with the control parameters that affect the spring term and the viscosity term of the prototype steering system, tuned by the driver's senses, is used. After tuning the sample to the four levels that are clean or smooth feeling that is comfortable, and spongy or sticky feeling that is unpleasant, to make the sensory scores evenly spaced, they were evaluated.

The damping ratio was evaluated by calculating the frequency characteristics of the damping ratio from the relationship between steering torque and steering angle obtained by applying a steering speed sweep input with constant steering angle amplitude (Figure 10).

The frequency characteristics indicate the four levels of damping ratio are placed at equal intervals. The average damping ratio in the frequency band where the driver frequently steers was compared with the sensory evaluation results. This result confirmed a strong correlation, indicating that the average damping ratio can be a valid index (Figure 11). A steering system with a feeling tailored to the customer's preference will be realized by applying the evaluation based on the average damping ratio into future product development.

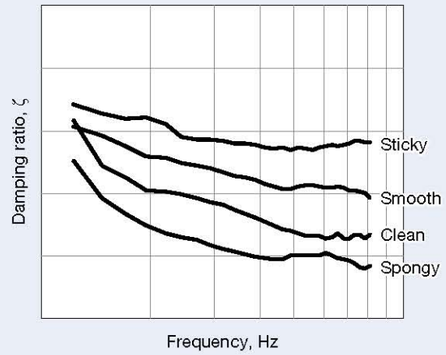

Fig. 10 Frequency characteristics of damping ratio

Fig. 11 Specifications for a viscous feeling

3. Realization of a Steering System that Satisfies the Requirement Specifications

3.1 Steering system requirement specifications definition

The performance as the goal of a vehicle is quantified by the vehicle requirement specifications definition. The next step is to assign the requirement specifications of steering performance from the vehicle to the steering system (Figure 3).

As shown in Section 2, the vehicle requirement specifications are defined by quantifying the relationship between the driver's input to the steering wheel and the vehicle's feedback to the driver, i.e., the yaw rate and lateral acceleration felt by the driver. The steering system requirement specifications based on vehicle requirement specifications can be defined by specifying characteristics of the vehicle, such as the rack reaction force to rack displacement, yaw rate and lateral acceleration to rack displacement (Figure 12).

Therefore, a two-wheel vehicle model that can express the frequency characteristics of rack reaction force and vehicle response was prepared and used to define the steering system requirement specifications.

Combining this model with the steering system simulation (described later) enabled assigning the requirement specifications of steering performance to the steering system.

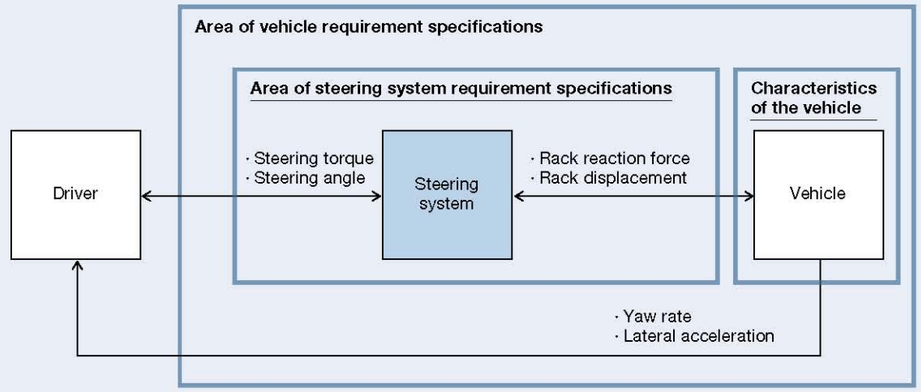

Fig. 12 Scope of requirement specifications for the steering system

3.2 Steering system design

By defining the steering system requirement specifications, the performance to be achieved by the steering system is quantified. Next, the requirement specifications are assigned to each unit constituting the system to realize a system that satisfies the steering system requirement specifications (Figure 3).

Clarifying the connection from the vehicle's requirements and the requirement specifications for a vehicle to the specifications for the unit enables a consistent design.

The specifications were assigned using a simulation of the steering system by the 1D model composed of the simple physical element that expresses each unit's input and output characteristics.

Figure 13 shows the configuration of the units of the column-type ESP from the viewpoint of steering performance. The constructed model limited the physical elements constituting each unit to the minimum necessary elements for analyzing steering performance.

The model of mechanical elements included spring, inertia, friction, and viscosity, and the model of the ECU and motor, which determine the assist force, has the characteristics similar to those of the product.

Applying the load proportional to the rack displacement under the actual vehicle driving condition to the steering system model combined with these unit models and simulating the quasi-static steering input from the steering wheel produced the Lissajous waveform of steering torque and steering angle (Figure 14).

Furthermore, by combining the steering system model and the vehicle model explained in Section 3.1, it is possible to simulate both the response of the on-center quasi-static characteristics and the vehicle response shown in Section 2.3.

An example of changing the stiffness of the torsion bar of the torque sensor is shown as a case of analyzing the on-center quasi-static characteristics by simulation. The change in the slope of the high stiffness area at the beginning of steering by changing the torsion bar's stiffness is confirmed (Figure 15).

In this case, by increasing or decreasing the stiffness by 30% compared with the original, the contribution of the torsion bar stiffness to the on-center quasi-static characteristics is confirmed. Changing each unit's performance in the simulation realizes a design in which each unit's characteristics satisfy the vehicle requirements. It is therefore possible to assign vehicle specifications to each unit in the steering system.

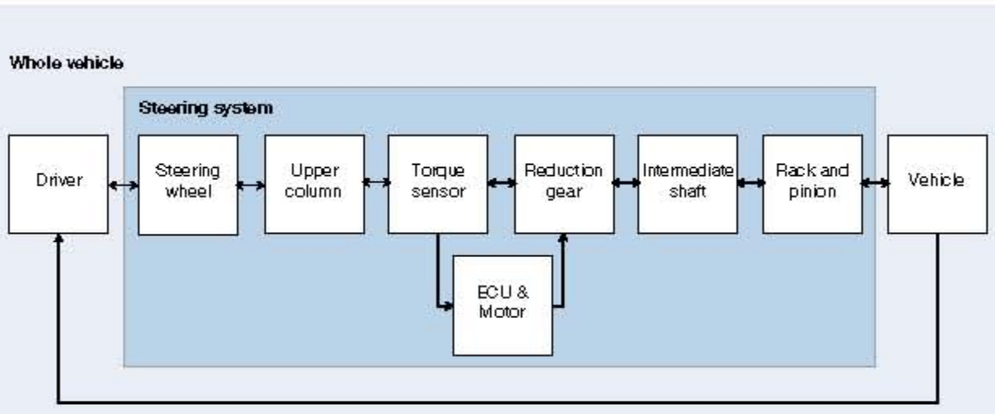

Fig. 13 Structure of the column-type EPS system

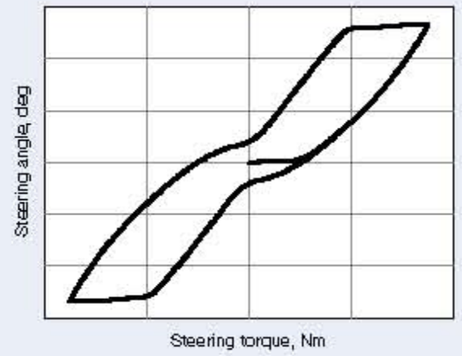

Fig. 14 Results of the system simulation

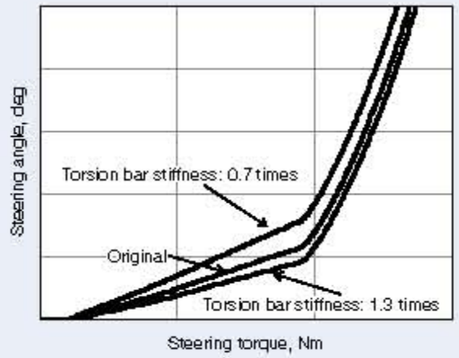

Fig. 15 Example of parameter study for the unit parameter

4. Afterword

This article showed that a consistent system design of steering performance from requirement extraction is possible by defining vehicle requirement specifications and allocating specifications to units using vehicle models and steering system models according to the V-shaped process of development.

Steering performance will remain as requirements as long as drivers are holding steering wheels. Even fully autonomous driving, in which the driver is a passenger, does not change the needs for the technology to define the requirement specifications for the steering system and perform system design.

Further developments aimed at better steering performance and autonomous driving will provide ease and pleasure for drivers using NSK steering systems.

References

1) M. Oba "Improving the Efficiency of Derivative Development through Systematic Restructuring," *NSK Technical Journal*, No. 690 (2018).

2) I. Kushiro "Mathematical Model of Skilled Driver's Steering Pattern Based on Minimum Jerk Model," Transactions of the Society of Automotive Engineers of Japan, Inc. Vol. 47, No. 5 (2016).

Makoto Nishio

Development of Bearings for Industrial Machinery Motors

Katsuaki Denpou
Industrial Machinery Bearing Technology Center, Robot & Motor Bearing Technology Department

Abstract

Motor power consumption is said to make up 40 to 50% of the world's power consumption, making motors a key energy reduction target. High-efficiency motors with improved motor energy efficiency are being introduced. In addition, power consumption is being reduced by inverter control motors. In recent years, the demand for industrial robots has expanded rapidly due to decreases in working populations. These robots use servomotors that can rotate forward and backward for accurate positioning, and the demand is expected to grow. This paper introduces developments in bearings used in high-efficiency motors, inverter motors, and servomotors.

1. Introduction

The power consumption of motors used in various industrial machines is said to account for 40 to 50% of the world's power consumption[1], so societies have called for a reduction of this consumption. In response, high-efficiency motors with higher energy efficiency have been introduced. Another means of reducing power consumption is the inverter motor, which changes rotational speed according to operating conditions.

In recent years, demand for industrial robots has expanded rapidly due to shrinking workforces. These robots use servomotors capable of both forward and reverse rotation and precise positioning, with the expectation that the demand for them will rapidly increase.

This article introduces efforts to develop bearings used for high-efficiency motors, inverter motors, and servomotors, which will be in great demand in the future (Table 1).

Table 1 Industrial machinery motor market requirements and bearing initiatives

Types of industrial machinery motors	Market trends	Environment surrounding the motor	Bearing initiatives
High efficiency motor	· Increased awareness in global environmental protection · Global trends in power consumption reduction	· Regulation of motor efficiency	· Reduction of mechanical loss
Inverter motor	· Energy saving of pumps, blowers, and compressors · Introduction to large manufacturing facilities such as steel and paper manufacturers	· Increased demand for inverters · Higher carrier frequency (higher precision of control)	· Measures against electrolytic corrosion
Servomotor	· Declining working population and automation · Expanded use of industrial robots	· Improvements to encoder resolution · Installation of a brake (to keep the motor stationary)	· Measures against encoder/ brake contamination

2. Low-Torque Bearings for High-Efficiency Motors

2.1 Background of development

Worldwide endeavors to reduce power consumption has led to regulations requiring improvements to motor efficiency. A motor's energy loss comprises iron loss (heat generation from the iron core), copper loss (heat generation from winding), and mechanical loss (in this article: loss due to bearing rotation, excluding wind loss due to cooling fans). Although the mechanical loss can be as small as roughly 1% of motor power consumption, it accounts for 0.4–0.5% of the world's power consumption. Therefore, the social impact of such a reduction would be significant. NSK has thus been evaluating mechanical loss with actual motors and is working to reduce it. As shown in Figure 1, a motor equipped with bearings for evaluation was broken in for 3 hours. The input voltage was lowered from 200 V, and the input power (W) for each voltage was measured. The minimum value of the input power was regarded as the mechanical loss. Also, the cooling fan was removed.

This evaluation method allowed for a direct evaluation of the mechanical loss, and it became possible to use this approach to develop customers' motors.

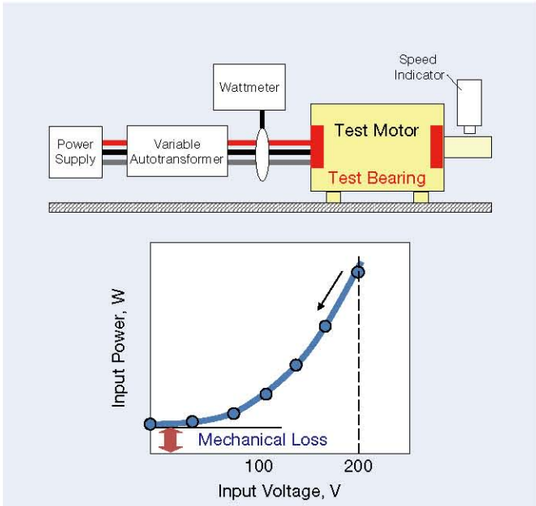

Fig. 1 Mechanical loss evaluation method

2.2 Product features

Figure 2 shows the components of the mechanical loss.

Under the conditions of a rated rotational speed of 3 000 rpm for the 2P motor, the cause of approximately 80% of the mechanical loss turned out to be lubrication resistance due to the shearing and agitation resistance of grease between the bearing parts. As a result, we thought that reducing the mechanical loss would help to reduce the lubrication resistance. We focused on the type and amount of grease as well as the cage shape and proceeded to optimize them.

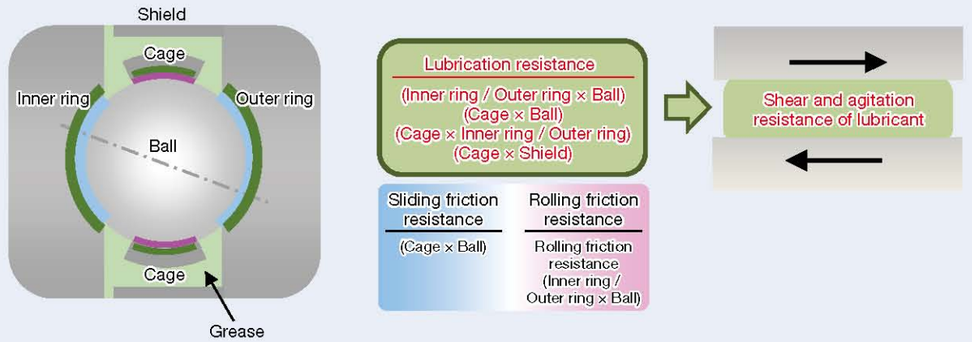

	Composition*	Bearing design	Grease type	Amount of grease	Cage type
Lubrication resistance	80 %	×	◎	◎	◎
Sliding friction resistance	20 %	×	×	×	○
Rolling friction resistance		○	×	×	×

*2P motor (3 000 rpm) condition

Small influence ← × ○ ◎ → Large influence

Fig. 2 Bearing mechanical loss factor

2.3 Evaluation results for the developed product

Figure 3 shows the results of the mechanical loss with the developed bearing. As a result of this test, optimizing the grease filling quantity reduced the mechanical loss by 60% compared to conventional bearings. In conventional bearings, reducing the grease content tends to break the oil film and shorten the grease seizure life. The bearing developed using NSK's special grease, which has excellent seizure resistance, reduced mechanical loss by 60%, compared to conventional bearings, and at the same time has achieved 2.7 times the grease seizure life.

Figure 4 shows the test results for the effects related to the number of motor poles (rotational speed). The results show that a 4P motor has less mechanical loss than a 2P motor. This is due to the rotational speed of the 2P motor (2P: 3 000 rpm, 4P: 1 500 rpm) being slower than that of the 4P motor. This test's mechanical loss reduction rate was 50% for the 2P and 27% for the 4P. This rate difference is likely due to the low ratio of the lubrication resistance to the mechanical loss (Figure 2: 80% in the 2P motor) for the 4P motor with slow rotational speed.

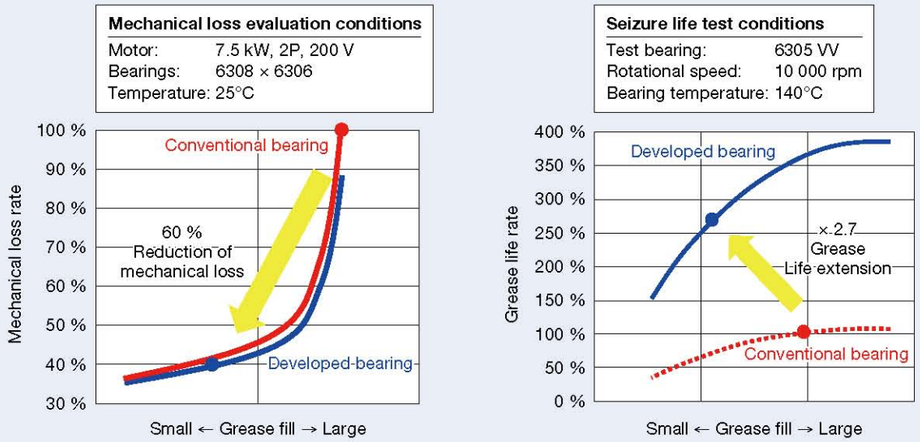

Fig. 3 Mechanical loss and grease seizure life of low-torque ball bearings for high-efficiency motors

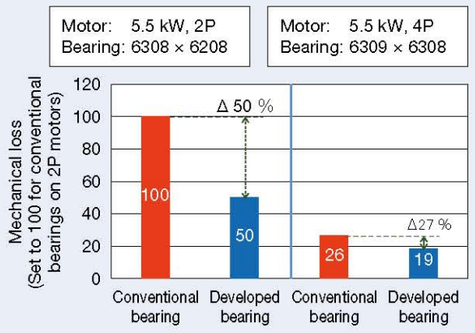

Fig. 4 Mechanical loss rate for the number of motor poles

Low-torque bearings for high-efficiency motors are available in various sizes (outer diameter: ϕ26 mm–ϕ170 mm). These low-torque bearings reduce mechanical loss and allow for longer grease seizure life compared to conventional bearings. Furthermore, plastic cages were confirmed to reduce the mechanical loss by half that of the iron cages (Figure 5). We considered that the plastic cage suppresses grease agitation resistance in the cage pocket and sliding friction resistance between the cage and ball. Also, we expect plastic cages to be used for industrial machine motors since they do not degrade grease due to cage wear and thus contribute to a longer life.

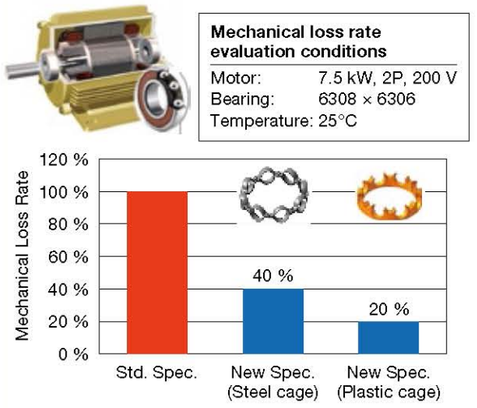

Fig. 5 Mechanical loss rate of low-torque ball bearings for high-efficiency motors

3. Anti-Electric-Corrosion, Ceramic-Coated Bearings

3.1 Background of development

The inverter motor, controllable with the optimum rotational frequency, is useful for energy saving in pumps and blowers as well as product quality improvements in steel and paper manufacturing facilities. The frequency to be controlled (carrier frequency) is increasing so that the motor can be operated with a higher degree of accuracy. As the carrier frequency increases, electrolytic corrosion may occur due to the high-frequency current in the bearing[2]. Electrolytic corrosion is a phenomenon whereby sparks are generated through the lubricating oil film between the raceway surface and rolling elements, causing local melting and unevenness (Figure 6). It also causes an early abnormal sound and seizure. Bearings used for small motors have ceramic balls that do not pass a current, as a measure against electrolytic corrosion. However, there are productivity issues with large ceramic balls. NSK has developed an anti-electrolytic-corrosion, ceramic-coated bearing for an inverter motor, in which a ceramic spray material coats the outer ring (photo 1).

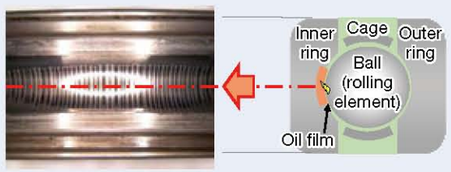

Fig. 6 Electrolytic corrosion of bearing inner ring raceway

Photo 1 Ceramic-coated, electrolytic-corrosion-resistant bearing

3.2 Product features

The newly developed anti-electrolytic-corrosion, ceramic-coated bearing is excellent for electrical insulation since the high-productivity alumina ceramic spray material coats the outer ring. Furthermore, it has fewer voids in the ceramic-coated area than the general ceramic-coated bearing and is highly durable due to the dense coating (Figure 7).

3.3 Evaluation results for the developed product

As a result of evaluating the electrical insulation, the developed product has about ten times as much insulation as the general ceramic-coated bearing with the DC power supply. The developed product has equivalent or better insulation with the AC power supply, satisfying an impedance of 100 Ω or more at 1 MHz of high frequency, which IEC TS60034-25:2014 recommends (IEC2014) (Figure 8).

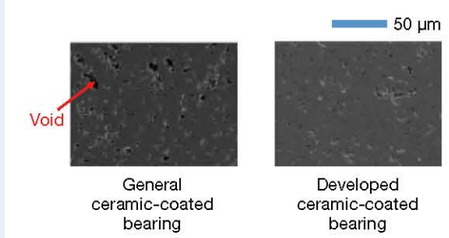

Fig. 7 Cross section of a ceramic-coated part

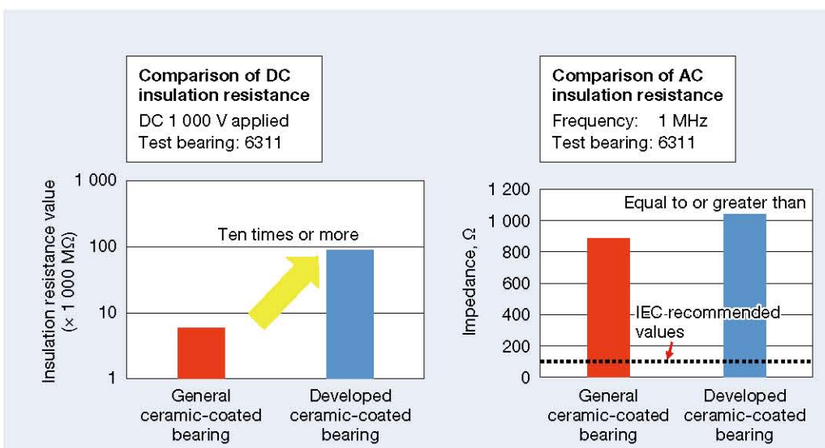

Fig. 8 Electric insulation performance of the developed ceramic-coated bearing

In terms of mechanical properties, the impact resistance of the coating is about three times that of a general ceramic-coated bearing (Figure 9) and is easy to handle.

Heat dissipation, which is a disadvantage of ceramic coatings, can be suppressed by a relatively dense coating compared to general ceramic-coated bearings. Therefore, it can be expected to extend both the lubricant life and the motor life. The temperature rise during bearing rotation was lower by about 10°C when compared to the general ceramic-coated bearing (Figure 10).

The anti-electrolytic-corrosion ceramic-coated bearings are available in a lineup of bearings (outer diameter: ϕ130 mm–ϕ230 mm) suitable for medium and large motor sizes.

4. Low Particle Emission Bearings for Servomotors

4.1 Background of development

The servomotors' precise positioning is performed by transmitting or reflecting the LED's light emission signal in the pattern engraved on the encoder plate and feeding the received signal back to the motor controller. Contaminating the encoder plate's surface by oil or other matter disables the signal reception and feedback of the position information to the motor controller, preventing regular operation. In a servomotor used for a robot, it is necessary to stop the arm and the workpiece via the electromagnetic brake. At this time, contaminating the brake plate with oil or other matter causes brake slippage. Servo motors used in industrial robots are required to be highly reliable, so bearings must have low particle emission and do not contaminate encoders or brakes[3].

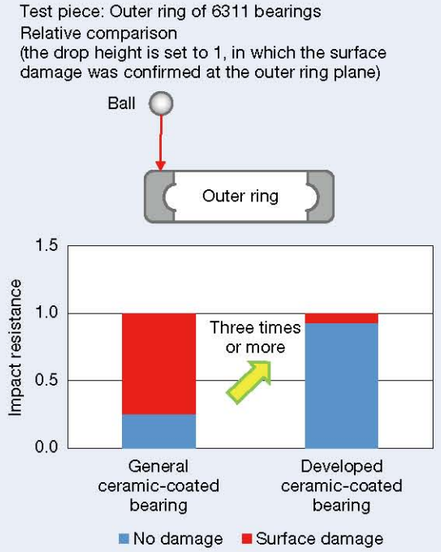

Fig. 9 Mechanical strength of the developed ceramic-coated bearing

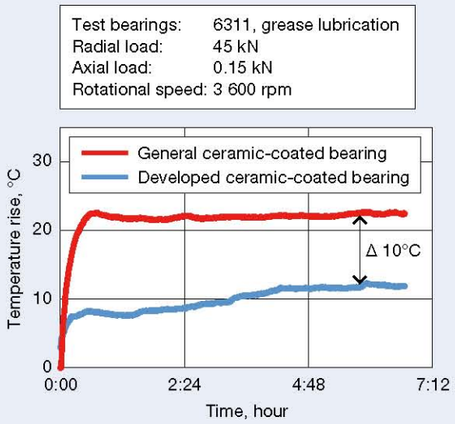

Fig. 10 Heat radiation performance of the developed ceramic-coated bearing

4.2 Product features

The low particle emission bearing for servomotors uses a low particle emission LGU grease with optimized grease composition as well as a high-sealing, light-contact DW seal (Figure 11).

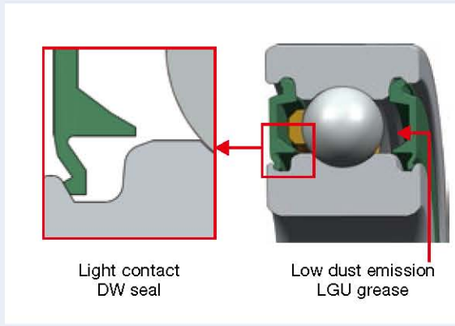

Fig. 11 Bearing with low particle emissions for servomotors

4.3 Evaluation results for the developed product

NSK has carried out several simulation tests to investigate the relationship with the contamination of encoder brake plates by the scattering of bearing internal grease. Figure 12 shows the results of the visualization of scattered particles by laser irradiation. In a non-contact seal with conventional grease, many particles scattered from the gap between the rotating bearing inner ring and seal were observable, simulating the grease's contamination path scattered from the bearing. Tests have confirmed that the scatter amount decreases in the bearings with a non-contact seal and a low particle emission LGU grease. Furthermore, in the bearings filled with LGU grease in a light contact seal, scattering of grease was hardly observed.

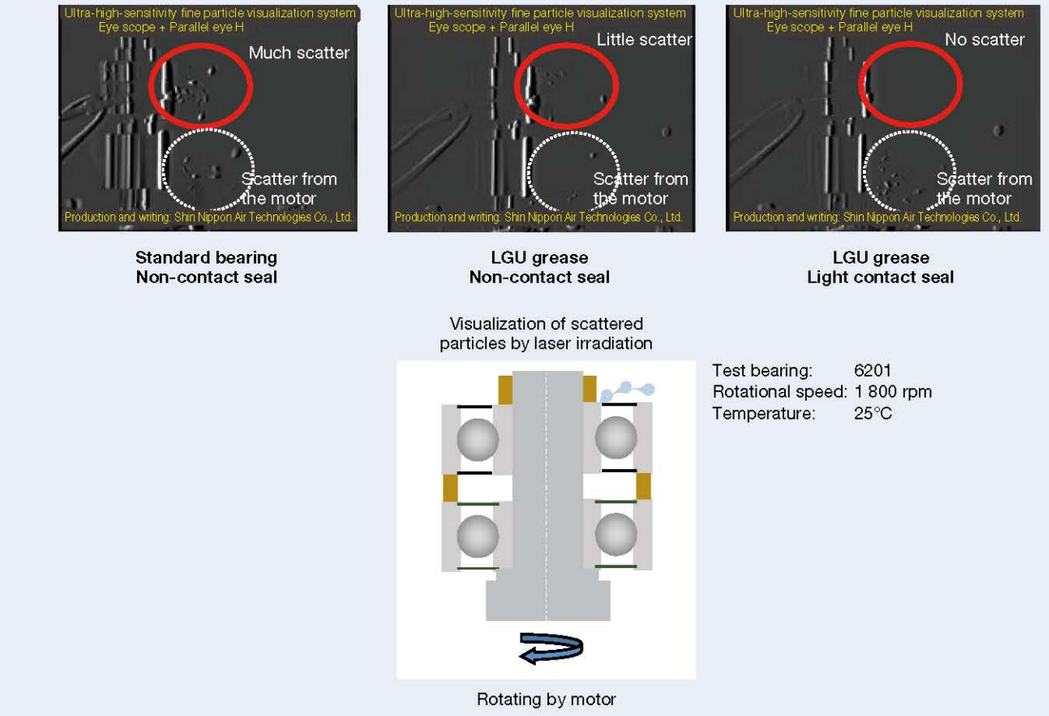

Fig. 12 Bearing grease scattering visualization test

Figure 13 shows a test to quantify the contamination of the encoder plate or brake plate due to grease splattering. This is a method in which a shaft with a disc that imitates an encoder or brake plate is supported by a test bearing and rotated for a certain period of time by an external motor to evaluate the contamination of the disc after rotation. Contamination quantification was performed by image analysis of the proportion of contaminated areas in a particular area of the disc. As a result of the test, it was verified that the low particle emission LGU grease has less adhesion to the disk than the standard grease and that the grease with the low particle emission is effective as a countermeasure against encoder contamination. Furthermore, when the light contact DW seal was combined, there was almost no adhesion under the test conditions.

The low particle emission bearings for servomotors, which are packed with LGU grease and employ light contact DW seals, are available in a lineup of bearings (outer diameter ϕ 26 mm–ϕ 120 mm) suitable for the motor size. Consequently, these bearings are now highly regarded by users.

5. Postscript

This article introduced the challenges of the technological development of bearings used for high-efficiency motors, inverter motors, and servomotors. Through the development of bearings, we hope to contribute to energy savings in motors and the reduction of the life cycle costs of machines.

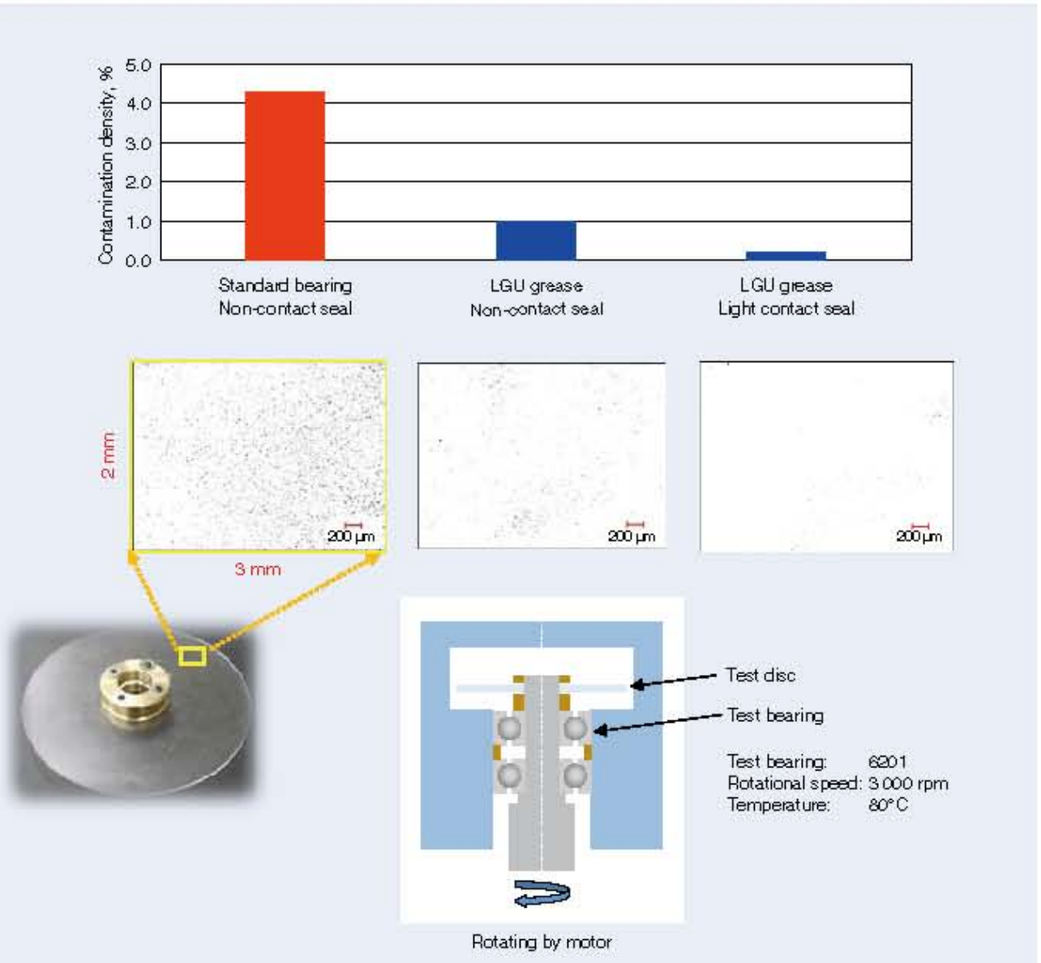

Fig. 13 Disc adhesion simulation test

References

1) "Top Runner Motor," The Japan Electrical Manufacturers' Association (2015).
2) K. Yasunaga, "Electric Erosion of Motor Bearings," *NSK Technical Journal*, 686 (2013) pp. 40–45.
3) H. Ishiguro, "Technical Trend of Industrial Machinery Bearings," *NSK Technical Journal*, 691 (2019) pp. 13–18.

Katsuaki Denpou

High Load Endurance Test Unit for Electric Injection Molding Machine Ball Screws

Akihiko Ishikawa
Industrial Machinery Linear Technology Center, Research Department
Ken Namimatsu
Japan Sales and Marketing Division-Headquarters, Sales Engineering Department
Noriaki Sekiya
Japan Sales and Marketing Division-Headquarters, Nagano Branch

Abstract

A high load endurance test unit for electric injection molding machine ball screws was recognized by the Japanese Society of Tribologists in May 2020's "Tribological Heritage #18." This test unit was developed in 1990 to evaluate the rolling fatigue life of ball screws under the high load conditions found in such machines. The unit features:

1. An endurance test that simulates the injection unit of an electric injection molding machine (maximum load: 300 kN, fluctuating load, short stroke).
2. A test load on the load cell that can be constantly monitored.
3. A simple and compact structure that achieves high load testing.

This was a groundbreaking test machine for the time thanks to its unique configuration that matched the development of ball screws for electric injection molding machines. The test unit is recognized for laying the foundation for endurance evaluations of these specialized ball screws and contributing to the electrification of industrial machinery. The test unit is now on exhibit in the NSK showroom.

1. Introduction

Injection molding machines produce most of the many plastic products in our everyday lives, such as home appliances, automobile-related items, IT equipment, electronic components, food containers, medical equipment, and sports goods. Hydraulic injection molding machines had until recently been quite common. However, with the promotion of electrification and from the viewpoint of energy-saving and environmental protection, in the 1980s an electric injection molding machine was introduced and used as an electric servo mechanism for the positioning of machine tools . Since then, to cope with the great diversity of needs for plastic products, performance enhancements (higher speeds, precision, and quality, greater energy savings, etc.) are being attempted for electric injection molding machines.

The ball screw is one essential part of an electric injection molding machine. However, unlike positioning applications such as machine tools, the injection part mechanism of electric injection molding machines is used to transmit force. A high load of several hundred kN, which is more than one order of magnitude larger than the load used in machine tools, works on the ball screws. Therefore, the durability of ball screws represents a problem. Even under harsh conditions, maintaining its durability for an extended period created a need for ball screws with a higher loading capacity and longer life.

The high-load durability testing machine for ball screws used in electric injection molding machines responded quickly to that need and a foundation was established for evaluating the durability of ball screws for this application, which has contributed to the development of electric industrial machines such as those for injection molding.

This high-load durability testing machine was recognized as the 18th Tribology Heritage of the Japan Society of Tribology, introduced in this article. At present, the testing machine is on display in NSK's showroom (Photo 1).

2. Ball Screw High-Load Durability Testing Machine

2.1 Durability testing machine for general ball screws

NSK has accumulated several systematic life tests using durability testing machines with multiple nuts on one shaft, as shown in Figure 1, to evaluate and confirm the life of ball screws used in machine tools and for other machines. Coil spring provides a constant load (roughly several tens of kN) to evaluate the lifespan (total number of revolutions) under these conditions.

These numerous test results have established the lifetime calculation formula for ball screws under normal operating conditions, and the market has confirmed the validity of those results.

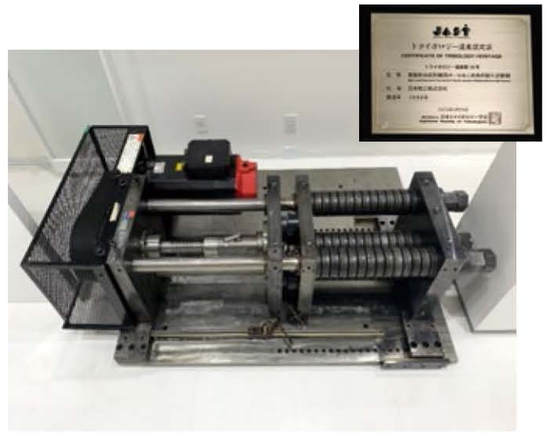

Photo 1 High-load durability testing machine of ball screws for electric injection molding machines and certification

2.2 Problems with ball screws in electric injection molding machines

In the 1980s, several injection molding machine manufacturers in Japan started developing electric injection molding machines. These were a breakthrough at the time, but there remained a number of problems to be solved[1, 2]. One of these was related to ball screw durability. Photo 2 shows the damage that ball screws were incurring at the time. The grease quickly turned black, and significant flaking occurred. If the ball screw is used continuously after flaking, the result will be poor circulation of the balls and the machine will lock up (stop).

Figure 2 shows an example of the electric injection molding machine's arrangement and the ball screws used for it. The ball screws used for the injection axis have a small stroke of several tens of mm and are in use under the especially severe conditions of repeated high load.

Consequently, under the conditions of high load and small stroke in the injection axis and other parts, the ball-screw life-calculation method, which had been in use for evaluations up to that point in time, could no longer be applied. This led to an urgent need to carry out a durability evaluation under those conditions in order to set out new ball screw specifications as well as a life calculation method.

2.3 Features of the high-load durability testing machine

Ball screws for the injection axis are used under conditions such as fluctuating loads up to several hundred kN as well as a short stroke, requiring a testing machine capable of reproducing such load conditions. This durability testing machine manufactured in 1990 has a timing belt connecting a servo motor to a ball screw, which rotates the screw shaft and moves with a nut. A disc spring unit provides the load, the maximum of which can be 300 kN, and three load cells placed in the center detect the actual load. This allows for durability tests for electric injection molding machines. Figure 3 shows the structure and load pattern.

In this test machine, a disc spring unit provides a high load and a variable load, and a ball screw, which is a test sample, runs by itself, producing a test load, which is a feature, unlike conventional durability testing machines. The conventional durability testing machine set the spring's displacement to apply a constant load. However, in the high-load durability testing machine, three load cells detect the actual load described above since the load fluctuates. Furthermore, adjustments can prevent the unbalanced load from acting on the ball screw to obtain stable test conditions.

As a result, it is possible to carry out an accurate durability evaluation even during a high load test. Additionally, the test machine is compact and straightforward, and maintenance is easy to perform.

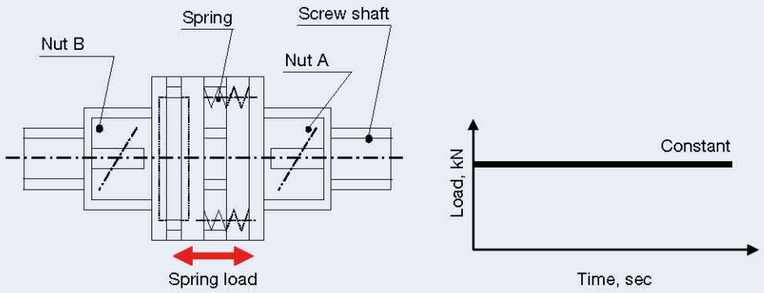

Fig. 1 Endurance testing machine with three ball screws arranged in a series

Photo.2 Ball screw damage in the early stage of electric injection molding machines

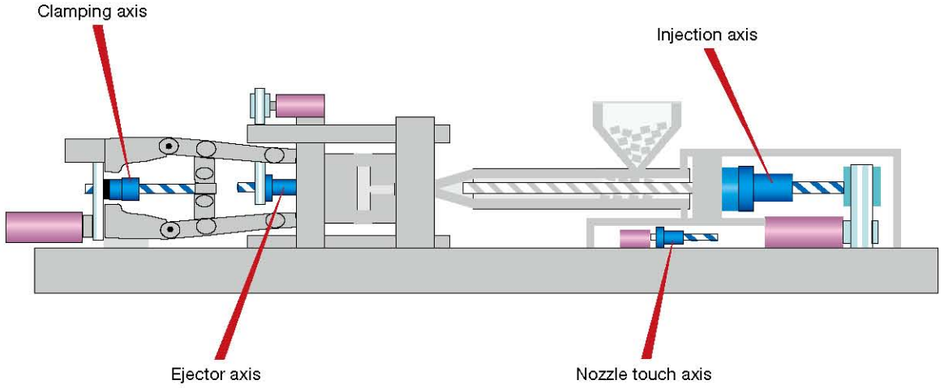

Fig. 2 Applications of ball screws in an electric injection molding machine

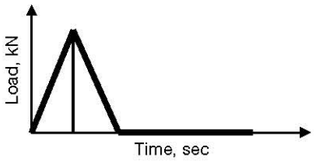

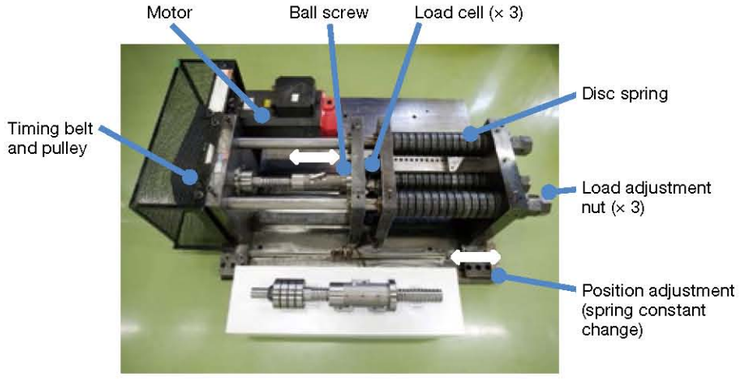

Fig. 3 Structure of a high-load durability testing machine with ball screws for an electric injection molding machine

3. Development of Ball Screws for Electric Injection Molding Machines

NSK has developed the HTF Series of ball screws for the high-load drive of electric injection molding machines after conducing high-load durability tests, analyzing issues related to the ball screws, and performing a number of other tests and evaluations.

The high load capacity of the HTF Series was made possible with the following design specifications and corresponding production and processing technologies.

· High load design

Increasing the ball diameter to the limit, increasing the number of effectively loaded balls, and optimizing the ball groove shape.

· Uniform nut load distribution

Making the phases of the ball circulation paths by 180° opposite allows for a radial balance. Also, we recommend an installation that balances out the effects of axial expansion and contraction of the screw shaft and nut due to a high load.

While developing the HTF Series, we carried out durability tests by varying the load (contact pressure) and stroke using this durability testing machine. Figure 4 shows some of the test results. It turned out that the surface pressure and the stroke due to the load significantly affect the durability of ball screws.

With these results, a life calculation formula was derived using surface pressure and the stroke coefficient by modifying a general calculation formula of the rated fatigue life[3].

Subsequently, we were able to develop the HTF Series of high-load drive ball screws for electric injection molding machines (photo 3). As a result of this development, the application of electric injection molding machines has expanded, requiring increases in speed and load. However, more durable ball screws (HTF Series) are needed in order to satisfy these needs.

In the injection molding machine, a high load works on the ball screws, deforming the machine stand. Unlike with machine tools and other machines, this unbalanced load on the ball screws tends to increase the ball's load. The lubricant's base oil viscosity may decrease due to heat generated by continuous operation under high loads, metallic contact between balls may cause abnormal wear, and poor circulation, such as ball clogging due to a small stroke, may cause damage. As a countermeasure against these problems, inserting retaining pieces between the balls eliminated the metal contact. Figure 5 shows the results. The results were confirmed using a high-load durability testing machine.

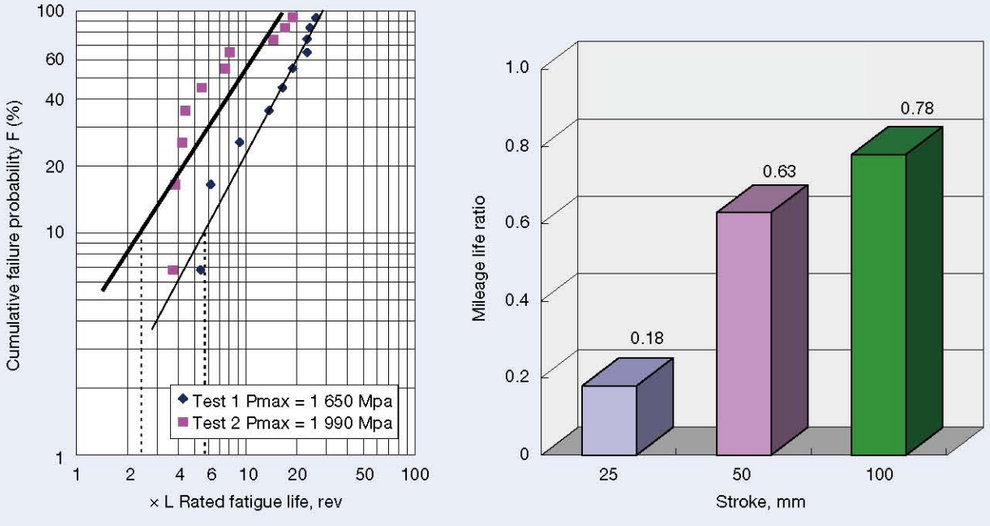

(a) Impact of high surface pressure (load) on life

(b) Impact of small stroke on life

Fig. 4 Durability test results

Photo 3 HTF series of ball screws for high-load drive

Based on this development, we expanded the HTF-SRC Series of ball screws for high speeds and high loads, which use retaining pieces and are compatible with high-cycle machines (Photo 4).

Moreover, we were able to increase the durability of the ball screws for electric injection molding machines.

Photo 4 HTF-SRC series of ball screws for high-speed high-load drive

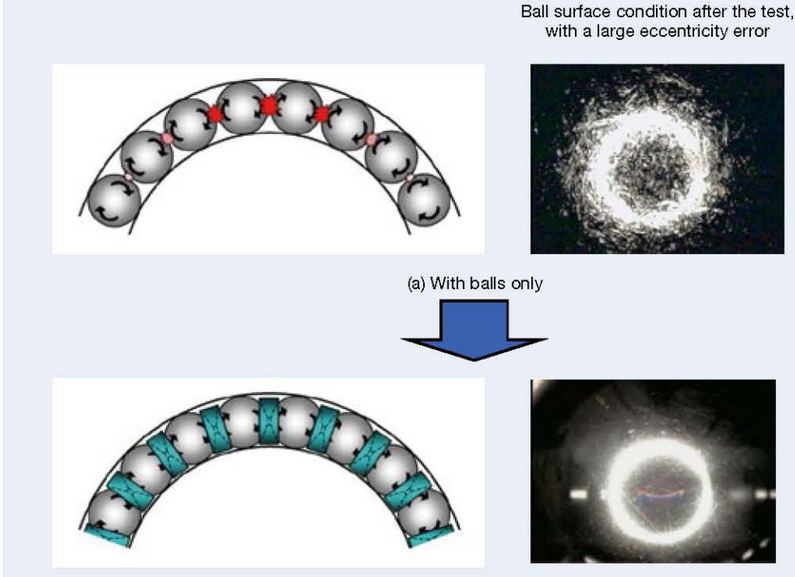

Fig. 5 Effect of the ball retaining piece

4. Conclusion

Along with greater demand for electric injection molding machines, advancements are being made to increase their performance in terms of higher loads and speeds as well as longer life.

The NSK ball screw high-load durability testing machine is now capable of higher loads and speeds, and progress is continuously being made to overcome related problems.

In the future, the application of ball screws will expand further, and operating conditions will be even more severe. In light of this, we will continue to promote ball screw development and evaluation so that ball screws can operate stably even in such conditions.

References

1) Y. Inaba, "Development of the electric servo injection molding machine," Thesis (1998) pp. 10–13.
2) Y. Inaba, "The electric servo injection molding machine and precision molding" (1999) pp. 28–29, The Nikkan Kogyo Shimbun, Ltd.
3) M. Ninomiya and K. Miyaguchi, "Recent Development of Ball Screws," *NSK Technical Journal*, No. 664 (1997) pp. 9–10.

Akihiko Ishikawa

Ken Namimatsu

Noriaki Sekiya

Mobile Extendable Robot Arm (MERA)

Seiichi Teshigawara
New Field Products Development Center Technology Development Department 1
Haruhiko Harry Asada
Massachusetts Institute of Technology, Mechanical Engineering

Abstract

Maintenance and repair often involve climbing up tall ladders and working around risks such as high-voltage power lines, gas pipes, and other physical and chemical hazards. Using ladders to conduct inspections comes with significant risks; falls from ladders account for a large portion of occupational accidents every year. Even though the tasks are easy and repeatable, they are still not automated. The Mobile Extendable Robot Arm (MERA) is a movable robot arm with a novel extendable mechanism for reaching high places and positioning an end effector. MERA is composed of a locomotive vehicle combined with a rotation table and a two-layer, two-degree-of-freedom (2DOF) scissor mechanism. In this paper, we present the design of the scissor mechanism and a singularity analysis. Based on the analysis of the singularity found in the 2-DOF scissor mechanism, we propose two novel solutions to the problem.

1. Introduction

In large buildings such as hospitals or schools, a lot of equipment as well as pipes, air ducts, and electrical supply systems are in the walls or ceilings. When inspecting and maintaining equipment in high places like ceilings, tools such as ladders and stepladders are widely used. On the other hand, because the equipment is easy to use, people tend to be less cautious about falling and other hazards. Consequently, ladders and the like are ranked as the number one cause of such accidents[1].

When we think about work using ladders in indoor facilities, there is a lot of relatively simple inspection work done through ceiling openings and fluorescent light replacements. Accidents caused by falls should be reduced as much as possible, as some cases lead to severe injury or death, despite the work being so simple. Photo 1 was taken at the Massachusetts Institute of Technology (MIT) campus. The worker stands on a ladder and works alone with his upper body in a narrow space of the ceiling, which is about 2.5 (m) off the ground. This work is not limited to the MIT campus and is often seen in various facilities daily. This paper will introduce a Mobile Extendable Robot Arm (MERA). The MERA aims to automate the simple tasks, and reduce the number of industrial accidents.

As a previous work, a method based on taking camera images using a small drone has been proposed for the automation of inspection work in high places. However, there are limitations such as payload, flight time, and difficulty in accurate positioning. To solve this problem, we propose the use of an extendable mechanism to access the ceiling from the floor. As examples of the extendable mechanism, a scissor mechanism used for a lifter, a zipper[2,3], a chain[4], and a belt[5] have been proposed. They have both high rigidity and extendability. However, they can only be deployed vertically, and it is impossible to access the workspace where there is an obstacle around or below, as shown in Figure 1. On the other hand, the proposed TSE[6] (Triple Scissor Extender) and TSERA[7] (Triple Scissor Extender Robot Arm), which use a scissor mechanism, have high degrees of freedom and a high extension rate. However, due to the scissor mechanism's singularity problem, it is difficult to expand when in a completely closed posture. This restriction prevented the achievement of an adequate level of the extension ratio of the scissor mechanism.

This paper proposes a small, two-degree-of-freedom scissor mechanism, provides an analysis of the singularity problem of the scissor mechanism, and presents two methods for solving the technical issue. We also present a two-layer scissor mechanism as an application of this method.

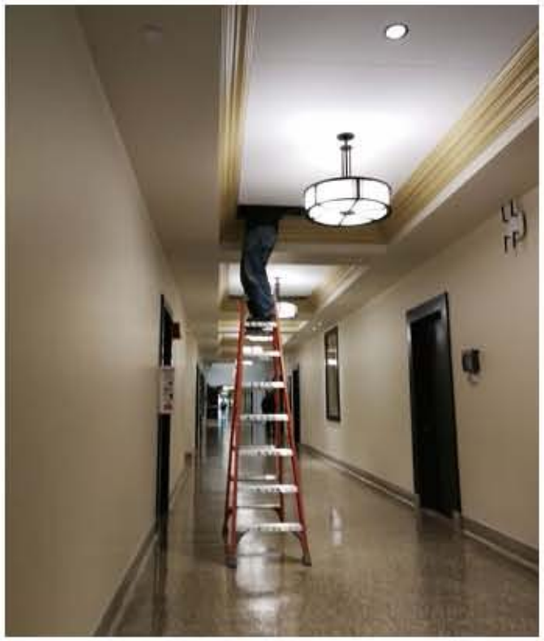

Photo 1 Maintenance task using a ladder

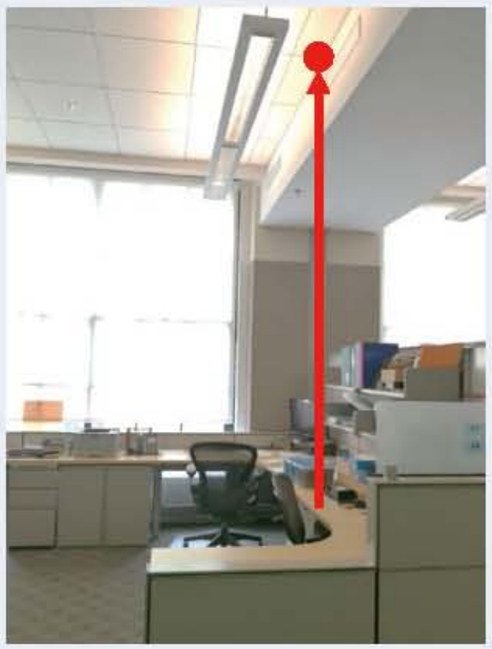

Fig. 1 Air duct difficult to access due to obstacles such as desks and chairs

2. Extendable Actuator

2.1 Configuration and features

The *scissor* mechanism in *scissor* lifts is characterized by high rigidity and a high extension ratio. However, as pointed out in the first section, the working area is limited to straight lines because it can only extend or contract only upward. Therefore, here, we propose a two-degree-of-freedom *scissor* mechanism with rotational degrees of freedom in addition to the extending motion (Figure 2).

Although the structure is straightforward, the point is that the two links at the base can rotate independently on the same shaft, and the combination of these two links allows both extending and rotary motions. Specifically, when two base links rotate in the same direction and at the same speed, they rotate while maintaining the same length, and when rotating two base links at the same speed and in different directions, they only extend. In other words, controlling the rotational direction and speed of the two base links enables extending and rotary motions with two degrees of freedom on a plane (Figure 3). This type of drive system, in which two actuators work together and generate motion, is generally called an "Coupled Drive". This driving method allows for reducing the overall size and weight of the device[8]. In this paper, we call the combination of the two-degree-of-freedom *scissor* mechanism and actuators for driving an "extendable actuator." Depending on the linkage's width and length, the extendable actuator can achieve an expansion ratio of approximately eight. Furthermore, since the motors to drive the *scissor* mechanism, can be concentrated at the base, it is easy to miniaturize the whole system. These features make it compact when moving and deployable whenever necessary to perform work at the required location.

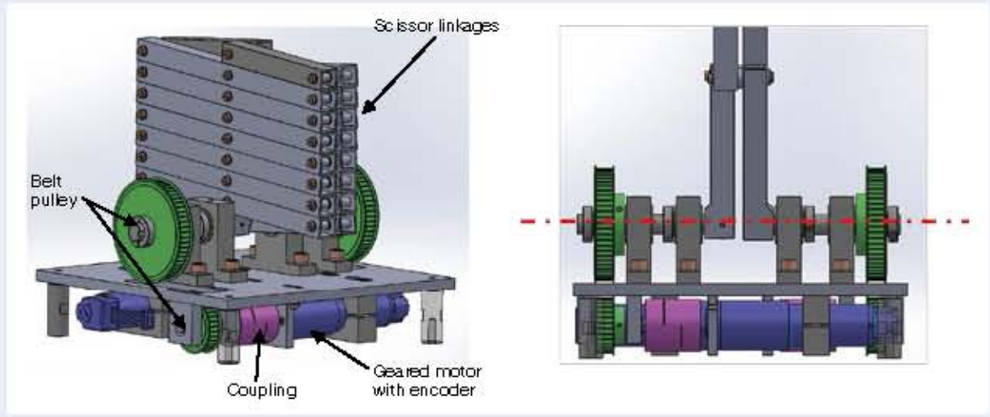

Fig. 2 Structure of extendable robot arm

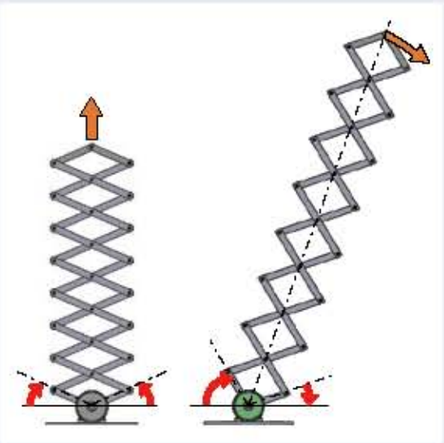

Fig. 3 Principle allowing extending and rotating motion

2.2 Movable range

As shown in Figure 4, when the linkages forming a parallelogram is defined as the first segment, and the length of one side of this parallelogram in the first segment is l_1, the forward kinematics in the n-segment scissor mechanism provide the following equations (1) and (2). Thus, with two motor angles (q_1 and q_2) given, the tip position (x_n, y_n) of the n-th segment scissor mechanism can be obtained.

$$x_n = \frac{1}{2}\mathbf{L}\left(\cos q_1 - \cos q_2\right) \quad \cdots\cdots\cdots (1)$$

$$y_n = \frac{1}{2}\mathbf{L}\left(\sin q_1 - \sin q_2\right) \quad \cdots\cdots\cdots (2)$$

Where $\mathbf{L}$ is $\mathbf{L} = 2\Sigma l_i$. Figure 5 is the result of calculating the movable range of the prototype extendable actuator based on this equation. For the prototype extendable actuator, the number of segments is n = 8, each linkage length is the same, l_1, ..., l_8 = 125 (mm), and the linkage width is w = 20 (mm). The maximum reach distance is 2 100 mm, the length at contraction is 270 (mm) (including the motors), and the expansion ratio is about 8. As shown in Figure 5, the general scissor mechanism is clearly limited to a linear motion, while the extendable actuator provides access to a larger area.

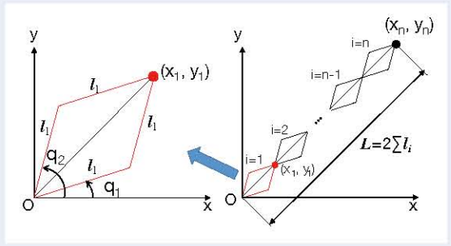

Fig. 4 Cartesian coordinate model of an ideal n-stage 2-DOF scissor mechanism

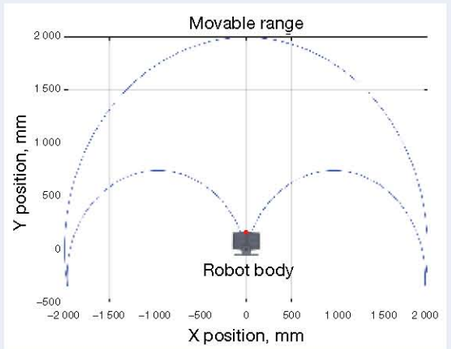

Fig. 5 Movable range of the prototype extendable robot arm

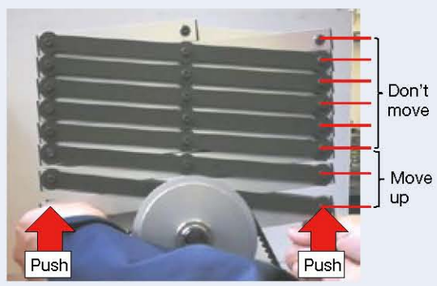

Fig. 6 Scissor mechanism singularity

3. Singularity and Analysis of the Scissor Mechanism

3.1 Singularity Posture

As shown in Figure 6, when trying to expand the prototype extendable actuator upward, only the first segment below the scissor mechanism expanded, while the second segment expanded by about half of the first segment, and the linkages after the third segment did not expand. Even trials with more force could not expand the scissor mechanism. Theoretically, since the linkage lengths are the same, the following linkages should expand uniformly with the displacement given in the first segment. We hypothesized that the scissor mechanism in a singularity due to the linkage's deflection or a small gap in the joint caused this. We also investigated the cause of this phenomenon by using a simulation model.

3.2 Singularity analysis

The modeling of the scissor mechanism considered each linkage's deflection and the gap in each joint based on the analysis method on the free body diagram (FBD) of Chikahiro et al.[9] The paper[10] explains the modeling details. Therefore, in this paper, we show only the result of analysis using the simulation model. This simulation model can analyze the necessary motor torque to expand the scissor mechanism, the forces on each joint, the deflection of the whole structure, and the joint's gap. The gap at the joint includes the following.

- Radial clearance of ball bearings
- Elastic deformation of the balls in the ball bearing
- Clearance between the ball bearing and its housing
- Clearance between the shaft and ball bearing inner ring

Ideally, individual parameters should be set for each of these. However, for the sake of simplicity, we set a parameter Ga (mm), which is assumed to be the same for all joints of the scissor mechanism, and carried out simulations. The simulation parameters are set as follows based on the prototype extendable actuator.

- Material: aluminum 6 063-T5
- Density : 2 690 (kg/m^3)
- Young's modulus: 68 600 (MPa)
- Cross section shape: hollow square pole (20 mm × 20 mm, internal dimensions: 16 mm × 16 mm)
- Weight of joint (shaft + bearing + spacer): 21 (g)
- Number of segments of scissor mechanism: n = 8
- Linkage length : l_1, l_2, l_3, ..., l_7, l_8 = 125 (mm)
- Linkage angle when fully contracted: q_1 = 5 (deg), q_2 = 175 (deg) (with respect to the horizontal plane)

Figure 7 shows the simulation results. Figure 7-(a) shows the result when the gap at the joint G_a = 0 (mm), and Figure 7-(b) shows the result with G_a = 0.05 (mm). In the case of zero gap, when the angle between the base

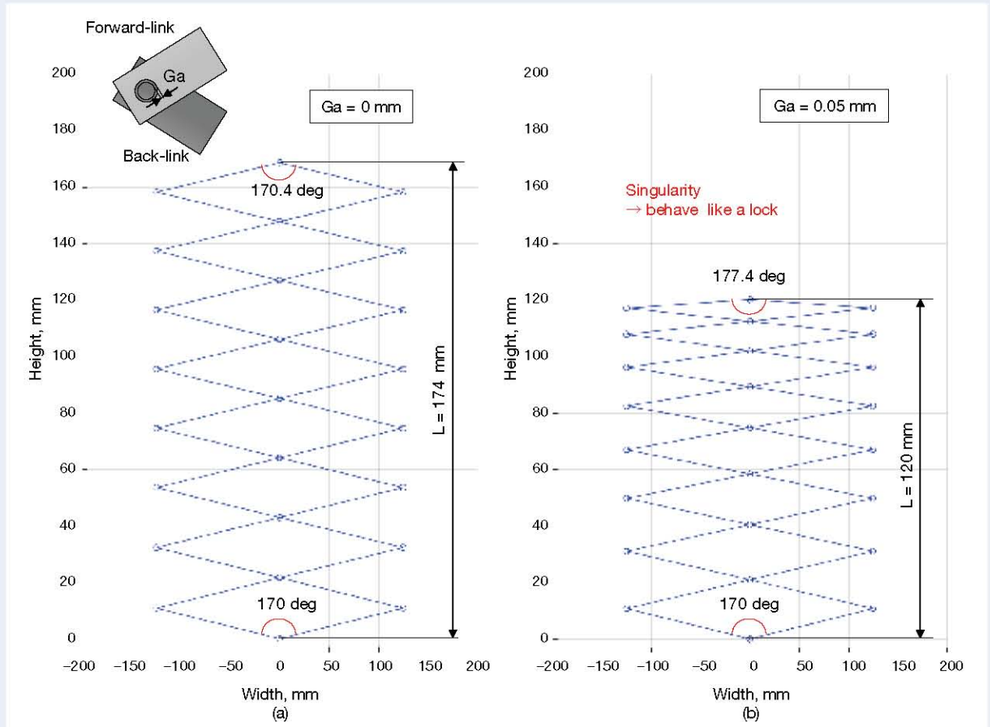

Fig. 7 Simulation results

linkages was 170°, the angle between the tip linkages was 170.4°, and the difference was only 0.4°. The deflection of each linkage due to its weight caused this difference, but its influence is quite small. This means that all linkages can open and close uniformly by driving the base linkages. On the other hand, as a result of considering the gap of 0.05 mm, in Figure 7-(b) the angle between the tip links is 177.4°, while the angle between the base linkages is 170°. The overall shape is flat. This effect gradually increases upward from the base linkages. This indicates that the farther the linkage is from the base linkage, the more difficult it is to expand. The tip linkage angle is very close to the singularity of 180°, i.e., no matter how much driving torque one applies to the base linkage, it is impossible to deploy this scissor mechanism because it behaves like a lock. This is consistent with the previous section's phenomenon, that when applying a force from the base linkages, the linkages after the third row never expand. That is to say, the reason why the prototype extendable actuator could not expand is related to the gap at each joint.

4. Novel Solution for the Singularity Problem

A commercial lift with a multi-segment scissor mechanism solves this problem by using a prismatic actuator in every two or three segments[11]. However, it is difficult to use multiple prismatic actuators in the extendable actuator due to miniaturization and weight reduction. We propose two methods to solve this problem.

4.1 Linkage design approach

This section briefly discusses the phenomenon caused by the gap at the joint with reference to Figure 8. Figure 8-(a) corresponds to Ga = 0 (mm), where the rotational centers of the linkages OA-AC and OB-BC coincide at joints A and B. However, as shown in Figure 8-(b), there is a mechanical gap in the joint in the actual configuration. Even a small gap of Ga = 0.05 (mm) results in shift, point C falls, and angle C increases. This mechanical error increases as the number of segments increases and eventually has a significant impact, as shown in the previous section's analysis results. We also propose a method based on the linkage length design method. Specifically, as shown in Figure 8-(c), the AC and BC linkages are designed to be slightly longer by δl than the OA and OB, assuming there is a gap. As shown in Figure 8-(c), this method prevents point C from falling due to the gap of joints A and B, and creates the same condition as the posture without gap (Figure 8-(a)).

A 3D printer made a miniature model to verify, with an actual machine, the effectiveness of the method. Figure 9 shows a miniature model of two scissor mechanisms. Figure 9-(a) shows a miniature model with the same linkage length (l). Figure 9-(b) shows a miniature model with the pattern shown in Figure 8-(c) with the linkage length adjusted to δl = 0.2 mm. As shown in Figure 9-(a), in the miniature model manufactured with the same length, the upper linkage's opening-closing length is shorter than that of the lower linkages. Figure 9-(b), however, shows that the miniature model produced based on the idea proposed this time opens and closes uniformly. The proposed geometric design method solves the problem of the singularity of the prototype extendable actuator.

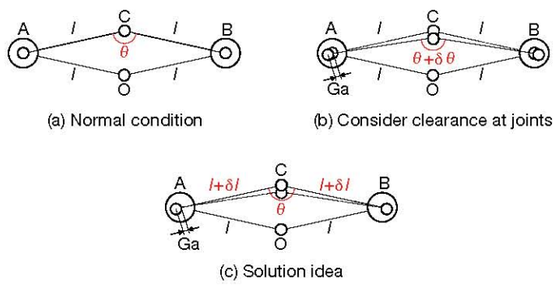

Fig. 8 Singularity schematic and solution

4.2 Mechanical design approach

The linkage design method described above is effective and provides a direct solution to the singularity problem. However, in actual applications, it must be possible to grasp and move an object at the tip while bracing the load of an external force in order to perform the task. When such an external force is applied, the effect on the gap caused by the load fluctuation increases. In other words, when a large load is applied, the displacement is more significant than that assumed, and the extendable actuator is to become a singularity again. That is, in some cases, there is a limit to the geometric design technique alone. Here we propose placing a belt through the linkages for transmitting the angular displacement at the base linkages. This method places a belt pulley and a timing belt inside the linkage for the scissor mechanism, transmitting the base linkage's angular displacement to the following linkages. As the angular deviation increases, the belt exerts a rotational force to assist in opening and closing the extendable actuator. Figure 10 shows the linkage configuration of the proposed mechanism. The linkage (a) and belt pulley (a) are fixed by a pin joint and rotate together around the shaft (b). A bearing inside the pulley (a) and a bearing with a large diameter above the linkage (b) support the pulley (a). The linkage (b), shaft (b), and pulley (b) are connected and fixed to each other. Two bearings in the linkage (a) support the shaft (b). With the above configuration, when links (a) and (b) actively move relative to each other, they are connected and follow the relative motion. Figure 11 shows how the mechanism works. When moving the two links at the base and changing the angle between them from θ_0 to θ_1, the internal timing belt transmits the movement, and the subsequent linkages follow the movement. When applying this system to an extendable actuator, an active

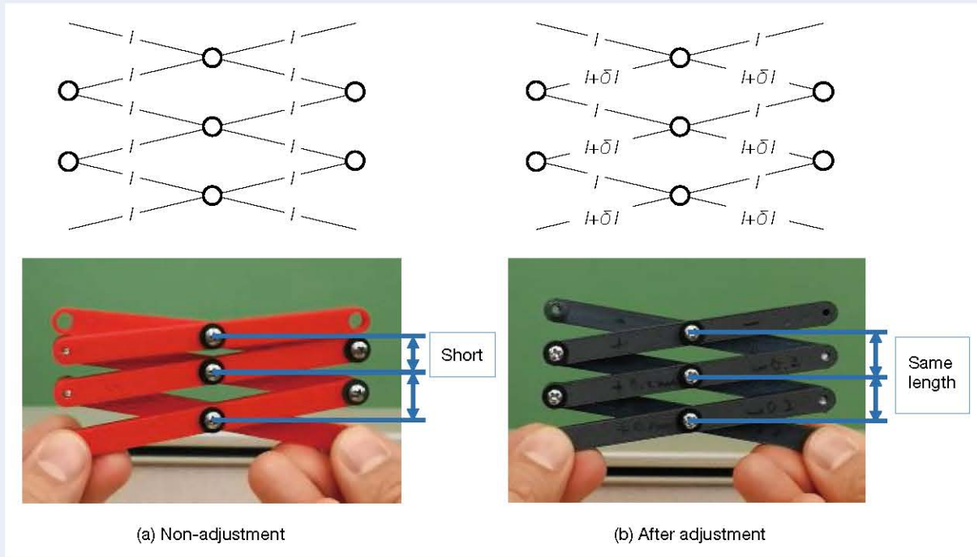

Fig. 9 Miniature models used to (a) verify the effect of joint clearance and (b) confirm our potential solution

base linkage tries to expand, the internal timing belt transmits the link angle, and the following links follow this rotational displacement. In other words, the force acts in the direction of deployment, automatically avoiding the singularity.

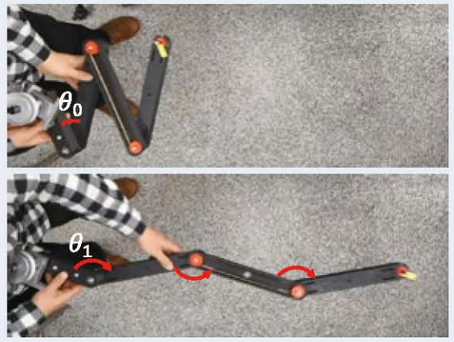

Fig. 11 Movement of the new linkage mechanism, as enabled by the embedded timing belt

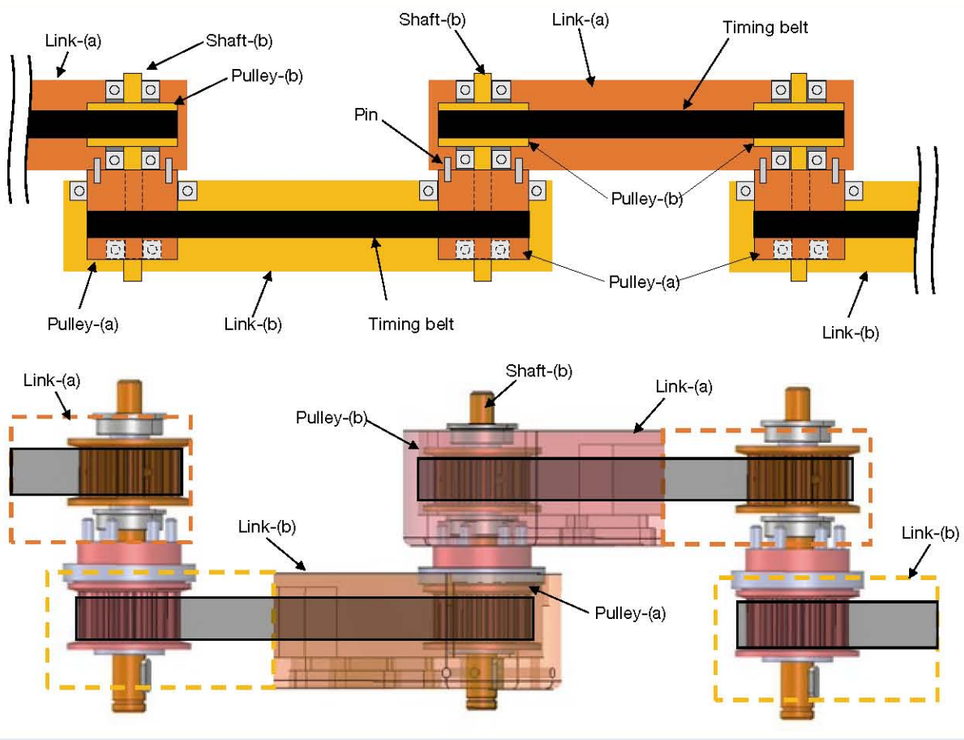

Fig. 10 Mechanism to avoid singularity by using embedded pulleys and timing belts

5. Application to a Mobile Extendable Robot Arm

5.1 System configuration

Figure 12 shows an overview of the Mobile Extendable Robot Arm (MERA). This system is composed of a rotary table and two large and small extendable actuators on a mobile vehicle, with a small WiFi camera mounted at the tip. Each of the large and small extendable actuators has two degrees of freedom and is connected in a series. The first layer extendable actuator has power and a long extendable range (1.5 m) for lifting up the second layer extendable actuator and the WiFi camera at its tip. The second layer extendable actuator, which has a short range (0.5 m), is tiny and provides access to narrow spaces.

5.2 Structure of the two-layer extendable actuator

The two-layer extendable actuator was developed by combining two techniques: a geometric design technique for avoiding the singularity of the scissor mechanism proposed in the previous section and a technique using a transmission mechanism.

The first layer scissor mechanism has two significant roles, one to lift up the second layer scissor mechanism and the other to transmit the torque mechanically to drive the second layer scissor mechanism. As shown in Figure 12, two scissor mechanisms are arranged parallel and connected to each other to realize these roles simultaneously. The scissor mechanism is structurally weak in rigidity in the thickness direction. Adoption of the parallel configuration intends to ensure rigidity. All the linkages adopt the linkage design method for singularity

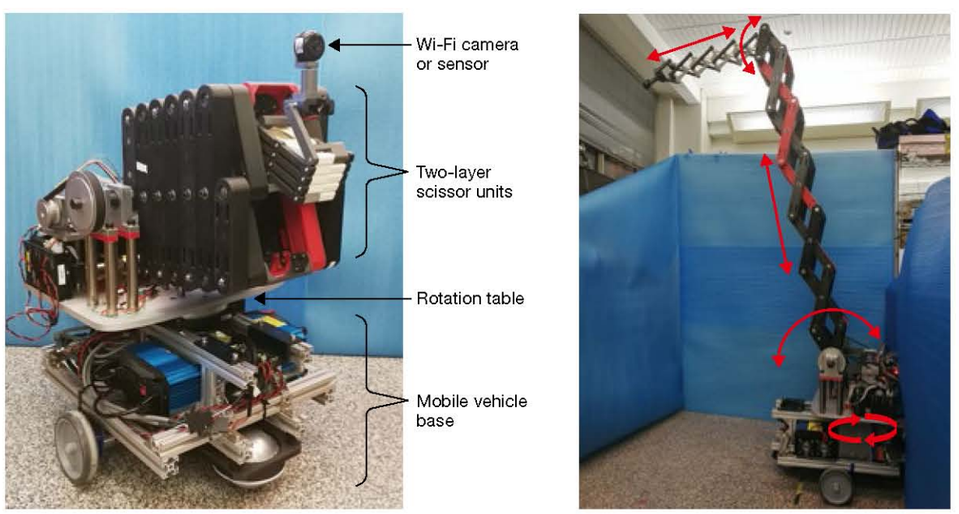

Fig. 12 Mobile Extendable Robot Arm (MERA)

avoidance in Section 4.1. The distance between the left and right shafts of a linkage is 302.1 (mm), and the center shaft shifts by 0.1 (mm) based on the above design method ($\delta l = 0.1$ mm). The first layer of the scissor mechanism also adopted the angular displacement transmission mechanism in Section 4.2. Besides, this mechanism also works only on the serial link. As shown in Figure 13, it is possible to avoid the singularity if only the path (red linkages) of the side constituting the parallel scissor mechanism incorporates the transmission mechanism.

In this case, as shown in Figure 13, the blue link parts out of four paths remain. Therefore, we considered a mechanism for transmitting torque to the second layer scissor mechanism. The components are almost the same as the angular displacement transmission mechanism, but the behavior and the role are different. Figure 14 shows the internal structure of the link for transmitting torque to the second layer. The shaft and pulley are infixed to each other, and a timing belt inside the linkage connects the pulleys. Bearings support the scissor mechanism and the shaft so that movement of the internal pulley does not interfere with that of the linkage. This enables controlling the extension and rotation of the second layer scissor mechanism regardless of the first layer scissor mechanism's position and motion.

Since the second layer scissor mechanism must be compact, only the linkage design method was used for the design. The distance between the left and right shafts of one link is 130.1 (mm), and the center shaft shifts by 0.1 (mm) ($\delta l = 0.1$ mm). Although the parallelization strengthened the rigidity like the first layer scissor mechanism, miniaturization has made the rigidity insufficient. Therefore, we devised a reinforced linkage, shown in Figure 15. Adding the beam strengthened the individual linkage's rigidity, and it can now withstand a load of about 500 (gf).

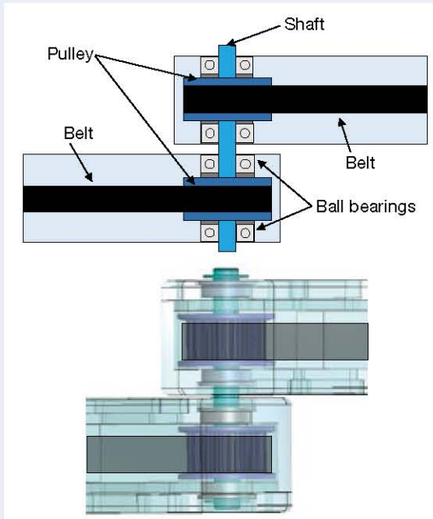

Fig. 14 Mechanism to drive the second layer scissor mechanism

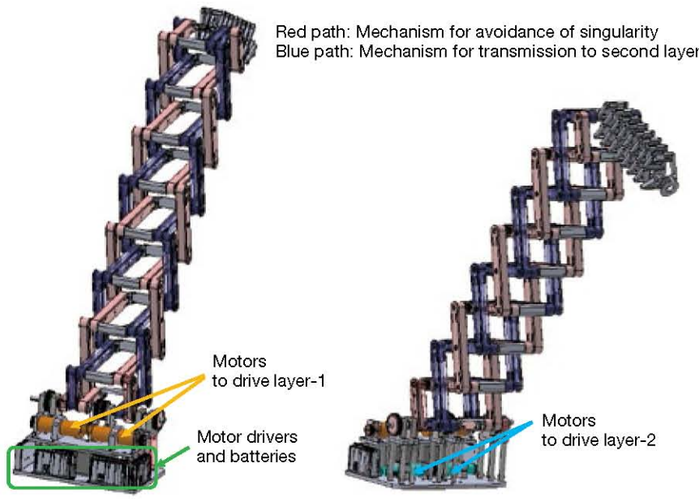

Fig. 13 Structure of first layer scissor mechanism

5.3 Features and applications

The main feature of the two-layer extendable actuator is that a mobile vehicle can house all the actuators and their associated motor drivers and batteries. This reduces the risk of tipping over due to horizontal extension, eliminates the electrical wiring and the risk of wire breakage due to repeated stretching of the scissor mechanism, and is usable even in places where water or chemicals may fall on it if it is waterproofed or stain-proofed.

The two-layer extendable actuator has four degrees of freedom per plane, and two degrees of freedom are redundant. These redundant degrees of freedom enable accessing the desired area at various angles and postures (Figure 16, left). If there is an obstacle, such as a desk, directly below the inspection port, it is possible to avoid the obstacle and access the piping inside the ceiling from the inspection port (Figure 16, right).

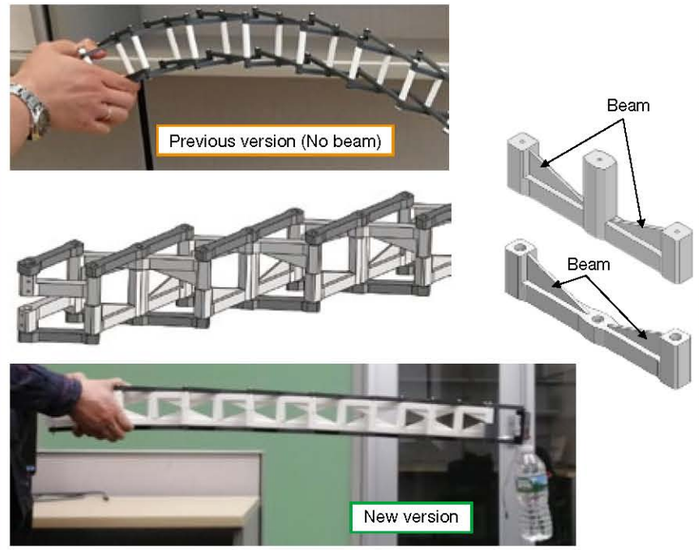

Fig. 15 Structure of second layer scissor mechanism

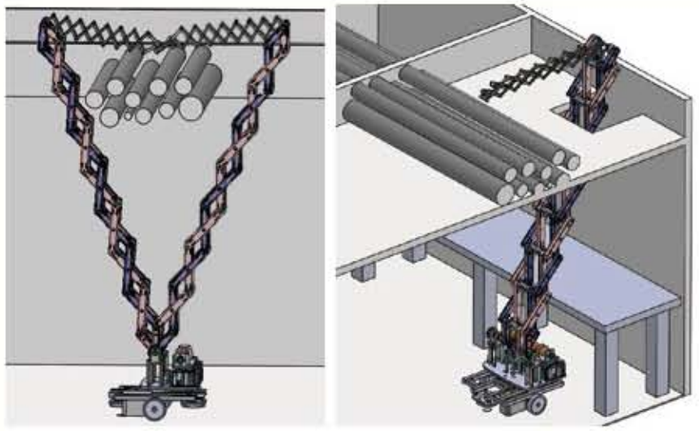

Fig. 16 MERA feature

6. Conclusion

Finally, Photo 2 shows the pipe inspection task in the ceiling performed by the developed robot system as an example of the application. As described in the introduction, many maintenance and inspection tasks involve physical and chemical risks associated with climbing high ladders, high-voltage power transmission lines, and gas pipes. In particular, a task with ladders involves risks such as falls, and accidents involving ladders account for a large portion of occupational accidents every year. Natural disasters, partially or wholly destroyed roofs and ceilings, ruptured pipes, gas, chemical leaks, and tangled wiring also increase the risk of an accident at work. Using robots in work associated with these types of dangers can significantly reduce the risks. It also has the potential to perform more practical tasks, such as taking photographs of joints, wiring, and parts at construction sites and then having experts check them remotely for the quality control. In the future, it will be necessary to develop a system that can automatically perform maintenance tasks by adding an environmental recognition function and a control algorithm of a two-layer extendable actuator. To do this, we need to work together with partners who are both at and outside of NSK. We hope that this paper has helped readers know this technology, and bring an opportunity to co-development.

Photo 2 Example application: inspection task

References

1) From a leaflet published by Ministry of Health, Labor and Welfare Tokyo Labor Bureau https://jsite.mhlw.go.jp/tokyo-roudoukyoku/jirei_toukei/pamphlet_leaflet/anzen_eisei/_123512.html
2) F. Collins and M. Yim, "Design of a spherical robot arm with the Spiral Zipper prismatic joint," 2016 IEEE International Conference on Robotics and Automation (ICRA), Stockholm, 2016, pp. 2,137–2,143.
3) C. D. Woodruff, K. Groah, and G. E. Woodruff, Apparatus and Methods for Providing a Retractable Mast, U.S. Patent 0 261 207, Nov. 23, 2006.
4) J. J. Soerensen, Push-Pull Chain and Actuator, U.S. Patent 8 250 846, Aug. 28, 2012.
5) Joel Bourc'his, Linear Belt Actuator, U.S. Patent 7 270 619, Sep. 18, 2007.
6) D. J. Gonzalez and H. H. Asada, "Design and Analysis of 6-DOF Triple Scissor Extender Robots with Applications in Aircraft Assembly," in IEEE Robotics and Automation Letters, vol. 2, no. 3, pp. 1,420–1,427, Jul. 2017.
7) A. Shikari and H. Asada, "Triple Scissor Extender Robot Arm: A Solution to the Last One Foot Problem of Manipulation," in IEEE Robotics and Automation Letters, vol. 3, no. 4, pp. 3,978–3,982, Oct. 2018.
8) S. Hirose and M. Sato, "Coupled drive of the multi-DOF robot," Proceedings, 1989 International Conference on Robotics and Automation, Scottsdale, AZ, 1989, pp. 1,610–1,616 vol.3.
9) Y. Chikahiro, I. Ario, M. Nakazawa, Theory and Design Study of a Full-Scale Scissors-Type Bridge, ASCE, Journal of Bridge Engineering, 2016, 21(9):04016051.
10) S. Teshigawara and H. Asada, "A Mobile Extendable Robot Arm: Singularity Analysis and Design," in IEEE Intelligent Robots and Systems (IROS), Macau, China, 2019, pp. 5,131–5,138.
11) T. Hongyu, Z. Ziyi, Design and Simulation Based on Pro/E for a Hydraulic Lift Platform in Scissors Type, Procedia Engineering 16 (2011) 772 781.

Seiichi Teshigawara

Haruhiko Harry Asada

Development of an Automated Single-Cell Seeding Device for Biopharmaceuticals

Richard House
Technology Development Department 1
New Field Products Development Center
Technology Development Division Headquarters

Abstract

The use of antibodies for the research and development of new drugs by the biopharmaceutical industry is steadily increasing. Antibody production requires that the producer cells originate from a single cell, and NSK hopes to eliminate one of the uncertainties in the development process by providing monoclonality support data during the seeding operation.

With our machine, the cell never leaves the view of the camera from collection to deposit, a video is recorded of the entire process, and images are saved from key points. Our machine achieves a single cell seeding accuracy of 94% and an operation time of 40 minutes for a 96-well plate.

1. Introduction

In recent years, expectations for biopharmaceuticals have increased in the drug discovery industry. In the research and development of biopharmaceuticals, it is necessary to produce high-quality antibodies using cells as the raw material for their production[1) 2)].

In order to ensure the quality of the antibody, it is necessary to prove that all the producer cells originated from a single cell. In the conventional sorting method, a lot of effort is required to obtain this proof[3)].

To solve this, we have applied our micromanipulation technology for targeting cells, which was cultivated through our research and development in the biotechnology field up to now, and added a function to prove that single cells were seeded. With this modification, we are able to automatically isolate cells that can then be used for antibody production.

Here, we will introduce the configuration of the NSK-developed equipment and its operating characteristics.

2. Device Configuration

The developed device is shown in Photo 1, with the device configuration shown in Figure 1, and the basic specifications shown in Table 1. The device is equipped with a 3-axis motorized manipulator[4)] and a sample stage. A glass capillary is attached to the manipulator so that precise manipulation can be performed within the well plate. An electric syringe pump is attached to the capillary and is used to collect cells. In addition, two cameras are arranged in the device to enable observation of the capillary.

For control, we have developed dedicated software to control the motors and cameras using a windows PC.

The device performs the steps shown in Figure 2. It automatically collects single cells with a diameter between 13 and 17 µm from the cell suspension in a 6-well plate and seeds them into a 96-well plate. The functions of the device are described below.

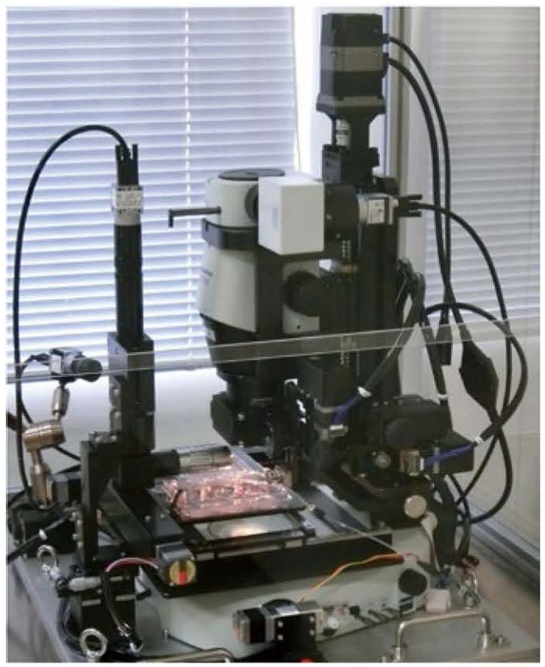

Photo 1 Developed device

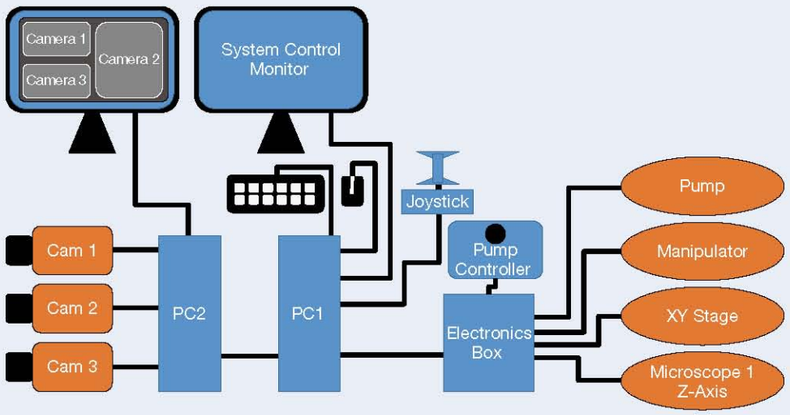

Fig. 1 System components

Table 1 System specifications

	Micro Manipulator	XY Stage	Z-Axis	Pump
Stroke	20 mm	150 mm	100 mm	27.99 µL
Max Speed	5 mm/s	500 mm/s	250 mm/s	–
Resolution	0.1 µm	1.5 µm	1 µm	508 pL
Microscope	Olympus SZX-16			
Camera	USB 3.0 camera x3			
Control	PC			

2.1 Automated cell seeding

Our cell seeding device achieves automatic operation by combining image processing and motion control. The cells to be collected are automatically recognized from the microscope image in the 6-well plate, and the glass capillary is moved to the correct position based on the image processing information, as shown in Photo 2. During cell collection, an optimal drive command is generated and sent to the syringe pump to ensure gentle yet efficient collection of cells. Once the collection operation is completed, the cell is moved to the designated well of the 96-well plate and deposited.

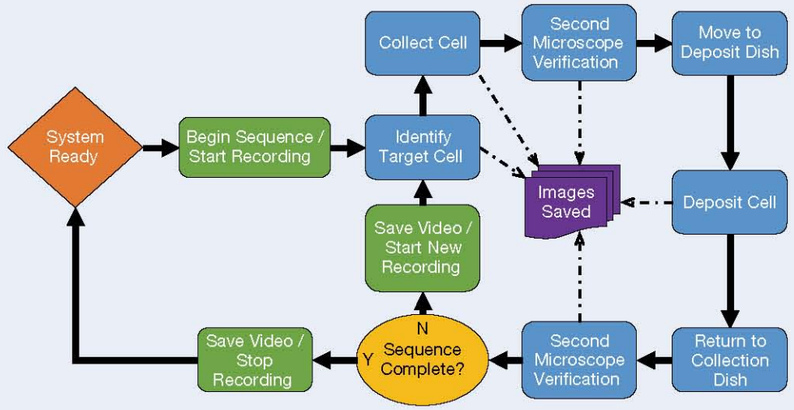

Fig. 2 Sequence operation flowchart

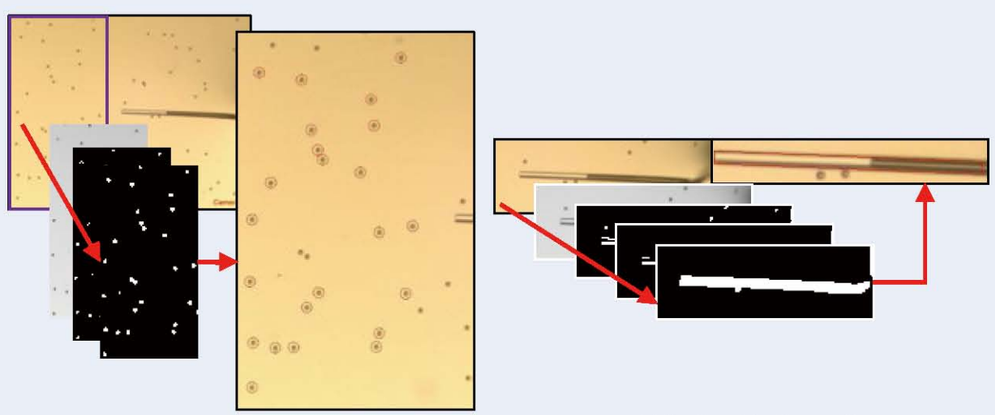

a) Target detection results

b) Capillary detection results

Photo 2 Processing results

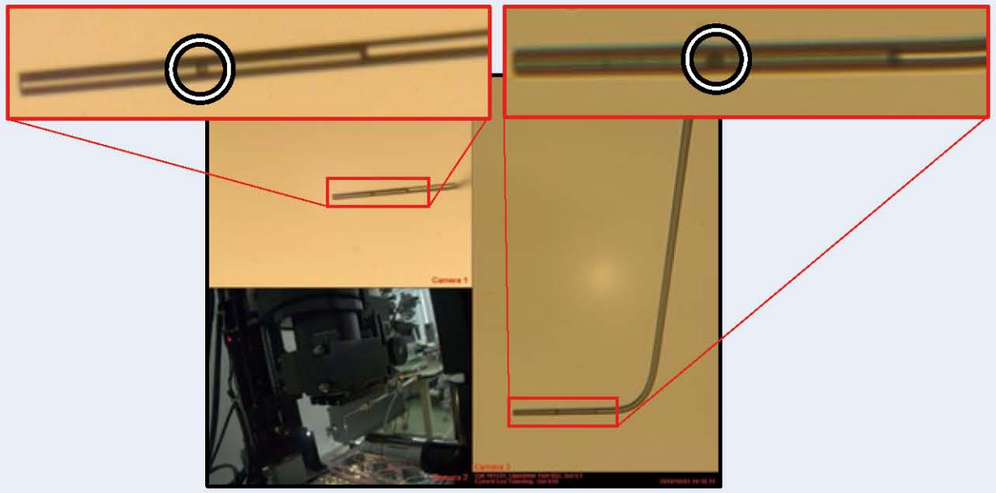

Photo 3 Single-cell verification

2.2 Single-cell verification data

This device is able to generate image data that shows a single cell was successfully seeded in the 96-well plate. At the time of seeding, single cell verification is done by taking multiple images of the capillary, as shown in Photo 3. This ensures there are no blind spots for a second cell to hide in. In addition, a movie of the seeding process is also recorded.

These images and movies are organized and stored on a PC and are referenced to the manipulated cells. When antibody production is analyzed after seeding, and subsequent culturing steps, the images and movie can be used to prove that the producer cells are all derived from a single cell.

2.3 Report function

When performing cell seeding, it is necessary to manipulate a large number of cells. It is difficult for an operator to manage a record that contains images and a video for each manipulated cell.

Therefore, we developed a report function for this device. It displays the recorded images, videos and any user entered data for each seeding operation. This report can be easily exported as a PDF. See Figure 3.

Using this function, the operator can quickly generate a report for each operation without performing any special work. This results in a reduced work load.

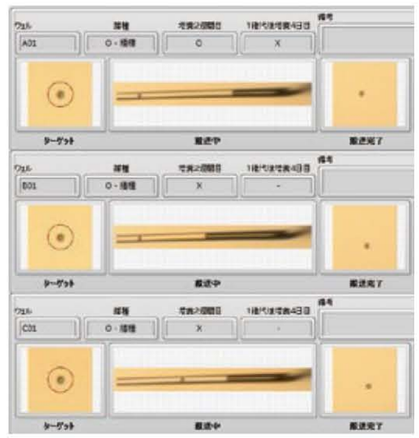

Fig. 3 Example report for a seeding operation

3. Performance Evaluation Results

An experiment was performed where live cells were seeded into a 96-well plate. In this experiment, there was a 94% probability that a single cell was correctly seeded. The working time for seeding into one 96-well plate was 40 minutes. In addition, subsequent testing confirmed that the cells continued to produce antibodies.

4. Conclusion

By developing a unique method that is different from the conventional single cell seeding technique, this device is able to obtain data proving single-cell manipulation at the time of seeding.

We believe that this kind of automation technology, one that combines fine operation with image processing, is an important advancement that will continue to support biotechnology in the future.

5. Acknowledgements

Part of this research was conducted in collaboration with the Manufacturing Technology Association of Biologics (MAB). MAB is supported by the Japan Agency for Medical Research and Development (AMED) and their internal department.

References

1) Feng Li et al., "Cell culture processes for monoclonal antibody production." *mAbs* Vol. 2, 5 (2010): pp. 466–479.
2) Renate Kunert and David Reinhart, "Advances in recombinant antibody manufacturing." *Applied MICROBIOLOGY and BIOTECHNOLOGY* Vol. 100, 8 (2016): pp. 3451–3461.
3) Susan M. Browne and Mohamed Al-Rubeai, "Selection methods for high-producing mammalian cell lines." *Trends in BIOTECHNOLOGY* Vol. 25, 9 (2007): pp. 425–432.
4) Nobuaki Tanaka, "Development of Micro Manipulation System," *NSK TECHNICAL JOURNAL*, 688 (2016) pp. 35–44.

Richard House

Quantitative Evaluation of Effects on Dent-Initiated Flaking of Rolling Bearings (Part 1: Evaluation of Dent Density ρ_d)

Fumiaki Aikawa
Technology Development Division Headquarters Core Technology R&D Center Computational Mechanics Research Group
Sho Hashimoto, Hiroki Komata, Kouji Ueda
Technology Development Division Headquarters Core Technology R&D Center Materials & Rolling Fatigue Life Research Group

Abstract

Dent-initiated flaking is a major failure mode for rolling bearings. An accurate prediction of bearing life is required as bearings are increasingly used in various severe conditions. Bearing life is affected by oil-film thickness and the size and hardness of debris that exists in the lubricant. In this research, we conducted endurance tests under various conditions. Our results found that dent-initiated flaking life is correlated with dent density on the raceway, and dent density is affected by oil-film thickness and the size and hardness of debris in the lubricant.

This article has been approved for reprinting by the Proceedings of JAST Tribology Conference 2017 Fall in Takamatsu.

1. Introduction

Among the flaking that is the main form of damage of rolling bearings, dents form on the raceway surface due to the biting of debris in the lubricating environment and surface-starting-type flaking originating from peeling (small surface cracks) are still problems for bearing users. In recent years, to save energy and improve efficiency, demand for the torque reduction, miniaturization, and weight reduction of rolling bearings has further increased, and the usage environment has become harsher and more diverse, such as lower viscosity lubricating oil and higher contact surface pressure.

Many studies have investigated the effects of debris conditions on life concerning dent-initiated flaking, and the size, hardness, and quantity of debris are generally known as influential factors[1]. Test results on the effect of oil film formation under lubrication contaminated with debris have also been reported[2]. However, the effects of the interaction between the debris condition and oil film formation state on life has not been investigated in detail. The purpose of this study is to conduct bearing life tests under various debris and oil film conditions and to extract and quantify the factors that affect the dent-initiated flaking life in order to accurately predict a bearing life under diversified operating conditions. For this report, we first extracted the changes in the size of debris, quantity of debris, oil film thickness, and density of dents formed on the orbital surface as factors that affect the flaking life of the dent-initiated flaking life.

2. Experimental Method

Figure 1 shows a schematic of the life test rig. The test uses a deep groove ball bearing 6206 (inner diameter 30 mm, outer diameter 62 mm), with the rolling element and a raceway ring made of standard SUJ2 quenching and tempering material as well as a plastic cage. The test rig was designed to apply only the radial load to the test bearing directly.

Table 1 shows the life test conditions. A steel grit, quenched and tempered, and adjusted to an average hardness of 870 HV, is used as debris, and the particle size is selected with a vibrating sieve, as shown in Table 1. Ten types of tests were conducted, in which the size and quantity of debris and lubricating oil properties were changed. The number of tests n was n = 5 to 11, and the life test results were arranged by the Weibull distribution, and the L10 life was obtained from the optimal distribution straight line by the least-squares method. In addition, we observed the central part of the inner ring raceway surface of the bearing after the life test with an optical microscope to measure the number of dents per unit area = dent density ρ_d (count/mm^2).

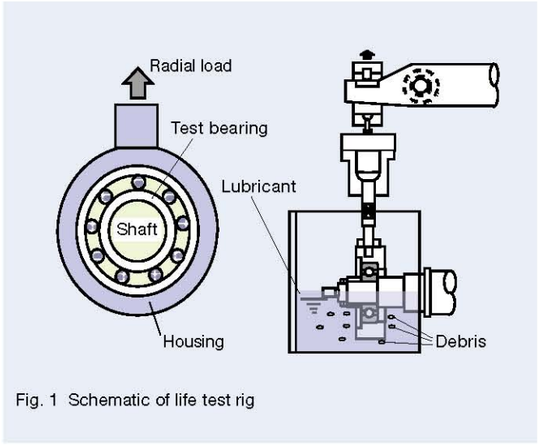

Fig. 1 Schematic of life test rig

Table 1 Operating condition of life tests

Test No.	A-1	A-2	A-3	A-4	A-5	B-1	B-2	B-3	B-4	B-5
Load, kN	6.2									
Rotating speed, min^{-1}	3 000									
Lubrication system	Oil bath									
Hardness of debris, HV	870									
Particle average diameter, μm	170					46				
Quantity of debris, mg/1.2 L	2.5	20	50	20		1.0	5.0	20		
Lubricant	VG68			VG32	VG10	VG68			VG32	VG10

3. Experimental Results and Discussion

Figures 2 shows the relationship between the quantity of debris and the life of L_{10}. Figure 3 shows the relationship between the central oil thickness hc and the life of L_{10}. All the flaking morphologies showed the appearance of dent-initiated flaking. The calculation of the central oil film thickness hc uses Hamrock-Dowson's formula. As for A-5 and B-5, the test was terminated because the flaking did not occur up to 1 000 h, so the plots assumed L_{10} = 1 000 h. As Figure 2 shows, the larger the quantity of debris, the shorter the L_{10} life, and when the quantity of debris is the same, the larger the size of debris, the shorter the L_{10} life. In addition, as Figure 3 shows, the thicker the oil film, the shorter the L_{10} life, and the tendency is more remarkable as the debris is larger. Figure 4 shows an example of surface observation results of the central part of the inner ring raceway surface after the life test. As the oil film thickness increases, the number of dents formed on the raceway surface increases. The increase in the number of dents that are the starting point of flaking is the cause of the shortened life, as shown in Figures 2 and 3. Figures 5 and 6 show the relationship between the quantity of debris and the central oil thickness h_c and ρ_d arranged by debris size. Since the number of debris particles affects the number of dents, not the weight of the debris itself, we calculated the concentration of debris in the lubricating oil from the average particle size and debris weight. As shown in Figure 5, the dent density increased as the quantity of debris increased. The tendency was the same even if the size of the debris changed. In addition, as Figure 6 shows, the dent density also increases as the oil film thickness increases. So far, the number of dents depends on the number of foreign substances in a unit volume and the oil film thickness[2, 3]. Unlike tests described in previous reports, the results of this test suggest that the quantity of debris and number of dents are not in a proportional relationship and that some of the debris contributes to the formation of dents, especially when the quantity of debris is large. Figure 7 shows the relationship between ρ_d and L_{10} life arranged by size of debris. As ρ_d rises, the L_{10} life becomes shorter, and the tendency becomes more pronounced as the debris becomes larger. This is because the dent edge stress concentration is different due to the difference in dent shape. These test results allowed for the extraction of the dent density ρ_d as one of the intermediate factors affecting the L_{10} life. In the future, quantifying ρ_d and estimating the stress acting on the dent edge will allow for a highly accurate prediction of the dent-initiated flaking life.

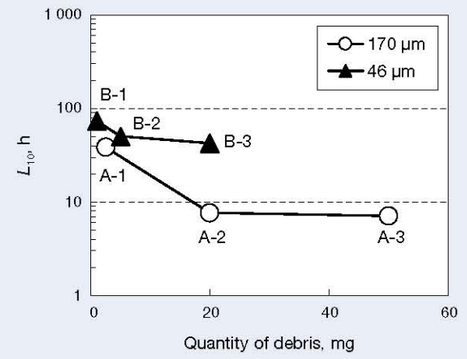

Fig. 2 Relationship between L_{10} and quantity of debris

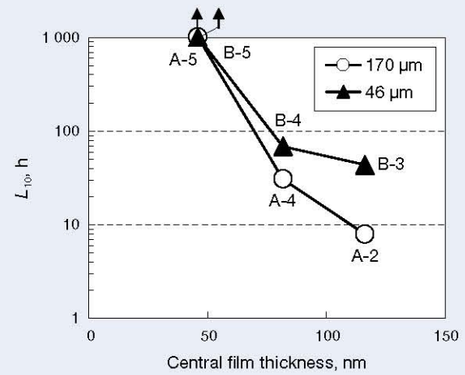

Fig. 3 Relationship between L_{10} and central film thickness

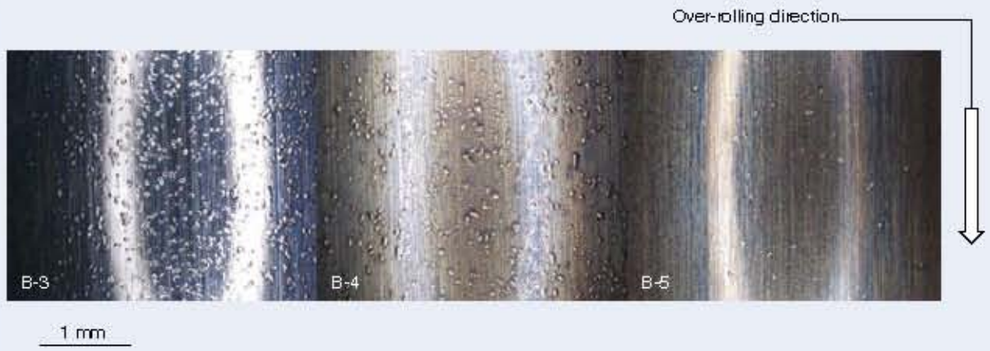

Fig. 4 Surface feature of the inner ring after life tests for different lubricants (B-3 VG68, B-4 VG32, B-5 VG10)

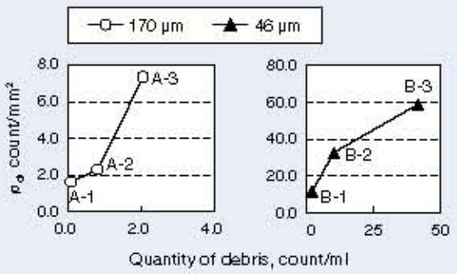

Fig. 5 Relationship between ρ_d and quantity of debris

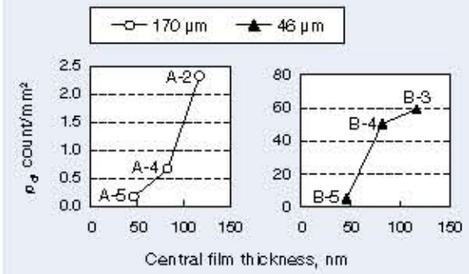

Fig. 6 Relationship between ρ_d and central film thickness

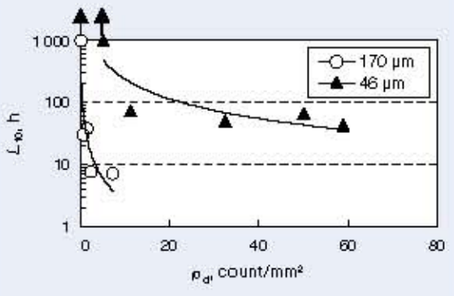

Fig. 7 Relationship between L_{10} and ρ_d

4. Summary

The quantity of the debris, size of the debris, and oil film thickness affect the dent-initiated flaking life of rolling bearings under lubrication contaminated with debris. This report shows that the dent-initiated flaking life correlates with the dent density formed on the orbital surface and that debris conditions and oil film conditions affect the dent density.

References

1) Murakami, H. Takemura, A. Fujii, and K. Furumura, Rolling Contact Fatigue Life under Contaminated Lubrication with Several Foreign Particles (in Japanese), *NSK Technical Journal*, 655 (1993), pp. 17–24.
2) T. Sada and T. Mikami, Effect of Lubricant Film Thickness on Ball Bearing Life under Contaminated Lubrication (Part 2): Relationship between Film Thickness and Dents Formation (in Japanese), *Journal of Japanese Society of Tribologists*, 50 (1), (2005), pp. 62–67.
3) A. Xiaolan, "Effect of debris contamination on the fatigue life of roller bearings," Proceedings of the Institution of Mechanical Engineers, Part J: *Journal of Engineering Tribology*, 215-6 (2001) pp. 563–575.


Akihiko Ishikawa


Sho Hashimoto


Hiroki Komata


Kouji Ueda

Quantitative Evaluation of Effects on Dent-Initiated Flaking on Rolling Bearings

(Part 2: Evaluation of Factors Influencing Dent-Density ρd)

Junichi Hamasaki, Fumiaki Aikawa
CORE TECHNOLOGY R&D CENTER, Technology Research & Development Office 3
Sho Hashimoto, Kouji Ueda
CORE TECHNOLOGY R&D CENTER, Technology Research & Development Office 1

Abstract

Operating environments for rolling bearings are becoming more severe and diversified due to increasing needs for lower energy consumption and higher efficiency. Therefore, dent-initiated flaking on the raceway surface caused by debris in the lubrication environment remains a problem. Previous studies have revealed that the end of bearing life caused by debris has a strong correlation with the number of indentations formed on the orbital raceway surface. In this report, the influence of the size of debris and oil film thickness on dent density is quantified. As a result, a calculation formula was obtained for accurate prediction of dent density from central oil film thickness, the size of debris, and the amount of debris.

This article has been approved for reprinting by the Proceedings of JAST Tribology Conference 2017 Fall in Takamatsu.

1. Introduction

Demand for reduced energy consumption and high efficiency is growing, and the usage environment of rolling bearings is becoming harsher and more diversified due to lower viscosity and increased contact surface pressure. In such an environment, surface-origin-type flaking originating from dents and flaking (small surface cracks) on the orbital surface caused by the biting of debris in the lubricating environment remains a problem.

Therefore, it is becoming more important to improve the accuracy of bearing life prediction. There are many reports on the prediction of dent-initiated flaking life, including on research investigating the effects of debris conditions such as the size, hardness, and quantity of debris on the dent-initiated flaking life[1] as well as the effects on ball-bearing life with lubrication contaminated by debris under oil-film-formation conditions[2]. However, detailed studies have not been conducted on the effects on life due to the interaction between debris and oil film formation. For the first report[3], bearing life tests were conducted under various debris conditions and oil film conditions, and factors affecting the dent-initiated flaking life were extracted and quantified. The investigation illustrated a strong correlation between the dent-density ρ_d (count/mm^2), an intermediate factor, and the dent-initiated flaking life. It is therefore necessary to accurately estimate the dent-density ρ_d for a highly accurate flaking life prediction. We investigated changes in the dent-density ρ_d depending on the size of debris and oil film thickness and attempted to quantify their effects.

2. Experimental Method

Figure 1 shows the schematic of the dent test equipment. A deep groove ball bearing 6206 (inner diameter 30 mm, outer diameter 62 mm) was used as the test bearing. The inner and outer rings and the rolling elements used SUJ2 quenching-tempering material, and the cage material was resin. This test directly applied a radial load to the test bearing.

Table 1 shows the dent test conditions. The quantity of debris was calculated based on the debris particle size and debris weight. A steel grit with hardness adjusted to an average hardness of 870 HV by heat treatment with the size adjusted with a vibrating sieve was used as debris for dent. We conducted 12 types of tests with the size of the debris and the viscosity of lubricating oil as parameters. The operating time of the testing machine was 10 min. The rotation speed was 3 000 rpm. After the dent test, we observed the central part of the bearing's inner ring raceway surface after the life test with a scanning white interference microscope, measuring the number of dents per unit area = dent-density ρ_d (dent density, count/mm^2).

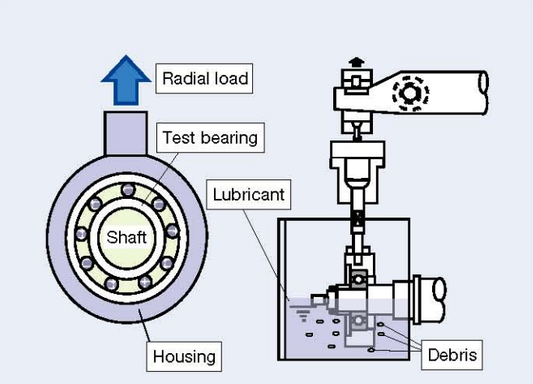

Fig. 1 Schematic of indentation test rig

Table 1 Operating conditions of the indentation tests

Test No.	C-1	C-2	C-3	C-4	D-1	D-2	D-3	D-4	E-1	E-2	E-3	E-4
Load, kN	6.2											
Rotating speed, rpm	3 000											
Lubrication system	Oil bath											
Hardness of debris, HV	870											
Size of debris, m	59				103				181			
Quantity of debris, count/ml	25.6				4.8				0.9			
ISO viscosity grade of lubricant	VG 10	VG 32	VG 68	VG 150	VG 10	VG 32	VG 68	VG 150	VG 10	VG 32	VG 68	VG 150

3. Experimental Results and Discussion

Figure 2 shows the relationship between the lubricating oil viscosity and thickness of the central oil (nm, hereinafter referred to as H_c). The Hamrock-Dowson formula was used to calculate H_c. Afterwards, we organized using H_c. Figure 3 shows the H_c dependence of the dent-density ρ_d. The dent-density ρ_d increases as H_c increases, especially when the debris (size of debris, μm, hereinafter referred to as *size*) is large. Figure 4 shows the *size* dependence of the dent-density ρ_d. From the test results discussed in the first report[3] and the results of this test, we found a relationship between the dent-density ρ_d and quantity of debris (count/ml, hereinafter referred to as Q_d), where $\rho_d \propto \exp(0.0113 \times Q_d)$ and the effect of the quantity of debris Q_d was eliminated by dividing ρ_d by $\exp(0.0113 \times Q_d)$. Figures 3 and 4 show the theoretical line for quantitative analysis, assuming that the dent-density ρ_d depends on H_c, *size*, and Q_d as an exponential function from the above test results. From these results, we formulated the following dent-density calculation formula using the debris *size* (μm), central oil film thickness H_c (nm), and quantity of debris Q_d (count/ml).

$$\rho_d = 1.52 \times (size)^{-1.21} \times H_c^{1.45} \times \exp(0.0113 \times Q_d)$$

Figure 5 shows the results of comparing the dent-density ρ_d obtained in the experiment with the dent-density ρ_d obtained from the dent-density calculation formula using this formula. The correlation coefficient r is 0.97, which means it is possible to perform a highly accurate calculation in which the experimental value and calculated value are almost the same. Therefore, it is possible to obtain a formula that accurately obtains the dent-density ρ_d using the central oil film thickness H_c, *size* of the debris, and quantity of debris Q_d. The indices and coefficients in the formula depend only on these test results and may fluctuate as the number of tests increases in the future.

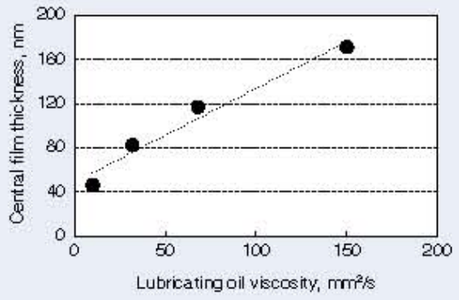

Fig. 2 Relationship between central film thickness and lubricating oil viscosity

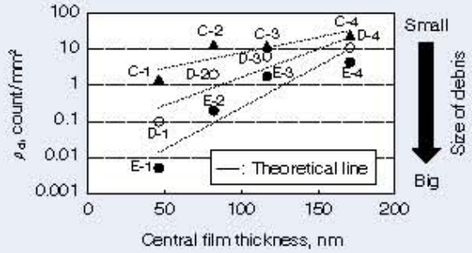

Fig. 3 Relationship between ρ_d and central film thickness H_c

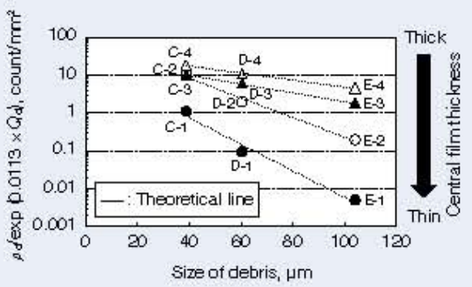

Fig. 4 Relationship between ρ_d/exp (0.0113 ×) and size of debris

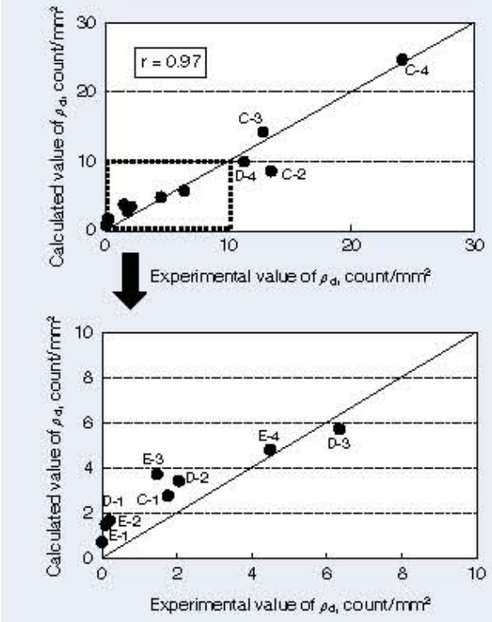

Fig. 5 Comparison between experimental value and calculated value of ρ_d
(Upper: 0–50 count/mm², Lower: 0–10 count/mm²)

4. Summary

It is well known that the dent-initiated flaking life of rolling bearings under lubrication mixed with debris correlates with the dent-density ρ_d. As described in this report, we conducted a dent test using the lubricating oil viscosity and debris *size* as parameters, quantified the relationship between the dent-density ρ_d and each parameter, and formulated the dent-density ρ_d calculation formula.

References

1) Y. Murakami, H. Takemura, A. Fujii, and K. Furumura, "Rolling Contact Fatigue Life under Contaminated Lubrication with Several Foreign Particles" (in Japanese), *NSK Technical Journal*, 655 (1993), pp. 17–24.
2) T. Sada and T. Mikami, "Effect of Lubricant Film Thickness on Ball Bearing Life under Contaminated Lubrication (Part 2): Relationship between Film Thickness and Dents Formation" (in Japanese), *Journal of Japanese Society of Tribologists*, 50 (1), (2005), pp. 62–67.
3) Aikawa Fumiaki, Hashimoto Sho, Komata Hiroki, and Ueda Kouji, Tribology Conference 2017, Autumn Takamatsu


Junichi Hamasaki


Fumiaki Aikawa


Sho Hashimoto


Kouji Ueda

Hub Unit Bearing Sealed by a Plastic Sensor Cap

With more and more automobiles sold globally each year, the use of automobiles is becoming more diversified, including automatic driving, EV conversion, sharing. For this reason, automobiles need to be highly reliable under a wide range of conditions and harsh road surface environments (rough road environments, splashing water, mud, sand, etc.). Moreover, the reduction of CO_2 emissions due to new environmental measures has increased demand for BEVs and HEVs. And to improve automobile performance, ensuring the safety of vehicles requires motion control technology.

Hub unit bearings used in the undercarriage of automobiles are required to maintain their reliability in harsh environments in order to reduce running resistance and detect wheel speed. That is why it is necessary to secure the magnetic encoder output for excellent sealing performance, low friction, and wheel speed detection as a measure against debris intrusion (Figure 1).

The friction of the hub unit bearing comprises the inside of the bearing and seal element, and the contribution is approximately 50% from each. The friction of the seal depends on the seal type and number of seals (Figure 2). Seals are usually applied to the outboard and inboard of the vehicle. For bearings for driving wheels, eliminating the seal inboard the vehicle and sealing it with a sensor cap reduces the friction due to its inner seal (Figure 3).

The sensor cap requires a sealing property against debris intrusion from the wheel speed sensor mounting part and fitting part. The sensor cap also needs to hold the wheel speed sensor so that the wheel speed sensor can stably detect the signal from the magnetic encoder.

NSK developed a hub unit bearing with a sealed plastic sensor cap (Photo 1 and Figure 4) that enables excellent sealing performance, low friction, and stable signal detection of wheel speed sensors in harsh environments.

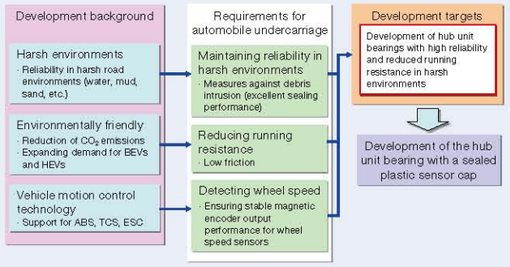

Fig. 1 Development background and target

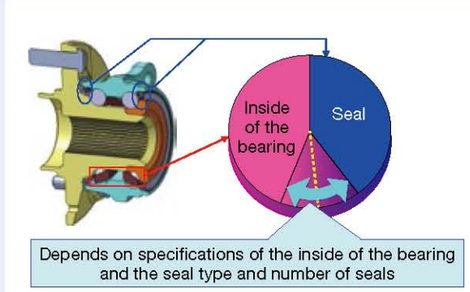

Fig. 2 Friction components for the hub unit bearing

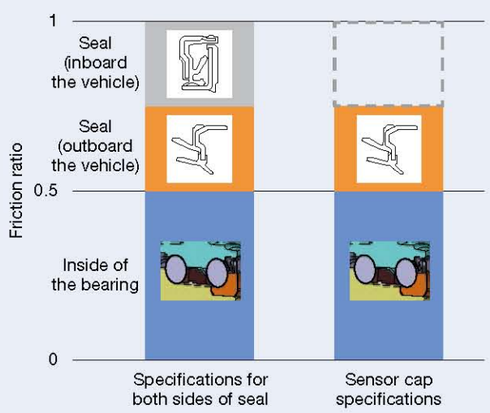

Fig. 3 Friction ratio of the bearing and seal

1. Features

1.1 Friction reduction

Abolishing the seal inboard the car body (Figure 5-A) and changing the structure to a plastic sensor cap (Figure 5-C) can eliminate the seal friction inboard the vehicle body. This design limits the friction to the bearing's inboard and vehicle's outboard seal, reducing the friction for the bearing as a whole (Figure 3).

Photo 1 Hub unit bearing sealed by a plastic sensor cap

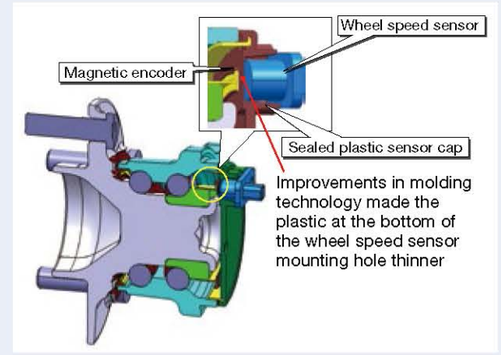

Fig. 4 Structure of the hub unit bearing sealed by plastic sensor cap

	(A) Seal + sensor holder	(B) Plastic cap	(C) New product with a sealed plastic sensor cap
	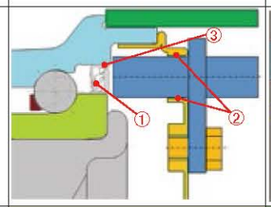	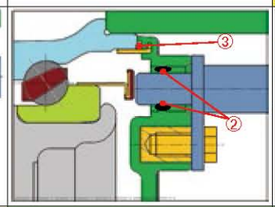	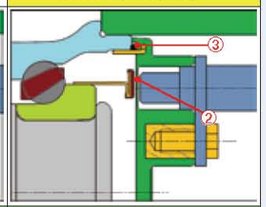
1. Friction	△ Friction of the seal inboard the car body occurs	○	○
2. Wheel speed sensor mounting hole sealability	△ Concerns that debris may enter through the gap between the sensor holder and sensor	△ Concerns that debris may enter from the O-ring due to assembly when replacing the sensor	○ Sealed with a thin plastic plate
3. Sealing property of the fitting part	○ Sealed with a rubber seal	○ Sealed with an O-ring	○ Sealed with an O-ring

Fig. 5 Structure and characteristic of the seal and cap

1.2 Improved sealing

In the conventional plastic cap structure (Figure 5-B), the wheel speed sensor is provided with an O-ring to ensure the sensor mounting hole seal. However, since the sensor mounting hole penetrates when assembling the wheel speed sensor, there are concerns that the O-ring position may shift, and debris may infiltrate into the bearing from the O-ring.

Sealing the bottom of the wheel speed sensor mounting hole with a thin plastic plate can improve this product's sealing performance against debris intrusion from the sensor mounting hole (Figure 5-C).

1.3 Thinning of plastic

Improving the plastic molding technology can make the bottom surface of the wheel speed sensor mounting hole thinner.

Shortening the distance between the magnetic encoder and wheel speed sensor can stabilize the wheel speed sensor signal detection from the magnetic encoder (Figure 4).

2. Summary

The hub unit bearing with a sealed plastic sensor cap can achieve excellent sealing performance, low friction, and stable signal detection of the wheel speed sensor and contribute to the improvement of vehicle reliability and fuel efficiency. In the future, we will aim to develop products that can meet the needs for further fuel efficiency improvements while maintaining high reliability for use in more vehicles.

Ball Screw Units for Electric Hydraulic Brake Systems

While enhancing the sophistication of automatic braking functions associated with each country's efforts to enforce collision damage mitigation brakes, one advanced driver assistance system, and electrification of powertrains are accelerating, the electrification of brake boosters is also progressing.

A vacuum booster, which was mainstream for gasoline-powered vehicles, assists the driver's pedaling force with the engine's negative pressure. In contrast, the electro-hydraulic brake booster uses an actuator that combines a motor and a pressure generating mechanism to provide a mechanism to assist with pedal force. The linear motion mechanism used in the electro-hydraulic brake booster is required to convert the motor's rotational motion into linear motion and control the brake fluid pressure at a high speed and with precision. A structure that combines a ball screw and motor, which are excellent in responsiveness, efficiency, and positioning precision, is promising. Its structure is such that the torque of the motor is converted into thrust with a ball screw to generate the hydraulic pressure required for the brake (Figure 1).

NSK integrates the ball screw and its peripheral parts to reduce the unit size and weight and increase the degree of freedom in the layout. This article introduces this technology.

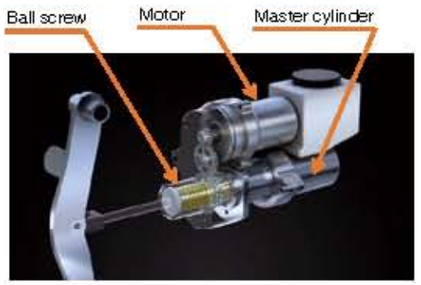

Fig. 1 Structure of the ball-screw-type electric hydraulic brake booster

1. Configuration, Structure, and Specifications

Figure 2 shows the structure of the developed ball screw. A ball screw comprises of a screw shaft and nut forming a spiral groove as well as a ball that rolls between them and circulation parts for circulating the ball in the nut. Furthermore, when used with nut rotation, power transmission parts such as bearings on the nut's outer periphery and gears that input power to the nut, are in place.

This product integrates a nut with a bearing inner ring and circulation parts.

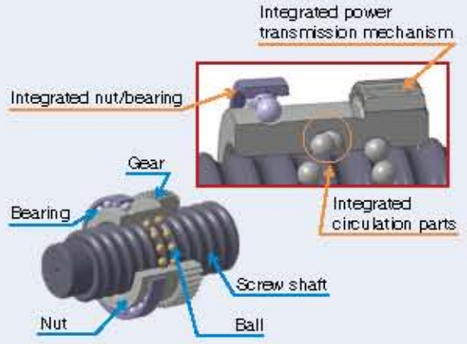

Fig. 2 Developed ball screw configuration

2. Features

(1) Bearing integration

Use with nut rotation usually requires a support bearing as a separate part. However, integrating the bearing inner ring and nut can reduce the outer diameter of the bearing (Figure 3).

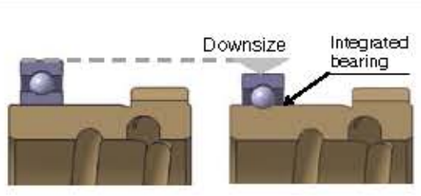

Fig. 3 Downsizing from integrated bearings

(2) Integrating circulation parts

Suppose the nut circulation parts of the ball screw are conventional independent bodies. In this case, the circulation parts interfere with the adjacent raceway grooves, so it is necessary to leave a certain distance between the ball circulation circuits. In addition, offsetting in the axial direction is necessary between the components, such as the gears and circulation parts. Therefore, integrating the nut and the circulation parts using cold forging technology can shorten the raceway groove's length, overlap the circulation parts and the gear in the axial direction to eliminate mounting restriction, and enable axial miniaturization (Figure 4).

3. Applications

It is applied to ball-screw-type electro-hydraulic brake boosters. We have started mass production of products that use this technology, integrating the circulation parts and bearing (Photo 1).

4. Summary

The integrating technology of the ball screw and its peripheral parts can contribute to the miniaturization and weight reduction of the electro-hydraulic brake booster.

NSK will improve vehicle safety by developing and launching small, high-performance ball screws for the market.

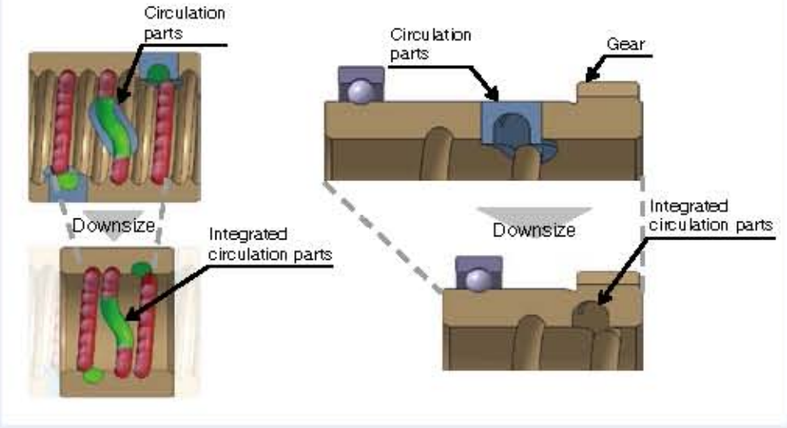

Fig. 4 Downsize by integrating the circulation parts

Photo 1 Ball screw for the electric hydraulic brake booster in mass production

High Safety Redundant Column EPS

In recent years, automobiles have become more sophisticated, requiring EPS to support the driving support function of Advanced Driver-Assistance Systems (ADAS). Since EPS is an important safety component, it has always been highly safe. However, the issuance of the functional safety standard ISO 26262, which applies to ADAS, required an even higher level of safety and quantification of the failure rate. The main characteristic of EPS is the avoidance of an assist-stop state at the time of failure. In the past, EPS was intentionally put into an assist-stop state by the Fail Safe when the main functions such as the sensor and drive system failed. However, considering the above-mentioned ADAS operation, it now treats a sudden assist-stop as a danger to avoid.

In this system, the torque sensor, angle sensor, and motor drive unit, which are the main functions of EPS, are made redundant to avoid an assist-stop as much as possible in the event of a failure. As a result, the assist-stop probability at the time of failure could be reduced to one-fifth or less compared to the non-redundant system. This system is explained below.

1. Configuration, Structure, and Specifications

Figure 1-1 shows a complete view of the redundant system, and Figure 1-2 shows the redundant system's specific functional blocks.

2. Features

2.1 Redundant system

2.1.1 Redundant configuration of the torque sensor

A redundant design with two sensors avoids an assist-stop when the torque sensor fails (Figure 2-1-1). Two linear Hall ICs detect the magnetic signal corresponding to the input torque. One IC system has two detection elements, outputting each detection value T-1 and T-2 to the ECU as a SENT signal. The ECU compares T-1 and T-2, recognizes T-1 and T-2 as torque if normal, and switches to the T-3 and T-4 of different systems if abnormal. This function maintains the torque detection function even when the torque sensor is in an abnormal state.

2.1.2 Redundant configuration of the angle sensor

A redundant design with three sensors avoids an assist-stop when the motor angle sensor fails (Figure 2-1-2). Three TMR sensors detect the magnetic flux direction of the magnet, provided on the motor shaft, as the motor angle. Each sensor decomposes the magnetic flux direction into Sin and Cos components and sends them to the ECU as analog values. The ECU demodulates the motor angle θ from the Sin and Cos signals. A comparison of θ_1, θ_2, and θ_3 of each system enables setting θ_1 as the motor angle when normal and switch to θ_2 when θ_1 is abnormal. This function maintains the angle detection function even when the angle sensor is abnormal.

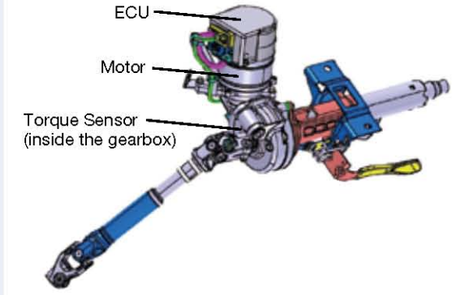

Fig. 1-1 Highly safe redundant column EPS

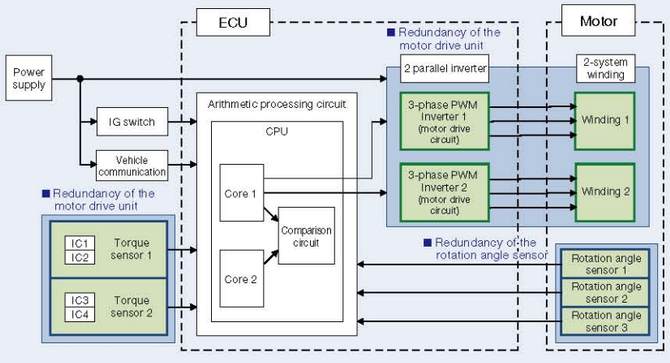

Fig. 1-2 Block diagram of the redundant system

2.1.3 Redundant configuration of the motor drive unit

Setting two-motor drive units (3-phase PWM inverter, Gate Driver Unit (GDU), motor coil) avoids an assist-stop when the motor drive system fails (Figure 2-1-3). Normally, two systems drive in parallel, and in the event of an abnormality the abnormal system stops and the remaining system continues to drive. This function maintains the assist function even when the motor drive system is abnormal.

2.2 Functional safety support

EPS is required in order to comply with ISO 26262. According to the standard, serious failures such as self-steering are Automotive Safety Integrity Level D (ASIL D). The allowable failure rate is 10 FIT (failure in time = unit of failure rate) or less. For the failure rate calculation, we used IEC62380, etc. The problematic sudden assist-stop was ASIL B, and the failure rate target was 100 FIT or less.

100 FIT was the target because it is difficult to achieve 100 FIT in reality since an assist-stop is also a safe state when ASIL D occurs. However, the failure rate of conventional non-redundant systems was 1386 FIT, significantly exceeding the target, which significantly increased demand to reduce the failure rate.

This system has an ASIL D failure rate of 4.13 FIT and thus addresses that demand. The failure rate of ASIL B (assist-stop) has also been reduced to 268 FIT, which has not reached the 100 FIT target, but the failure rate was reduced to one-fifth or less compared to the non-redundant system. The product therefore represents a significant safety improvement.

3. Applications

The product is an ISO 26262-compliant electric power steering system for vehicles with an ADAS function.

4. Summary

To comply with ISO 26262 for vehicles equipped with ADAS, we commercialized a system in which the EPS primary function has been made redundant. The assist-stop occurrence rate is reduced to 268 FIT, which is one-fifth that of the non-redundant system. In the future, if 100 FIT is not the target but rather a requirement for autonomous driving and the like, then a system with redundant microcomputers and power supply units will be required.

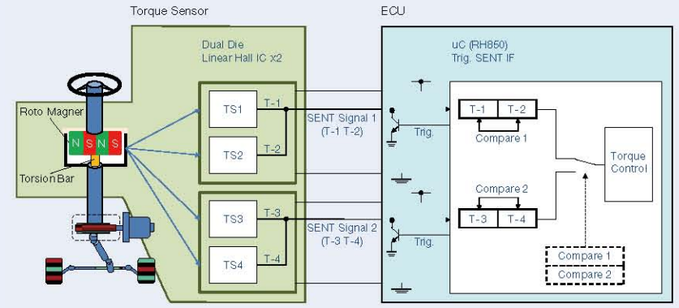

Fig. 2-1-1 Redundant torque sensor system

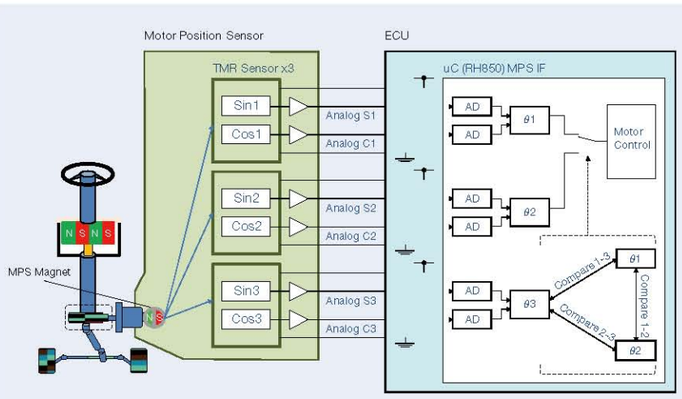

Fig. 2-1-2 Redundant motor position sensor system

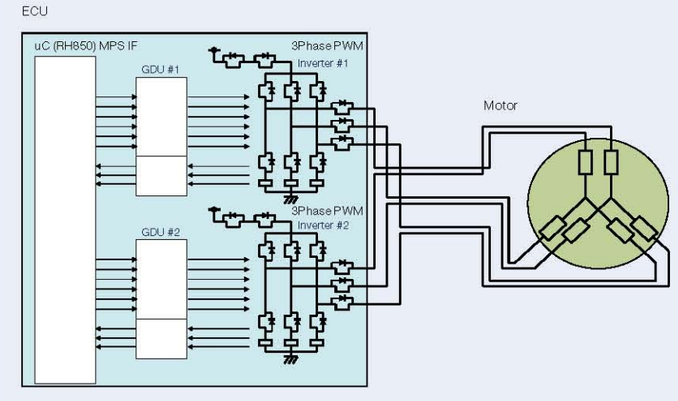

Fig. 2-1-3 Redundant motor drive system

Thin-Section Ball Bearings for Strain Wave Gearings

In recent years, as the working population declines due to lower birthrates and an aging population globally, the advanced utilization of all kinds of information such as big data and AI is progressing. Along with this, the spread of robots is rapidly increasing at various worksites. The application of these robots is expanding from tasks that are difficult for humans to perform, such as transporting heavy objects and working in dangerous places, to those performed on behalf of humans, such as transporting and assembling lightweight objects. Therefore, there is a need for small-scale robots that can deal with objects that humans can carry.

For this reason, the required functions of the motor and reducer built into the robot will change, and demand for strain wave gearings that can be lightweight, compact, and achieve a high reduction ratio will increase.

The bearings used in this strain wave gearing operate with elliptical deformation and are significantly different in terms of conventional bearing specifications.

Photo 1 Thin-section ball bearing for strain wave gearings

1. Configuration, Structure, and Specifications

What follows is a brief description of the strain wave gearing (Figure 1). First, the external gear (having external teeth) bent into an ellipse engages with an internal gear (having internal teeth) that is a perfect circle. By rotating this ellipse phase, it is a unique mechanism that decelerates according to the difference in the number of teeth of both gears (Figure 2). An elliptical shaft and a bearing are required to give the external gear elliptical deformation and phase rotation (Figure 3). By fitting the elliptical shaft to the inner ring and giving rotation to the shaft, the outer ring can transmit the phase rotation of the elliptical deformation (phase change of the ellipse) to the external gear via the ball. The function of this product is to convey this elliptical shape correctly.

This product has extremely thin outer and inner rings (Figure 4) compared to general deep groove ball bearings, which allows for its functions. In the reducer, the bearings always operate with deformation, so applying the optimum design avoids fracturing due to bending deformation in addition to conventional rolling fatigue.

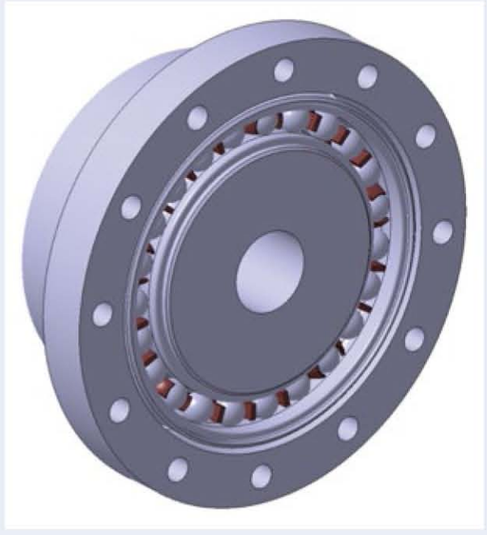

Fig. 1 Strain wave gearing

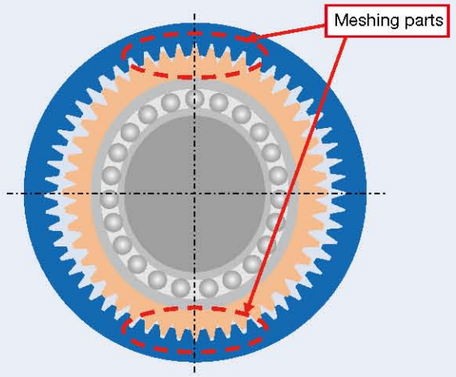

Fig. 2 Condition of gear contact

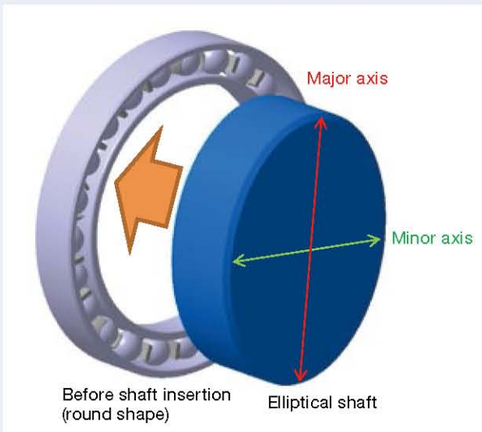

Fig. 3 Insertion of an elliptical shaft into the developed bearing

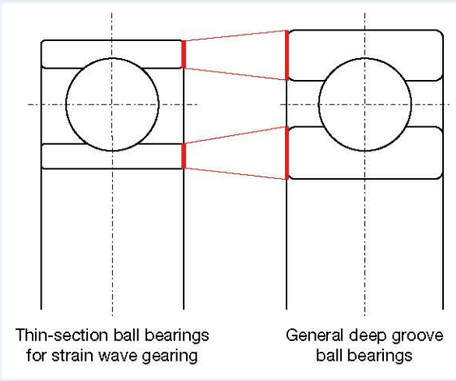

Fig. 4 Comparison with general deep groove ball bearings with the same ball diameter

2. Features

(1) NSK's material/heat treatment technology and analysis techniques provide a highly reliable design that prevents the outer and inner rings from cracking even when used with deformation.

(2) In the reducer, it is necessary to correctly convey the shaft's elliptical shape to the external gear via the inner ring, ball, and outer ring. Hence, it is essential for the outer and inner rings to have the proper wall thickness.

NSK manufacturing technology, which processes thin outer and inner rings with high precision, has made commercialization of the product possible.

3. Applications

Its primary application is a wave generator for strain wave gearing, but it can also be used on the premise of deformation. For example, it is possible to replace the parts used in the conventional sliding contact, such as the cam mechanism with this bearing.

4. Summary

Thin-section ball bearings for strain wave gearing are significantly different from conventional bearings that support the shaft and rotate smoothly and are used on the condition of deformation and have a new function of transmitting the shape correctly. The product's design is optimized to satisfy these functions and contribute to high accuracy of strain wave gearing and robots.

In addition, by applying the function of transmitting the shape, we will consider replacing the parts that were conventionally in sliding contact and aim to contribute to the environment by extending the life and efficiency of mechanical products.

Sealed-Clean Four-Row Tapered Roller Bearing with Long-Life, Water-Resistant Grease

Steel manufacturers have been working on reducing carbon dioxide emissions and environmental impacts through energy saving and other measures. Simultaneously, we have been developing high value-added steel products, improving productivity through stable equipment operations, and reducing maintenance costs. Iron-making equipment always requires highly reliable and long-life bearings with reduced premature damage.

As outlined in Figure 1, the iron-making process comprises the pig iron-making process (equipment that melts raw materials to make molten steel), steel-making process (equipment that adjusts the composition of molten steel and hardens it), and rolling process (equipment that forms the hardened steel to a rolling roll and then into the shape of plates or bars).

Among these, the bearings for the rolling mill used in the rolling process are among the equipment used in harsh environments.

For the work roll (WR) bearings of the rolling mill (Figure 2), the four-row tapered roller bearings are mainly used with grease lubrication. In addition to severe usage conditions such as load and speed, the environment is harsh where oxide scale and cooling water (or rolling water) infiltrate into the bearing. The bearing is affected by considerable early damage due to the flaking or rusting of the raceway surface caused by poor lubrication. Reducing lubricant consumption is also an issue. As a countermeasure, we have been developing products that utilize the sealing design technology optimal for rolling mill bearings and grease technology that minimizes the effects of water intrusion. We developed a long-life, water-resistant grease-sealed four-row tapered roller bearing, described as follows.

1. Configuration, Structure, and Specifications

Photo 1 shows the newly developed bearing, and Figure 3 shows its cross-sectional structure. The oil seal is compact, and a new processing method for the cage was used to extend the roller length and increase the number of rollers, resulting in a high load capacity design. The inside of the bearing is sealed with the newly developed water-resistant grease to minimize the effects of water intrusion (Photo 2).

Table 1 shows the main specifications of the developed bearing.

2. Features

1. Maximized load capacity and cleaned sealing

(1) Optimizing the internal design of the sealed-clean four-row tapered roller bearing increased the basic dynamic load rating by about 25% compared to the conventional product.

(2) The tight sealing suppresses the ingress of foreign matter and water to extend the service life and reduces the amount of grease used in cleaning and maintaining the onsite work environment.

2. Improved Lubrication Performance (Development of Water-Resistant Grease)

(1) Optimizing the grease composition enables forming and maintaining a thick oil film between the bearing raceway surface and rollers to prevent metal contact between the raceway surface and rollers.

(2) Forming a protective film on the raceway surface by blending a special additive prevents water from contacting the raceway surface and also prevents rusting. Figure 4 shows the characteristics of the developed grease. As a result of the service life test in a water-infiltrated environment, it was confirmed that the developed grease has a service life that is more than twice as long as that of the conventional grease (Figure 5).

3. Applications

The developed product is suitable for all work roll bearings for steel-making equipment and hot/cold rolling mills.

4. Summary

Our tests confirmed that the newly developed bearing prevents premature damage even in a cold rolling mill WR bearing. We will continue to meet the needs of steel-makers, promote the development of more environmentally friendly bearings, and develop products that contribute to the advancement of the steel industry.

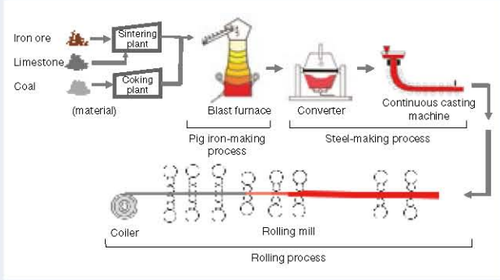

Fig. 1 Steel-making process

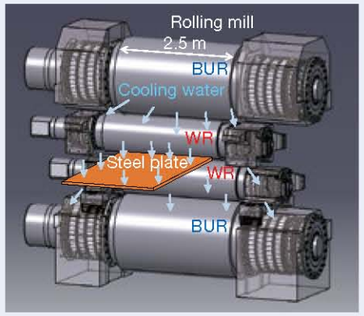

BUR: Backup roll WR: Work roll

Fig. 2 Rolling mill structure (4 Hi-Mill)

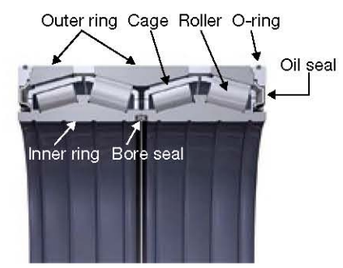

Fig. 3 Cross section of the developed bearing

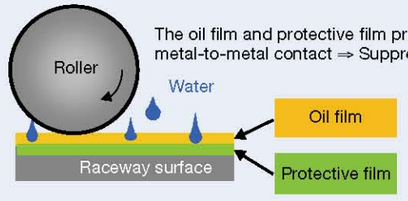

Fig. 4 Characteristics of the developed grease

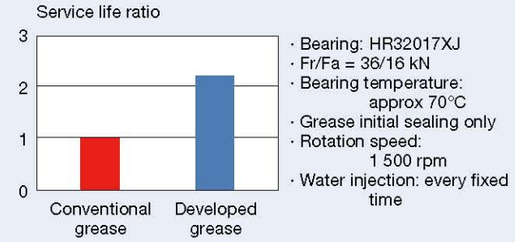

Fig. 5 Bearing life test under water entry

Photo 1 Sealed-clean four-row tapered roller bearing with long-life, water-resistant grease

Photo 2 Inside conditions of the bearing with developed grease

Table 1 Specifications

Bearing number	Main dimensions, mm				Basic dynamic load rating
	Inner diameter	Outer diameter	Inner ring width	Outer ring width	Cr (kN)
245KVS3402 ( ) RN1	245	345	310	310	2 700
279KVS3952 ( ) RN1	279.4	393.7	320	320	2 720
317KVS4251 ( ) RN1	317.5	422.275	269.875	269.875	2 740
343KVS4551 ( ) RN1	343.052	457.098	254	254	2 430
482KVS6151 ( ) RN1	482.6	615.95	330.2	330.2	4 900

( ): Represents a special symbol

High Durability Precision Ball Screw

The ball screw is used as a precision feed drive mechanism element of a machine and is an important part for the production of high-precision, high-quality products.

In recent years, the feed drive mechanism must maintain accuracy for an extended period and further extend its maintenance interval.

To address this, NSK has developed a high durability precision ball screw (Photo 1) that uses surface modification technology for the ball screw rolling surface to maintain a high level of precision for an extended period, described as follows.

Photo 1 High durability precision ball screw

1. Configuration, Structure, and Specifications

The high durability precision ball screw is made by applying NSK's original surface modification technology to the rolling surface of the screw shaft and nut. Photo 2 shows numerous tiny dimples formed on the rolling surface.

These play the role of improving the oil film-forming ability between the steel ball and rolling surface and also suppress wear due to contact between metals.

2. Features

(1) Improved wear resistance

The developed product suppresses wear due to contact between metals by improving the oil film-forming ability.

It is particularly effective under conditions such as low speeds and small stroke operations where an oil film is difficult to form.

As a result, this has made it possible to suppress the decrease in preload and maintain the accuracy of the ball screw for an extended period.

NSK has performed tests under severe conditions such as ultra-low speeds and minute stroke. Figures 1 and 2 show the test data comparing the torque characteristics and wear characteristics.

Photo 2 Surface properties

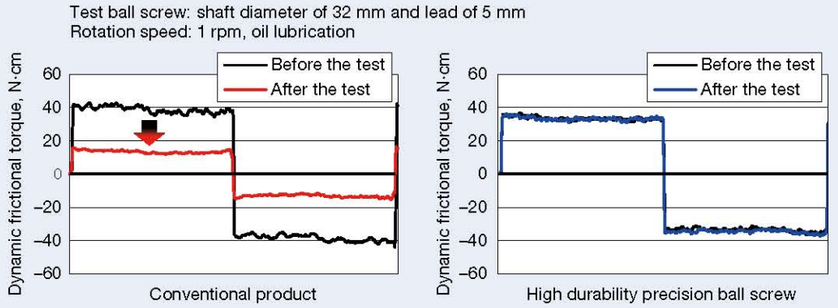

Fig. 1 Preload torque before and after the low speed test

(2) Extended machine maintenance period

Maintaining the precision life of the ball screw for an extended period allows for stable operation of the machine for a long period and extends the machine maintenance interval.

(3) Contribution to reduced machine energy consumption

Improving the oil film-forming ability allowed the product to reduce the dynamic frictional torque by up to 40% compared to the conventional product, especially at 0.1 to 10 rpm. As a result, reducing the energy consumption of the machine is possible (Figure 3).

In addition, suppressing the torque increase at low speeds facilitates controlling the drive of the ball screw, with the expectation that the developed product improves the accuracy during curved surface machining and reversal.

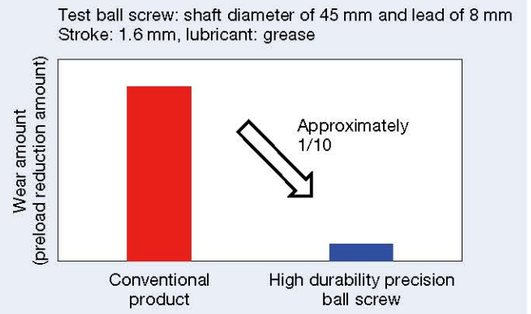

Fig. 2 Results of the small stroke wear test

3. Applications

The product is suitable for machines with severe positioning accuracy requirements, such as die machining centers, electric discharge machines, lathes, and grinding machines.

4. Summary

The high durability precision ball screw is environmentally friendly because it can improve machine tool productivity, extend the maintenance interval, and reduce energy consumption by maintaining precision for an extended period.

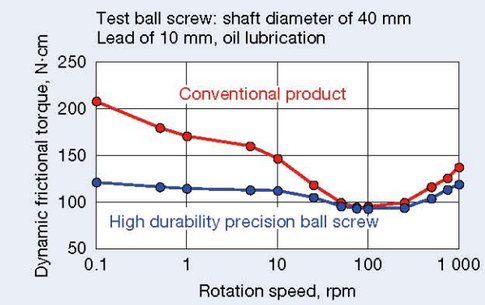

Fig. 3 Relationship between the dynamic frictional torque and rotation speed

Worldwide Sales Offices

P: Phone F: Fax ☆: Head Office

NSK LTD.-HEADQUARTERS, TOKYO, JAPAN

Nissei Bldg., 1-6-3 Ohsaki, Shinagawa-ku, Tokyo 141-8560, Japan

INDUSTRIAL MACHINERY BUSINESS DIVISION-HEADQUARTERS
P: +81-3-3779-7227 F: +81-3-3779-7432

AUTOMOTIVE BUSINESS DIVISION-HEADQUARTERS
P: +81-3-3779-7189 F: +81-3-3779-7917

●Africa

South Africa:

NSK SOUTH AFRICA (PTY) LTD.

SANDTON 25 Galaxy Avenue, Linbro Business Park, Sandton 2146, South Africa
P: +27-011-458-3600 F: +27-011-458-3608

●Asia and Oceania

Australia:

NSK AUSTRALIA PTY. LTD.

MELBOURNE ☆ 100 Logis Boulevard, Dandenong South, Victoria, 3175, Australia
P: +61-3-9765-4400 F: +61-3-9765-4466

SYDNEY Suite A315, 20 Lexington Drive, Bella Vista, New South Wales, 2153, Australia
P: +61-2-9839-2300 F: +61-2-8824-5794

BRISBANE 1/68 Selhurst Street, Coopers Plains, Queensland 4108, Australia
P: +61-7-3347-2600 F: +61-7-3345-5376

PERTH Unit 1, 71 Tacoma Circuit, Canning Vale, Western Australia 6155, Australia
P: +61-8-9256-5000 F: +61-8-9256-1044

New Zealand:

NSK NEW ZEALAND LTD.

AUCKLAND Unit F, 70 Business Parade South, Highbrook, Business Park Auckland 2013, New Zealand
P: +64-9-276-4992 F: +64-9-276-4082

China:

NSK (SHANGHAI) TRADING CO., LTD.

JIANGSU No.8 NSK Rd., Huaqiao Economic Development Zone, Kunshan, Jiangsu, China (215332)
P: +86-512-5796-3000 F: +86-512-5796-3300

NSK (CHINA) INVESTMENT CO., LTD.

JIANGSU ☆ No.8 NSK Rd., Huaqiao Economic Development Zone, Kunshan, Jiangsu, China (215332)
P: +86-512-5796-3000 F: +86-512-5796-3300

BEIJING Room 1906, Beijing Fortune Bldg., No.5 Dong San Huan Bei Lu, Chao Yang District, Beijing, China (100004)
P: +86-10-6590-8161 F: +86-10-6590-8168

TIAN JIN Unit 4604, 46/F., Metropolitan Tower, 183 Nanjing Road, Heping District, Tianjin, China (300051)
P: +86-22-8319-5030 F: +86-22-8319-5033

CHANGCHUN Room 902-03, Changchun Hongwell International Plaza, No.3299 Renmin Street, Changchun, Jilin, China (130061)
P: +86-431-8898-8882 F: +86-431-8898-8670

SHENYANG Room 1101, China Resources Building, No. 286 Qingnian Street, Heping District, Shenyang Liaoning, China (110004)
P: +86-24-2334-2868 F: +86-24-2334-2058

DALIAN Room 1805 Xiwang Tower, No.136 Zhongshan Road, Zhongshan District, Dalian, Liaoning, China (116001)
P: +86-411-8800-8168 F: +86-411-8800-8160

NANJING Room A1 22F, Golden Eagle International Plaza, No.89 Hanzhong Road, Nanjing, Jiangsu, China (210029)
P: +86-25-8472-6671 F: +86-25-8472-6687

FUZHOU Room 1801-1811, B1#1A Class Office Building, Wanda Plaza, No.8 Aojiang Road, Fuzhou, China (350009)
P: +86-591-8380-1030 F: +86-591-8380-1225

WUHAN Room 1512, No.196Yuncai Road, Office Building, Oceanwide City Square, JiangHan, District, WuHan, China (400039)
P: +86-27-8556-9630 F: +86-27-8556-9615

QINGDAO Room 802, Fargiory International Plaza, No.26 Xianggang Zhong Road, Shinan District, Qingdao, Shandong, China (266071)
P: +86-532-5568-3877 F: +86-532-5568-3876

GUANGZHOU Room 1011-16, Yuexiu Financial Tower, No.28 Zhujiang Road East, Zhujiang New Town, Guangzhou, Guangdong, China (510627)
P: +86-20-3817-7800 F: +86-20-3786-4501

CHANGSHA Room 3209, Huayuan International Center, No.36, Section 2, Xiangjiang Middle Road, Tianxin District, Changsha, Hunan, China (410002)
P: +86-731-8571-3100 F: +86-731-8571-3255

LUOYANG Room 955, HUA-YANG PLAZA HOTEL, NO.88 Kaixuan W.Rd., Jian Xi District, Luoyang,Henan Province, China (471003)
P: +86-379-6069-6188 F: +86-379-6069-6180

XI'AN Room 1007, B Changan Metropolis Center, No.88 Nanguanzheng Steet, Xi'an, Shanxi, China (710068)
P: +86-29-8765-1896 F: +86-29-8765-1895

CHONGQING Room 612, Commercial Apartment, Athastel Hotel, No.288, Keyuan Rd.4, Jiulongpo District, Chongqing, China (400039)
P: +86-23-6806-5310 F: +86-23-6806-5292

CHENGDU Room1117, Lippo Tower, No.62 North Kehua Road, Chengdu, Sichuan, China (610041)
P: +86-28-8528-3680 F: +86-28-8528-3690

NSK CHINA SALES CO., LTD.

JIANGSU No.8 NSK Rd., Huaqiao Economic Development Zone, Kunshan, Jiangsu, China (215332)
P: +86-512-5796-3000 F: +86-512-5796-3300

NSK HONG KONG LTD.

HONG KONG ☆ Suite 705, 7th Floor, South Tower, World Finance Centre, Harbour City, T.S.T, Kowloon, Hong Kong, China
P: +852-2739-9933 F: +852-2739-9323

SHENZHEN Room 624-626, 6/F, Kerry Center, Renminnan Road, Shenzhen, Guangdong, China
P: +86-755-25904886 F: +86-755-25904883

Taiwan:

TAIWAN NSK PRECISION CO., LTD.

TAIPEI ☆ 10F-A6, No.168, Sec.3, Nanjing East Rd., Zhongshan Dist., Taipei City 104, Taiwan
P: +886-2-2772-3355 F: +886-2-2772-3300

TAICHUNG 3F. -2, No. 540, Sec. 3, Taiwan Blvd., Xitun Dist., Taichung City 407, Taiwan
P: +886-4-2708-3383 F: +886-4-2708-3385

TAINAN Rm. A1, 9F., No.189, Sec. 1, Yongfu Rd., West Central Dist., Tainan City 700, Taiwan
P: +886-6-215-6058 F: +886-6-215-5518

India:

NSK BEARINGS INDIA PRIVATE LTD.

CHENNAI ☆ TVH Beliciaa Towers, 2nd Floor, Block I, No.71/1, MRC Nagar Main Road, MRC Nagar, Chennai-600 028,India
P: +91-44-2847-9600 F: +91-44-2847-9601

MUMBAI No.321, A Wing, Ahura Centre, 82, Mahakali Caves Road, Andheri (E), Mumbai-400 093, India
P: +91-22-2838-7787

JAMSHEDPUR 13/A, 2nd Floor, Circuit House Area, North West Layout, Road No.12, (Near Sai Baba Mandir), Sonari, Jamshedpur-831 011, Jharkhand, India
P: +91-657-2421144

GURGAON Unit No. 202, 2nd Floor, 'A' Block, Iris Tech Park, Sector – 48 (Sohna Road), Gurgaon–122018, Haryana, India
P: +91-124-4838000

Indonesia:

PT. NSK INDONESIA

JAKARTA Summitmas II, 6th Floor, Jl. Jend Sudirman Kav. 61-62, Jakarta 12190, Indonesia
P: +62-21-252-3458 F: +62-21-252-3223

Korea:

NSK KOREA CO., LTD.

SEOUL Posco Center (West Wing) 9F, 440, Teheran-ro, Gangnam-gu, Seoul, 06194, Korea
P: +82-2-3287-0300 F: +82-2-3287-0345

Malaysia:

NSK BEARINGS (MALAYSIA) SDN. BHD.

SHAH ALAM ☆ No. 2, Jalan Pemaju, U1/15, Seksyen U1, Hicom Glenmarie Industrial Park, 40150 Shah Alam, Selangor, Malaysia
P: +60-3-7803-8659 F: +60-3-7806-5982

PRAI No.24, Jalan kilik, Taman Inderawasih, 13600 Prai, Penang, Malaysia
P: +60-4-3902275 F: +60-4-3991830

JOHOR BAHRU 88 Jalan Ros Merah 2/17, Taman Johor Jaya, 81100 Johor Bahru, Johor, Malaysia
P: +60-7-3546290 F: +60-7-3546291

IPOH No.10&10A, Jalan Industri Paloh, Kawasan Perindustrian Ringan Paloh, 30200 Ipoh, Perak,Malaysia
P: +60-5-2555000 F: +60-5-2553373

Philippines:

NSK REPRESENTATIVE OFFICE

MANILA 8th Floor The Salcedo Towers 169 H.V. Dela Costa St.,Salcedo Village Makati City, Philippines 1227
P: +63-2-893-9543 F: +63-2-893-9173

Singapore:

NSK INTERNATIONAL (SINGAPORE) PTE LTD.

SINGAPORE 238A, Thomson Road, #24-01/05, Novena Square Tower A, Singapore 307684
P: +65-6496-8000 F: +65-6250-5845

NSK SINGAPORE (PRIVATE) LTD.

SINGAPORE 238A, Thomson Road, #24-01/05, Novena Square Tower A, Singapore 307684
P: +65-6496-8000 F: +65-6250-5845

Thailand:

NSK BEARINGS (THAILAND) CO.,LTD.

BANGKOK 26 Soi Onnuch 55/1 Pravet Subdistrict, Pravet District, Bangkok 10250, Thailand
P: +66-2320-2555 F: +66-2320-2826

Vietnam:

NSK VIETNAM CO., LTD.

HANOI Techno Center, Room 204-205, Thang Long Industrial Park, Dong Anh District, Hanoi, Vietnam
P: +84-24-3955-0159 F: +84-24-3955-0158

NSK REPRESENTATIVE OFFICE

HO CHI MINH CITY Suite 307, Metropolitan Building, 235 Dong Khoi Street, District 1,HCMC, Vietnam
P: +84-28-3822-7907 F: +84-28-3822-7910

Worldwide Sales Offices

P: Phone F: Fax ☆: Head Office

●Europe

United Kingdom:

NSK EUROPE LTD. (EUROPEAN HEADQUARTERS)

MAIDENHEAD Belmont Place, Belmont Road, Maidenhead, Berkshire SL6 6TB, U.K.
P: +44-1628-509-800 F: +44-1628-509-808

NSK UK LTD.

NEWARK Northern Road, Newark, Nottinghamshire NG24 2JF, U.K.
P: +44-1636-605-123 F: +44-1636-605-000

France:

NSK FRANCE S.A.S.

PARIS Quartier de l'Europe, 2 Rue Georges Guynemer, 78283 Guyancourt, France
P: +33-1-30-57-39-39 F: +33-1-30-57-00-01

Germany:

NSK DEUTSCHLAND GMBH

DUSSELDORF ☆ Harkortstrasse 15, D-40880 Ratingen, Germany
P: +49-2102-4810 F: +49-2102-4812-290

STUTTGART Liebknechtstrasse 33, D-70565 Stuttgart-Vaihingen, Germany
P: +49-711-79082-0 F: +49-711-79082-289

WOLFSBURG Tischlerstrasse 3, D-38440 Wolfsburg, Germany
P: +49-5361-27647-10 F: +49-5361-27647-70

Italy:

NSK ITALIA S.P.A.

MILANO Via Garibaldi 215, Garbagnate Milanese (Milano) 20024, Italy
P: +39-299-5191 F: +39-299-025778

Netherlands:

NSK EUROPEAN DISTRIBUTION CENTRE B.V.

TILBURG Brakman 54, 5047 SW Tilburg, Netherlands
P: +31-13-4647647 F: +31-13-4641082

Poland:

NSK REPRESENTATIVE OFFICE

WARSAW Ul. Migdalowa 4/73, 02-796, Warsaw, Poland
P: +48-22-645-1525 F: +48-22-645-1529

Russia:

NSK POLSKA SP. Z O.O.

SAINT-PETERSBURG Office I 703, Bldg 29, 18th Line of Vasilievskiy Ostrov, Saint-Petersburg, Russia, 199178
P: +7-812-332-5071 F: +7-812-332-5072

Spain:

NSK SPAIN S.A.

BARCELONA C/Tarragona, 161 Cuerpo Bajo, 2a Planta, 08014, Barcelona, Spain
P: +34-93-289-2763 F: +34-93-433-5776

Turkey:

NSK RULMANLARI ORTA DOGU TIC. LTD. STI.

ISTANBUL Cevizli Mahallesi. D-100 Güney Yanyolu, Kuriş Kule İş Merkezi No:2 Kat:4, P.K.: 34846, Cevizli-Kartal-Istanbul, Turkey
P: +90-216-5000-675 F: +90-216-5000-676

United Arab Emirates:

NSK BEARINGS GULF TRADING CO.

DUBAI JAFZA View 19, Floor 24 Office LB192402/3, PO Box 262163, Downtown Jabel Ali, Dubai, U.A.E
P: +971-(0)4-804-8200 F: +971-(0)4-884-7227

●North and South America

United States of America:

NSK AMERICAS, INC. (AMERICAN HEADQUARTERS)

ANN ARBOR 4200 Goss Road, Ann Arbor, Michigan 48105, U.S.A.
P: +1-734-913-7500 F: +1-734-913-7511

NSK CORPORATION

ANN ARBOR 4200 Goss Road, Ann Arbor, Michigan 48105, U.S.A.
P: +1-734-913-7500 F: +1-734-913-7511

NSK PRECISION AMERICA, INC.

FRANKLIN ☆ 3450 Bearing Drive, Franklin, Indiana 46131, U.S.A.
P: +1-317-738-5000 F: +1-317-738-5050

SAN JOSE 780 Montague Expressway, Suite 505, San Jose, California, 95131, U.S.A.
P: +1-408-944-9400 F: +1-408-944-9405

NSK LATIN AMERICA, INC.

MIAMI 11601 NW 107 Street, Suite 200, Miami Florida, 33178, U.S.A.
P: +1-305-477-0605 F: +1-305-477-0377

Canada:

NSK CANADA INC.

TORONTO ☆ 317 Rutherford Road South, Brampton, Ontario, L6W 3R5, Canada
P: +1-888-603-7667 F: +1-905-890-1938

MONTREAL 2150-32E Avenue Lachine, Quebec, Canada H8T 3H7
P: +1-514-633-1220 F: +1-800-800-2788

Argentina:

NSK ARGENTINA SRL

BUENOS AIRES Garcia del Rio 2477 Piso 7 Oficina "A" (1429) Buenos Aires-Argentina
P: +54-11-4704-5100 F: +54-11-4704-0033

Brazil:

NSK BRASIL LTDA.

SUZANO ☆ Av. Vereador João Batista Fitipaldi, 66, Vila Maluf, Suzano-SP-Brazil-CEP 08685-000
P: +55-11-4744-2500

JOINVILLE Rua Blumenau, 178, sala 910, Centro, Joinville-SC-Brazil-CEP 89204-250
P: +55-47-3422-2239

Peru:

NSK PERU S.A.C.

LIMA Calle Teniente Enrique Palacios 360 Oficina 311 Miraflores, Lima, Peru
P: +51-493-4385

Mexico:

NSK RODAMIENTOS MEXICANA, S.A. DE C.V.

SILAO, GUANAJUATO Circuito Mexiamora Oriente No. 331, Parque Industrial Santa Fe I, Puerto Interior. Silao, Guanajuato, Mexico. C.P. 36275
P: +52-472-500-9500 F: +52-472-103-9403

<As of November 2020>

For the latest information, please refer to the NSK website.
www.nsk.com

Motion & Control

No. 32 June 2021

Published by NSK Ltd.

NSK used environmentally friendly printing methods for this publication.

CAT. No. ETJ-0032 2021 X-6 Printed in Japan